CONCEPT DEVELOPMENT OF ROTATING BED REACTOR FOR CHEMICAL LOOPING COMBUSTION USING METHANE AS FUEL AND COPPER OXIDE AS AN OXYGEN CARRIER

by

Saad Ali

Submitted in partial fulfilment of the requirements
for the degree of Master of Applied Science

at

Dalhousie University
Halifax, Nova Scotia
April 2015

TABLE OF CONTENTS

LIST OF TABLES

LIST OF FIGURES

ABSTRACT

A CFD model of a rotating bed reactor for chemical looping combustion involving the catalyzed reaction of methane with oxygen using a CuO-based oxygen carrier was developed in this work. The effects of process parameters (e.g., reactor rotation frequency, bed thickness and gas flow regions) on reactor performance were validated against experimental work published by Hakonsen (2011) and explored for a broader range of operating conditions. Three rotation speeds of 1, 2 and 4 RPM and three different bed thickness values of 10, 12 and 14 mm along with six different geometrical designs were simulated and used to propose a dimensionless graphical method of justifying design modifications in future reactors. The optimum combustion:purge:oxidation:purge angle ratios were found to be 106.52°:66.94°:126.01°:60.53°. For this configuration, the RPM can be adjusted for a given bed thickness and combustion rate to yield a total dimensionless rotation period of $t/t_{bed} = 12.37$.

LIST OF ABBREVIATIONS AND SYMBOLS USED

b_i Stoichiometric factor for the reaction i, mol solid reactant, per mol of fuel
C Concentration, mol m^{-3}
D_e Effective diffusivity, m^2 s^{-1}
D_{AB} Binary diffusion coefficient, m^2 s^{-1}
E Activation energy, J mol^{-1}
g_c Gravitational conversion factor
K Chemical reaction rate constant, mol^{1-n} m^{3n-2} s^{-1}
k_0 Pre-exponential factor of the chemical reaction rate constant, mol^{1-n} m^{3n-2} s^{-1}
n Reaction order
P Pressure, atm
$-r_g$ Reaction rate of gas, s^{-1}
$-r_s$ Reaction rate of the oxygen carrier, s^{-1}
R Constant of the ideal gases, J mol^{-1} K^{-1}
S Gas flux, mol m^{-3} s^{-1}
T Temperature, K
$M_{A,B}$ Molecular weights of A and B, g mol^{-1}
u Gas velocity, m s^{-1}
X The reactor length (bed thickness), m
Ra Reactor area, m^2
x Molar fraction

Greek letters

ρ_m Molar density of the reacting material, mol m^3
τ_i Time for complete solid conversion for the reaction i, s
σ_{AB} Characteristic length, Å
ρ_p Density of pellet, kg m^{-3}

Subscripts

PFCs Tetraflouromethane (CF_4)
HFCs Hexaflouroethane (C_2F_6)
SF_6 Sulfur hexafluoride

Definitions of non-dimensional variables

$\tilde{\tau}$ Tortuosity
ϕ_P Pellet porosity
σ_c Constriction factor
k Boltzmann's constant
Ω_D Diffusion collision integral
ε_{AB} Lennard-Jones potential energy parameter for A-B interaction
ε_b Bed porosity

ACKNOWLEDGEMENTS

I would like to express my gratitude to everyone who, in one way or another, contributed to this thesis. In particular, I would like to thank my supervisor, Professor Michael J. Pegg, for providing me with the opportunity to work in this fascinating field. I would also like to thank him for his interest in my work and for his encouragement.

As well, I wish to thank my co-supervisor, Dr. Adam Donaldson, who was always ready and willing to help me. This thesis would not have been accomplished without his kindness, guidance and support. His efforts and advice helped me make timely progress and overcome many difficulties I faced during this research.

My thanks go also to Professor Dominic Groulx, who gave me the opportunity to work in his lab with his LAMTE team, and provided me with all modeling requirements.

Finally, I owe immense gratitude to my wife and my parents, whom I love more than anyone else in the world. Through their prayers, patience and love, they have helped me surmount every challenge and bring this labor of love and research to a happy conclusion.

CHAPTER 1. INTRODUCTION

Numerous studies have confirmed that the concentration of greenhouse gases including carbon dioxide (CO_2), and the earth's temperature (global warming) have simultaneously been increasing in recent decades, (U.S. Department of Commerce, 2015; NASA Goddard Institute for Space Studies, 2015). It is generally agreed that greenhouse gases contribute to increased global temperatures and that the reduction of CO_2 emissions into the atmosphere is one way to offset the warming trend. There are both natural and human sources of carbon dioxide emissions. Natural sources include decomposition, ocean release and respiration. Human sources come from activities like vehicle use, electricity production, cement production, deforestation as well as the burning of fossil fuels like coal, oil and natural gas, which considered to be the major current source of CO_2. Lyngfelt (2001) suggests that, in "developing countries, economic growth results in a rapid increase in the demand for energy supplied by fossil fuels, while the developed countries have not yet found the means for substantially decreasing their use of these fuels". Since the combustion process (i.e., direct contact between air and fuel) requires a high-cost technique as well as special equipment to separate CO_2 from other flue gas components (e.g., nitrogen, water vapor, unused oxygen) and trace amounts of minor pollutants such as SO_x and NO_x, it is imperative to find a new combustion method. Such a method should enable CO_2 to be separated from the flue gases with only a small loss in efficiency. This thesis focus on chemical-looping combustion (CLC) as a new combustion technique that features inherent separation of CO_2.

1.1 THE GREENHOUSE EFFECT.

In light of the massive current energy demand worldwide, renewable energy sources such as wind power, wave power, solar energy, tidal energy and geothermal heat have a limited potential for substitution of fossil energy (Strömberg, 2001). Nevertheless, while using fossil fuels to supply most of the current world's power needs appears to be the most viable option at this present time, fossil fuel combustion releases a tremendous amount of greenhouse gases. Greenhouse gases such as CO_2, N_2O, CH_4, HFCs, PFCs and SF_6 trap heat in the atmosphere from escaping. Furthermore, because approximately 55%

of the gases are CO_2, global warming is enhanced when both concentration and absorption are considered (Harvey, 2000).

The average annual growth rate of CO_2 concentration was approximately 1.71 ppm from 1979 to 2012. Since 1995, however, this rate has risen to nearly 2 ppm per year, which contributes to global warming, as reported by the U.S. Department of Commerce. One major consequence of increasing global temperatures in the Northern Hemisphere is that snow cover and sea-ice have been decreasing for the past 46 years, resulting in higher sea water levels and flooding. The damage caused by these and related events, including ice jams, are projected to cost Canada CAN$60 million and America US$100 million annually, (IPCC, 1997). Consequently, the reduction of CO_2 emissions from fossil fuels combustion into the atmosphere has become ecologically indispensable. Such a reduction, however, is challenging, given the world's present and anticipated energy demands. Therefore, with the recent focus on global warming and the effects of CO_2 emissions during power generation, a number of unconventional combustion and CO_2 sequestration technologies are being explored.

1.2 CO_2 SEPARATION AND SEQUESTRATION.

Several methods can be used to separate and mitigate the emissions of carbon dioxide into the atmosphere.

- Post combustion
- Pre combustion
- O_2/CO_2 combustion ("oxy fuel")

1.2.1 Post-combustion capture

In post-combustion capture, which is the closest concept to conventional combustion, CO_2 is captured from flue gases derived from coal, natural gas, or oil combustion. The carbon dioxide is separated from the flue gases via a chemical absorption process that uses an absorbing media such as a mono-ethanol amine (MEA)-based absorber. The combustion takes place by mixing the fuel and air as a first step (combustion process), as presented in Figure 1-1. This results in the release of heat and releases CO_2 with other flue gases, such as Nitrogen, unused Oxygen, Water, SO_x, and

NO_x. The second step, which takes place in the separation unit, involves separating CO_2 by using, for example, MEA as an absorber to selectively absorb CO_2 from the other flue gases. The CO_2-rich MEA solution is then sent into the generation unit (stripper). In the stripper, the CO_2-rich MEA solution is heated to release almost pure CO_2 into the storage tank and generate a CO_2-lean MEA solution, which is circulated back into the separation unit (Herzog, 2009). Because the consumed energy in the generation unit is taken from the combustion process, the net energy efficiency of the process is affected.

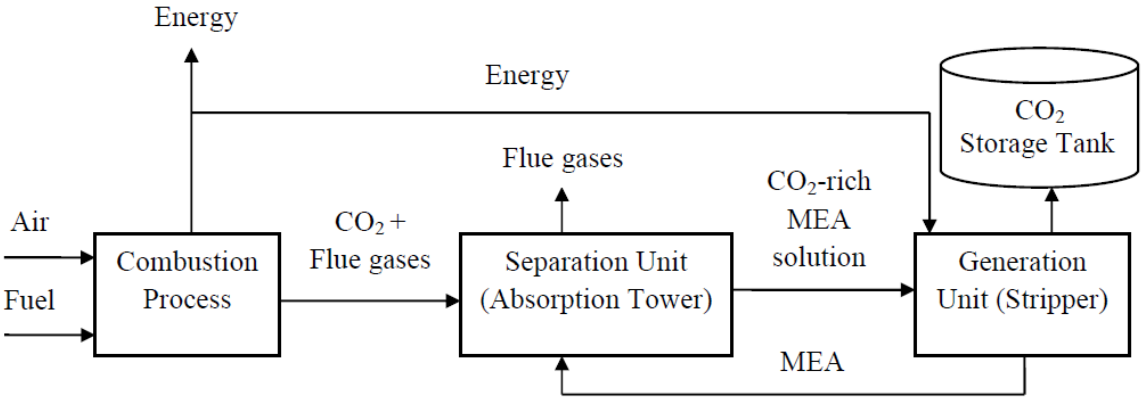

Figure 1-1 A sketch of post-combustion with the amine absorption concept, (Herzog, 2009).

1.2.2 Pre-combustion capture

In the process known as pre-combustion capture, CO_2 can be separated before the combustion process. This combustion procedure can be carried out by either one of two strategies, coal gasification or natural gas reforming. The fuel (coal or CH_4) is converted into a synthesis gas (syngas) composed of CO and H_2. As a first step, and as shown in Figure 1-2, the syngas (here, H_2 and CO) can be formed by gasifying the coal within partial oxidation in a gasification unit or mixing the natural gas with steam in a reforming unit. In the second step, the CO reacts with H_2O as a shift reaction in the shifting unit (catalytic reactor) to produce CO_2 and more H_2. Through the separation unit, the CO_2 can be captured, by a physical or chemical absorption process. In the chemical absorption process, chemical absorbents, such as Methyl diethanolamine (MDEA) react with acid gases and are then heated to release the acid gases by reversible reaction. In the physical absorption process, within a media of high pressure, physical absorbents, for example, Selexol absorbs acid gases, can be released from the solvent by decreasing the pressure

and increasing the temperature. With the physical absorption process, the required steam-heat for solvent generation is less than that in the chemical absorption process.

Because CO_2 requires auxiliary energy to be compressed for storage, using high pressure in the absorption process gives the pre-combustion capture some thermodynamic advantages over the post-combustion capture, (Global CCS Institute, 2011). Since it is not yet diluted by the combustion air, the H_2 can be used in many applications, such as boilers, furnaces, gas turbines, engines, and fuel cells, (IPCC, 2005). Using CH_4 as fuel, the concept of pre-combustion capture can be performed by several methods, such as pre-combustion with an auto-thermal reformer (ATR) and pre-combustion with a hydrogen membrane reactor (MSR-H_2), (Kvamsdal, 2007).

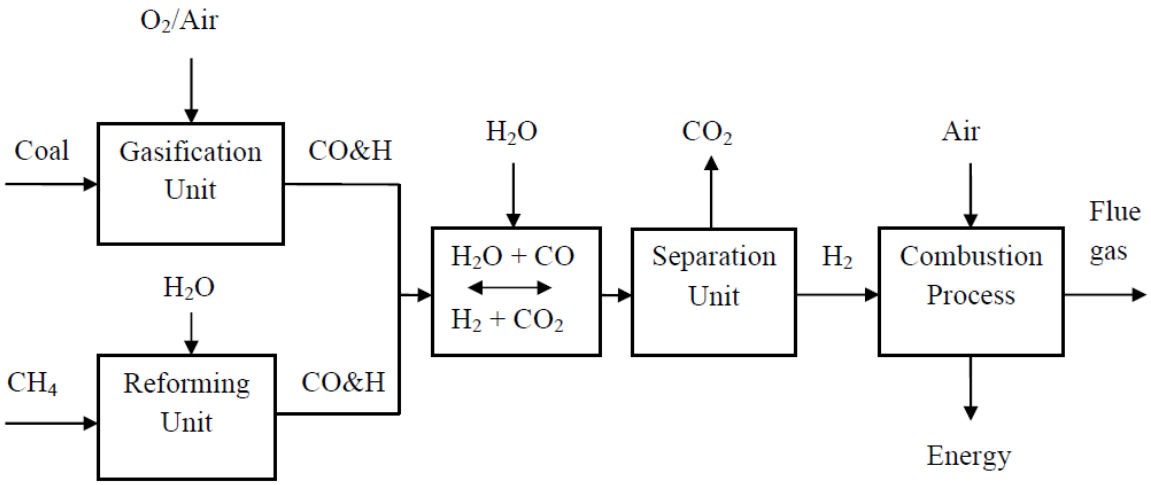

Figure 1-2 A sketch of pre-combustion with both strategies (coal gasification and natural gas reforming).

1.2.3 Oxy-Fuel combustion

The concept of Oxy-Fuel combustion is to burn the fossil fuel in pure or enriched oxygen. As a first step, the oxygen is derived and separated from nitrogen in the air in the separation unit, as can be seen in Figure 1-3. Thus, almost pure oxygen is sent into the combustion process. The purified oxygen is consumed during the combustion of the fuel and produces mostly CO_2 and H_2O as flue gases. To mitigate the excessive flame temperature caused by the fuel combustion in pure oxygen, some of the flue gas (CO_2 and/or H_2O-rich flue gas) is circulated into the combustion chamber. To prevent the need for flue gas circulation, some techniques, such as membranes and chemical looping

cycles are being developed to supply oxygen to the fuel at low temperature (IPCC, 2005). The rest of the flue gas is sent into the CO_2 purification unit to condense H_2O, which can be supplied to heat the recovery steam generator for the bottoming cycle, and compress CO_2 into the storage tank, which can be used, for example, in enhanced oil recovery. The concept of Oxy-Fuel combustion can be carried out by several methods, such as the oxy-fuel combined cycle, the water cycle, the Graz cycle, the advanced zero emissions power plant (AZEP), solid oxide fuel cell (SOFC) integrated with a gas turbine, and chemical looping combustion, (Kvamsdal, 2007).

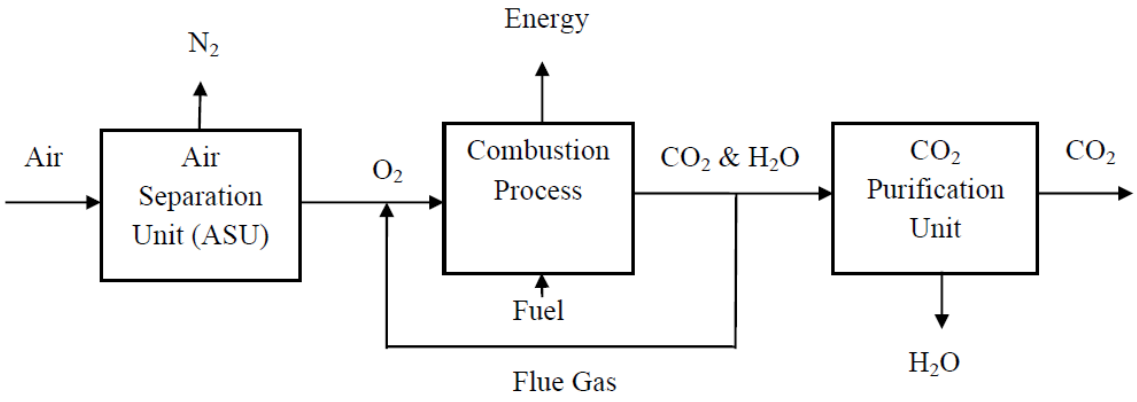

Figure 1-3 A sketch of Oxy-Fuel-combustion with the flue gas circulation concept.

1.3 A QUANTITATIVE COMPARISON OF SEVERAL CONCEPTS OF UNCONVENTIONAL COMBUSTION AND CO_2 SEQUESTRATION.

Kvamsdal (2007) investigated a quantitative comparison of the net plant efficiency of six varied concepts of Oxy-Fuel combustion, two varied concepts of pre-combustion, and one concept of post-combustion, as shown in Table 1-1. Oxy-Fuel combustion was presented by the following six concepts: (1) the oxy-fuel combined cycle, (2) the water cycle, (3) the Graz cycle, (4) the advanced zero emissions power plant (AZEP), (5) solid oxide fuel cell (SOFC) integrated with a gas turbine, and (6) chemical looping combustion (CLC). The pre-combustion was carried out by the two following concepts: (1) an auto-thermal reformer (ATR) and (2) a membrane reactor (MSR-H_2). The post combustion was performed based on a conventional combined cycle (CC) with CO_2 separation from the exhaust gas by chemical absorption (Amine).

Table 1-1 (Kvamsdal, 2007) Concept description of gas turbine cycles with CO2 capture

Concept name	Short name	Type of concept	Steam bottoming cycle
1. Oxy-fuel combined cycle	Oxy-fuel CC	Oxy-fuel	Yes
2. Water cycle	WC	Oxy-fuel	No
3. Graz cycle	Graz	Oxy-fuel	No
4. Advanced zero emissions power plant	AZEP	Oxy-fuel	Yes
5. Solid oxide fuel cell integrated with a gas turbine	SOFC + GT	Oxy-fuel	No
6. Chemical looping combustion	CLC	Oxy-fuel	Yes
7. Pre-combustion with an auto thermal reformer	ATR	Pre-combustion	Yes
8. Pre-combustion with a hydrogen-separating membrane reactor	MSR-H2	Pre-combustion	Yes
9. Post-combustion with amine absorption	Amine	Post-combustion	Yes

For the nine concepts, the net plant efficiency in percentage of the natural gas (NG) fuel with lower heating value was obtained. A standard combine cycle without CO_2 capture (CC base case) was applied as a reference case. As illustrated in Figure 1-4 (Kvamsdal, 2007), among the nine concepts, the best results were given by the concepts that involve new and emerging technology, such as CLC, MSR-H_2, AZEP, and SOFC+GT. In addition, the SOFC+GT concept shows better efficiency than the CC base case. Kvamsdal, (2007) indicated that the emerging technologies (CLC, MSR-H_2, AZEP, and SOFC+GT) generally provide higher efficiency values.

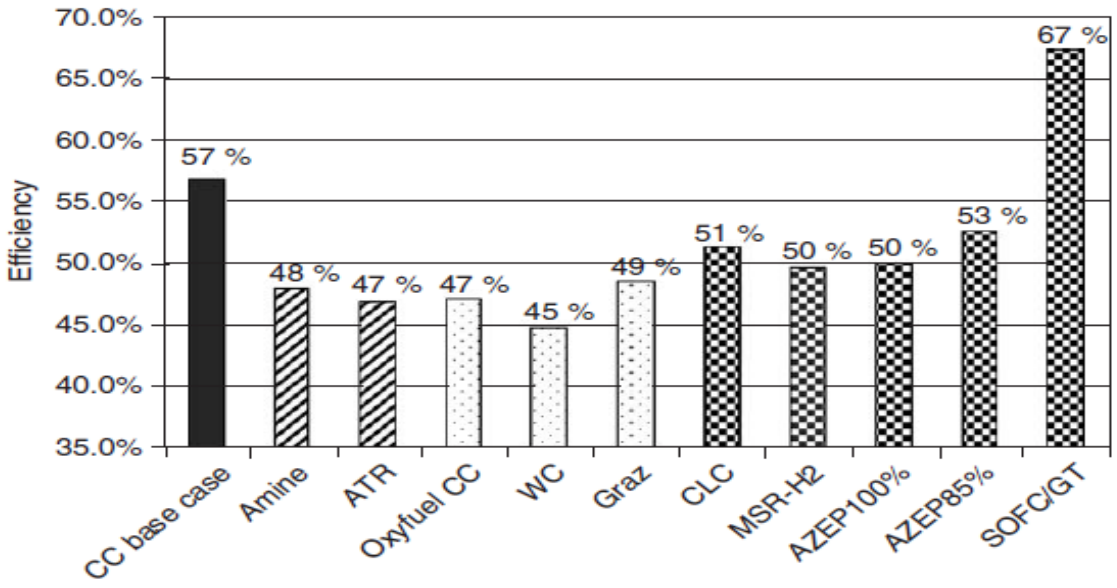

Figure 1-4 (Kvamsdal, 2007): Net plant efficiency of the nine concepts and a CC concept in % of the NG fuel LHV

As presented in Table 1-2, the cryogenic production of oxygen in some oxy-fuel concepts, such as oxy-fuel CC, WC, and Graz, is considered the major cause of reduction in efficiency. If the reduced CO_2 capture is compared to the 100% capture case, the AZEP and CLC concepts exhibit much better efficiency. The CLC can be considered a promising technology if the reactor system and the operating conditions (temperature and pressure) can be developed to overcome performance limits and run for long-term time frame of realization, (Kvamsdal, 2007).

Table 1-2 (Kvamsdal, 2007): Net plant efficiency for nine concepts of unconventional combustion and CO_2 sequestration.

	CC base case	Amine	ATR	Oxyfuel CC	WC	Graz	CLC	MSR -H_2	AZEP 100%	SOF C /GT
Chemical energy in fuel (LHV)	100%	100%	100%	100%	100%	100%	100%	100%	100%	100%
Turbines	96.4%	92.0%	85.7%	89.7%	62.0%	102%	103%	87.6%	104%	32.5%
Compressors	37.6%	37.6%	34.9%	28.7%	0.1%	36.6%	47.5%	33.4%	51.8%	17.3%
Cross power	58.8%	54.4%	50.8%	60.9%	61.9%	66.1%	55.5%	54.3%	52.8%	15.3%
Generator & mechanical eff	1.2%	1.1%	1.0%	1.2%	1.2%	1.3%	1.1%	1.1%	1.1%	1.5%
Net shaft power	57.6%	53.3%	49.8%	59.7%	60.7%	64.8%	54.4%	53.2%	51.7%	13.7%
Fuel Cell DC output	-	-	-	-	-	-	-	-	-	61.2%
Efficiency, DC to AC grid	-	-	-	-	-	-	-	-	-	31.1%
Net Fuel cell electric output	-	-	-	-	-	-	-	-	-	58.2%
Auxiliaries	0.6%	0.5%	0.5%	0.6%	0.7%	0.6%	0.5%	0.5%	0.5%	0.7%
Pumps	0.3%	0.6%	0.2%	0.3%	0.2%	0.5%	-	0.3%	0.2%	-
Ejectors	-	-	-	-	-	-	-	-	-	1.4%
Oxygen production	-	-	-	6.4%	6.6%	6.5%	-	-	-	-
Oxygen compression	-	-	-	2.4%	2.5%	2.7%	-	-	-	-
Amine absorption	-	2.0%	-	-	-	-	-	-	-	-
Compression work, CO_2	-	2.3%	2.2%	3.0%	6.1%	5.9%	2.5%	2.7%	1.0%	2.6%
Total consumers	0.8%	5.4%	2.9%	12.7%	16.1%	16.2%	3.1%	3.6%	1.7%	4.6%
Net efficiency	56.7%	47.9%	46.9%	47.0%	44.6%	48.6%	51.3%	49.6%	50.0%	67.3%
Reduction compared to the base case	-	8.8%	9.9%	9.7%	12.5%	8.2%	5.5%	7.1%	6.8%	-10%

CHAPTER 2. CHEMICAL LOOPING COMBUSTION (CLC)

Chemical-looping combustion (CLC) has emerged as an effective technology to decrease greenhouse gas emissions because CLC is a combustion process in the absence of direct contact between air and fuel, with inherent separation of CO_2. In this technique, there is no need for high cost working processes or large energy expenditure to separate CO_2 from flue gases, such as nitrogen, unused oxygen, and water. In the 1950s, chemical-looping combustion was invented as a procedure to produce pure carbon dioxide (Lewis and Gilliland, 1954). Later, in the 1980s and '90s, CLC was proposed as a viable technology to capture and sequester carbon dioxide from the other flue gas components produced by fossil fuel combustion (Ritcher, 1983; Ishida, 1994). CLC technology includes the use of an oxygen carrier that transfers oxygen from combustion air (metal-oxidation) to the fuel (metal-reduction), precluding direct contact between air and fuel. The oxygen carrier is usually a metal oxide (Jernald, 2006). CLC research has not only investigated gaseous fuels (CH_4, H_2 or CO) but also solid fuels such as coal, which is considered a major fossil fuel source and has been utilized as a solid fuel for CLC (Jin, 2004). In addition, Hoteit (2011) has suggested that liquid fuel such as heavy fuels resulting from oil distillation or conversion may also be valid feedstocks worth considering.

There are three available techniques to perform the oxidation and reduction of the metal oxide within the chemical-looping combustion. The first technique involves using an interconnected fluidized bed reactor to circulate a metal oxide between a fuel reactor (where the fuel is oxidized by reduction of the metal oxide) and an air reactor (where the reduced metal oxide is re-oxidized by contact with air) (Lyngfelt, 2001; Proll, 2009; Berguerand, 2010). The second technique involves using a packed bed reactor, where the oxidation and reduction can be carried out by switching gas feed streams, an air stream and fuel stream, through a bed of metal particles (Noorman, 2007). The third technique includes using a rotating bed reactor to rotate a fixed packed bed containing metal oxide between fuel and air stream sectors where the metal oxide is reduced and re-oxidized, respectively (Dahl, 2009; Hakonsen, 2011). Via these three techniques, the oxygen carrier is alternately exposed to two separate streams (the fuel stream and the air stream). Fuel

combustion takes place within the fuel stream, which results in reducing the oxygen carrier $(2n+m)M_yO_x$ and producing only H_2O and CO_2; thus, CO_2 does not mingle with N_2 compared to the traditional combustion (Lyngfelt, 2001):

$$(2n+m)M_yO_x + C_nH_{2m} \longrightarrow (2n+m)M_yO_{x-1} + mH_2O + nCO_2 \quad 2.1$$

Water can be removed through a condensation process and almost pure CO_2 can be obtained, which results in making CLC a distinct separation method. Within the air stream, the reduced oxygen carrier $(2n+m)M_yO_{x-1}$ is re-oxidized by reaction with air and absorbing oxygen, (Lyngfelt, 2001):

$$M_yO_{x-1} + \tfrac{1}{2}O_2 \longrightarrow M_yO_x \quad 2.2$$

The oxygen carrier can then continuously be exposed to the alternative stream. The flue gases are mostly nitrogen and unused oxygen. Solid particles based on Cu, Ni, Co, Mn and Fe have been extensively investigated as feasible oxygen carriers to be used in CLC systems. Considerable research has been carried out on CLC in the past a few years with respect to oxygen carrier improvement, reactor design, system efficiencies and prototype testing.

Lyngfelt (2010) stated that "more than 700 materials have been tested and the technology has been successfully demonstrated in chemical-looping combustors, using different types of oxygen carries. From these tests, it can be established that almost complete conversion of the fuel can be obtained and 100% CO_2 capture is possible". Similarly, Dahl (2009) indicated that the CLC concept has a 55% energy efficiency rate. Based on the progressive development and the efficacious performance of the CLC technology, power plants could, in the near future, be capable of using this combustion method instead of traditional methods, thereby largely mitigating the emissions of carbon dioxide released from the fossil fuel plants to the atmosphere.

2.1 FLUIDIZED BED REACTOR

The reactor is best described as a fluidized bed reactor (see Figure 2-1) where metal oxide particles as oxygen carriers are circulated between two interconnected fluidized beds, an air reactor and fuel reactor. Through the air reactor, which is considered a high-

velocity riser, metal particles adsorb oxygen by chemical reaction within the combustion air. They are then transferred from the air reactor to the fuel reactor by the driving force resulting from the high-velocity air flowing from the bottom to the top of the air reactor. The flue gases are mostly nitrogen and unused oxygen. Lyngfelt (2001) stated that "the volumetric gas flow in the air reactor is approximately 10 times larger than that of the gaseous fuel, and to keep a reasonable size of the reactors a high velocity is chosen in the air reactor".

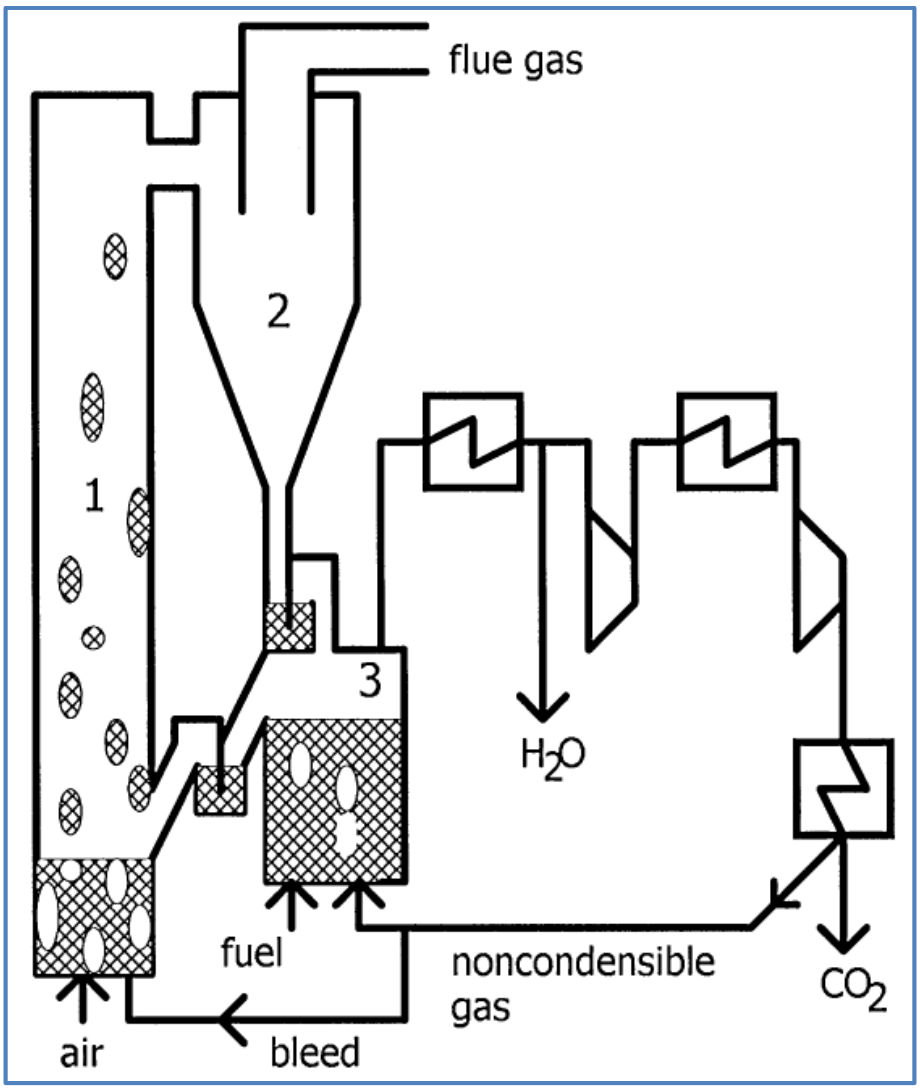

Figure 2-1 (Lyngfelt, 2001): Layout of chemical-looping combustion process, with two interconnected fluidized beds.

Within the fuel reactor (a low-velocity bubbling fluidized bed), the oxidized metal particles react with the fuel, reducing the oxidized metal particles and producing CO_2 and H_2O. The reduced metal particles can then be returned to the air reactor by gravity (i.e., the fuel reactor is higher than the air reactor). In order to reach high fuel conversion and high rate of reaction in both metal oxidation and metal reduction, flow of solid material between the two reactors is required to grant a good contact between gas and solid; and therefore a reactor [in Figure 2-1] with two interconnected fluidized beds has much better design than other several ways of design, Lyngfelt (2001). On the other hand, the major difference in volumetric gas flows between the air reactor and the fuel reactor will cause a significant drop in pressure, ultimately making the nitrogen slip to the fuel reactor. As a result, unwanted mixing of N_2, CO_2, unreacted fuel and water vapor occurs inside the fuel reactor. This mixing is considered a disadvantage, as are the attrition problems caused by the fluidized circulation of metal particles (Dahl, 2009). Additionally, due to the expansion of the reactor's bed materials, a bigger vessel is sometimes necessary, which is not the case for a packed bed reactor. This bigger-sized vessel would necessitate a larger expenditure in start-up costs (Trambouze, 2004).

2.2 PACKED BED REACTOR

The packed bed reactor (see Figure 2-2) is best described as a packed bed reactor where metal particles, based-oxygen carriers, are packed in a fixed bed. In this reactor-concept, the metal particles are fixed, while the gas streams, an air stream and fuel stream, are fed through the packed bed via regular switching. Metal oxidation takes place when the air stream is fed, while metal reduction occurs by switching the air stream with the fuel stream, which also results in fuel combustion.

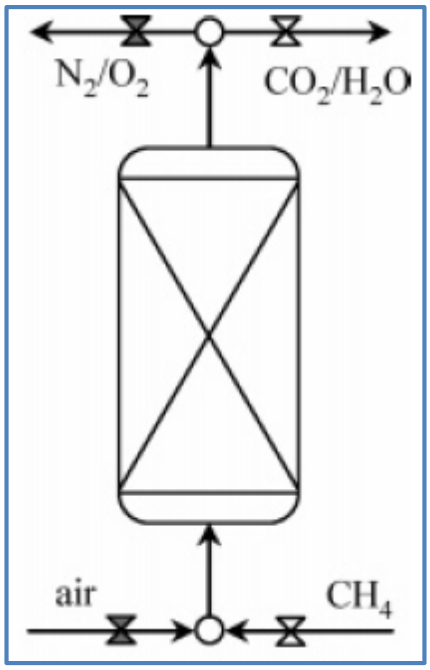

Figure 2-2 (Noorman, 2007): The concept of a packed bed reactor for CLC system.

The main advantages of the packed bed reactor technology, where the solids are stationary is the separation of gas and particles is intrinsically avoided, thus the design of reactor can be more compact. On the other hand, a high temperature and high flow gas switching system is required, which can be considered a disadvantage of this concept (Noorman, 2007). Switching gas feed streams prevents obtaining a constant energy rate. As a result, to accomplish high process energy efficiency, at least two reactors in parallel are required to provide a continuous high temperature gas stream to the gas turbine. As described by Dahl (2009), fixed bed setups suffer from particle crushing due to less frequent particle inventory changes from the inherent difficulty associated with changing particles during operation, consequently this will generate fines overtime.

2.3 ROTATING BED REACTOR

The reactor (see Figure 2-3) is best described as a rotating bed reactor. The internal annular feed system is divided into four sectors: two sectors (stream sectors) have streams of an inert gas that separate the other two sectors, which have reacting gas streams (an air stream and fuel stream). The inert gas is utilized to prevent mixing of the two reacting

gases inside the reactor. The middle annular fixed bed bears particles of an oxygen carrier and rotates between the different gas streams.

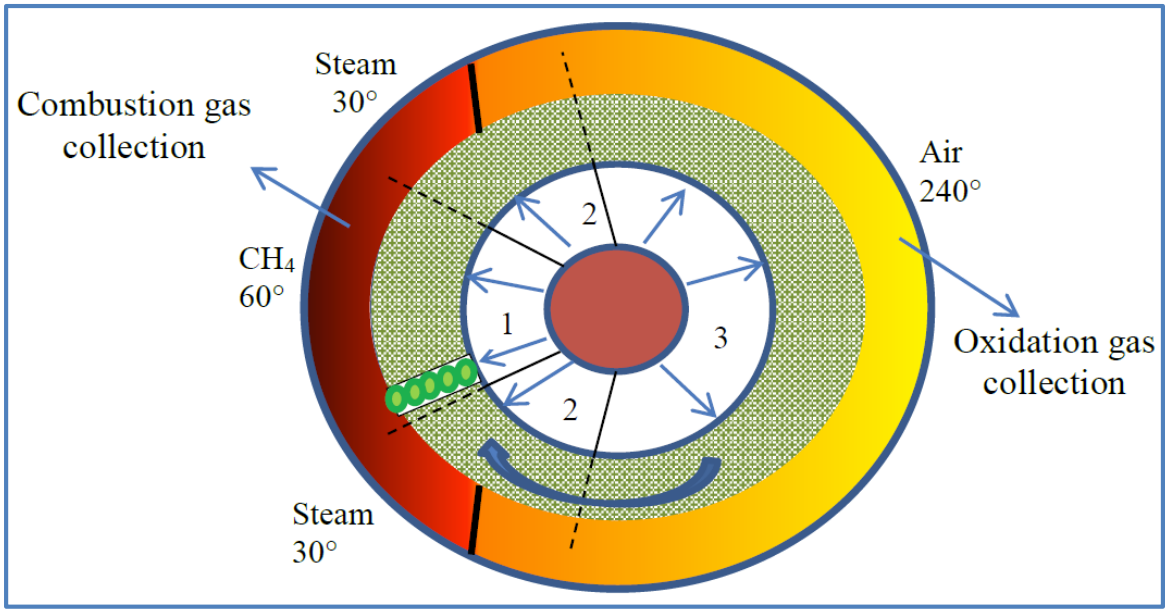

Figure 2-3 Schematic drawing of the rotating bed reactor used: The blue part indicates the various gas inlet sectors, the green part the rotating oxygen carrier bed (viewed along the rotating axis), while the red/yellow parts show the two exit chambers.

The four gas streams have radial flow going from the internal annular feed system towards the middle annular fixed bed (through the particles of an oxygen carrier) and into the external annular outlet system divided into two exit chambers separated by two stationary walls, each of which is located in the middle of each steam sector. The only moving part in this reactor is the middle annular fixed bed while the others are stationary. The red central circle is a heater that is used to heat up the feed gases to a suitable reaction temperature. Dahl (2009) stated: "we imagine that such a reactor could be very compact and easy to operate as compared to the fluidized bed reactor", and that a "radially directed gas flow will give the best gas flow performance". Dahl (2009) further explains that volume expansion arising from an increase in moles of gas and gas temperature (due to reaction exothermisity) "will be best compensated by the radial reactor volume increase. However, the main challenge with such a reactor concept is to avoid gas mixing between the fuel and air gas streams". Further, according to Hakonsen (2011): "rotation of the oxygen carrier bed is done by coupling the bed holder to a shaft

that can be rotated from the outside by a drive belt". The bearing can be located between the static inner part-tube and the rotating part-tube in order to keep the rotating bed moving smoothly between the different gas streams. In addition, the reactor is supplied by water cooling to keep the bearing at low temperatures. Hakonsen (2011) stated that the rotating bed reactor is well suited for operation at elevated pressure. As gases flow naturally from high pressure to low pressure areas, the high pressure drop inside the rotating bed reactor largely causes unwanted internal gas mixing (Dahl, 2009). Also, large temperature gradients caused by significantly different enthalpies of oxidation and reduction reactions will eventually lead to internal gas mixing (Dahl, 2009). With regards to this situation, Dahl (2009) stated: "We also believe that a uniform temperature is wanted to avoid stress in reactor construction which ultimately could lead to leakages". This reactor will be considered in this work because of the new concept with certain attractive advantages such as, operating at low temperatures, inherent separation of CO_2 (avoiding energy wastage and separation unit), involving very little to 5% internal gas mixing, obtaining high to 90% fuel conversion with simple operation having no high attrition.

2.4 CHOICE OF OXYGEN CARRIER

In order to apply chemical-looping combustion with high efficiency (high fuel conversion), transferring the air's oxygen to the fuel sector by means of an appropriate oxygen carrier with high oxygen capacity is essential. The oxygen carrier should be highly reactive in both reactions, oxidation by air and reduction by fuel (Mattisson, 2001). It should also have excellent physical and chemical stability (Haber, 1991) and be environmentally friendly and nontoxic. Furthermore, the oxygen carrier should have sufficient physical strength to resist attrition and fragmentation (Cho, 2004). Since big difference in enthalpies of reduction and re-oxidation reactions, along with high pressure drop and large temperature gradient lead to unwanted internal gas mixing inside the rotating bed reactor (Dahl, 2009), an oxygen carrier having the following specifications would be very helpful to achieve an effective performance of the rotating bed reactor.

- Close to equal enthalpies for both reduction and re-oxidation reactions.
- High reactivity at relatively low temperature.

- Good stability.
- High mechanical strength.
- High oxygen capacity.
- No negative environmental effects.

In the CLC process, the chemical reaction of an oxygen carrier with methane and air can be divided into two half-reactions (Dahl, 2009), as follows:

$$CH_4 + 4MO \longrightarrow CO_2 + 2H_2O + 4M \qquad \Delta H^o_{red} \qquad 2.3$$

$$4M + 2O_2 \longrightarrow 4MO \qquad \Delta H^o_{ox} \qquad 2.4$$

Where MO represents the oxidized metal oxide and M the reduced metal oxide. The total reaction enthalpy inside the reactor is distributed into two part-reactions and intensely influenced by the properties of the metal oxide utilized. Table 2-1 shows the enthalpies of the two half-reactions for various metal oxides.

Table 2-1 (Dahl, 2009): The enthalpies of various metal oxides based on two part-reactions.

MO/M pair	ΔH^o_{red} (kJ/mole)	ΔH^o_{ox} (kJ/mole)
Fe_3O_4/FeO	386	-1192
NiO/Ni	132	-934
CoO/Co	-8	-794
CuO/Cu	-206	-596
$LaCoO_3/LaCoO_{2.5}$	-280	-522
$La_{0.6}Sr_{0.4}Fe_{0.5}Mn_{0.5}O_3$/ $La_{0.6}Sr_{0.4}Fe_{0.5}Mn_{0.5}O_{3-\delta}$	-320	-482

A CuO-based oxygen carrier was tested and presented as a metal oxide with fast kinetics at a comparatively low temperature of 700°C (Son, 2009). In proportion to Table (2.1), a CuO-based oxygen carrier has no significantly different enthalpies of both exothermic part-reactions. It was therefore selected in the first tests by Dahl (2009) to avoid a large temperature gradient which ultimately leads to an undesirable high pressure drop (more gas mixing). According to Dahl (2009), "wet impregnation of $Cu(NO_3)_2$ on γ-Al_2O_3 was used to prepare oxygen carrier having > 10wt% oxygen capacity", after which spheres of a CuO-based oxygen carrier with a diameter of 2 mm were tested to confirm the stability of a copper oxide as an oxygen carrier, as shown in Figure 2-4.

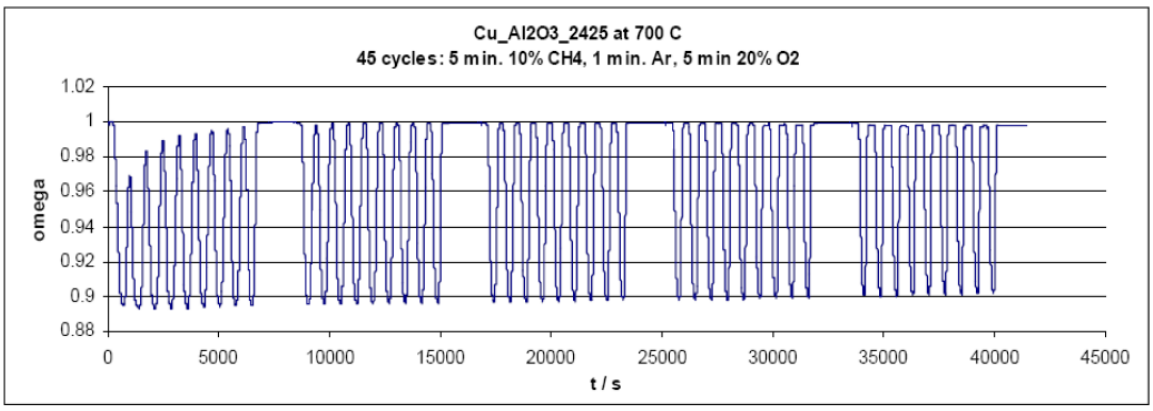

Figure 2-4 (Dahl, 2009): TG traces of CuO/Al_2O_3 material under red-ox cycling in 10% CH_4 and 20% O_2 at 700℃.

Many other studies have been carried out on the mechanical strength and reactivity of oxygen carries. For instance, Adanz (2004) compared different metal oxides, as shown in Table 2-2.

Table 2-2 (Adanz, 2004): Reactivity of different oxygen carriers and selection of the most promising carriers.

Metal-based oxygen carriers

		Cu				Fe				Mn				Ni			
	T_{sint} (℃)	950	1100	1200	1300	950	1100	1200	1300	950	1100	1200	1300	950	1100	1200	1300
Inert	MeO(%)	red-oxid															
Al_2O_3	80	a-a	c-c			a-a	a-a	b-b	b-b	a-a	b-b	c-c		a-a	a-b*	a-b*	b-c*
	60	a-a	c-c			a-a	b-b	b-b	b-b	b-b	c-c	c-c		a-a	a-b*	b-c*	c-c
	40	a-a	e-e			a-a	a-a	b-b	b-b	c-c	e-e	e-e		a-a	b-c	c-c	e-e
Sepiolite	80	a-a				a-a	a-a			a-a	a-a			a-a	a-a	a-a	e-e
	60	a-a				a-a	a-a			a-a	a-a			a-a	a-a	b-b	
	40	a-a				a-a	a-a			a-a	c-e			a-a	b*-a	e-e	
SiO_2	80	a-a				b-b	b-b			a-a	b-b			a-c*	a-c*	a-c*	a-b*
	60	a-a				a-a	b-b			a-a	e-e			a-c*	a-d	a-d	a-c
	40	a-a				a-a	a-a			a-a	e-e			a-c*	b-d	c-d	
TiO_2	80	a-a				a-a	b-b	b-c*	b-c*	b-b	b-b			a-b*	a-b*	a-b*	b*-c*
	60	a-a				a-a	b-b	b-c*	c-c	e-e	e-e			a-a	a-a	a-a	a-b*
	40	a-a				a-a	b-c*	b-c*	b-d	e-e	e-e			a-a	a-a	a-a	a-b*
ZrO_2	80	a-a				a-a	a-a	a-a	b-b	a-a	a-a	a-a	a-b*	a-c*	a-c*	a-d	a-d
	60	a-a				a-a	a-a	a-a	b-b	a-a	a-a	a-a	a-b*	a-b*	a-b*	a-b*	a-b*
	40	a-a				a-a	a-a	a-a	b-b	a-a	a-a	a-a	b*-b*	a-b*	a-b*	a-b*	a-b*

a = High reactivity and high conversion (X > 0.8 in 1 min)
b = Conversion between 0.5-0.8 in 1 min.
c = Conversion between 0.3-0.5 in 1 min.
d = Conversion lower than 0.3 in 1 min but higher than 0.3 in 20 min.
e = Low reactivity or low conversion (X < 0.3 in 20 min).
* = Reach high conversion at long time

Melt or decompose

Low reactivity or crushing strength

Selected particles by mechanical strength and reactivity

From Table 2-2, it can be concluded that at relatively low temperature (950℃), CuO-based oxygen carriers have good reactivity and good crushing strength value,

especially the ones that are prepared by SiO_2 and TiO_2. Son (2009) stated that the reactivity of CuO supported on Al_2O_3 is faster in both reactions than that on SiO_2. Also, Lyngfelt (2008) performed a comparison regarding the reactivity and other properties of Ni, Mn, Cu and Fe, as seen in Table 2-3.

Table 2-3 (Lyngfelt, 2008): Qualitative estimation of pros and cons for the active oxides

	Fe_2O_3/Fe_3O_4	Mn_3O_4/MnO	CuO/Cu	NiO/Ni	comments
R_0	0.03	0.07	0.20	0.21	Oxygen ratio
Reactivity	←decreasing		increasing→		
Cost	←decreasing		increasing→		
Health & Environm.				-	
Thermodynamics				-	<99.5% conv. for NiO
Reaction with CH4			+		CuO exothermic w. CH4
Melting point			-		1085°C for Cu

Lyngfelt (2008) stated that if the fuel is CO or H_2, the reaction will be exothermic, because using methane as a fuel makes the reaction endothermic except for Cu. Therefore, using Cu gives the process the advantage of maintaining the temperature of the oxygen carrier, which makes the circulation of metal oxide to the air reactor more efficient. According to Table 2-3, it can be also concluded that Nickel oxide and Copper oxide have the higher reactivity compared to the other metal oxides. As a result of previous studies, applying thermogravimetric analysis with methane as the reducing gas, the following results were obtained. CuO-based oxygen carriers, prepared with SiO_2, Al_2O_3 or TiO_2 as inert material, have shown the best properties, with sintering temperatures determined to be in the range of 700-950℃. Based on the findings of previous studies, Copper oxide will be utilized as an oxygen carrier in this work.

2.5 PREVIOUS EXPERIMENTAL WORK ON CLC BY USING A ROTATING BED REACTOR

Up to now, only a few experimental studies have simulated and validated the CLC process with CH_4 as fuel and Copper oxide as an oxygen carrier by using a rotating bed reactor; therefore, the available previous work will be interpreted and discussed in detail in this section. The first obtainable work was carried out by Dahl (2009), when the reactor as described in section 2.3 was utilized with the following dimensions: the four stream sectors (methane, steam, air and steam) were set to $60^{\circ}, 30^{\circ}, 240^{\circ}$ and 30°,

respectively, the outer radius of the middle annular fixed bed was 60 mm, a bed thickness of 1.0 cm and a bed height of 4.0 cm. Needle valves and mass flow meters were set on the two exit chambers to obtain as low as possible pressure drop inside the reactor because Dahl, (2009), stated that pressure differences between the air and methane sides also strongly influence the amount of internal gas mixing.

In Dahl's work, Al_2O_3 was used to prepare a Cu-based oxygen carrier (2 mm spheres) having a > 10% oxygen capacity. Four different total gas flows (300, 600, 900 and 1200 ml/min) with a temperature of 800 ℃ were experimentally measured to test the effect of different flow rates. The gas flow rates of methane, argon and air were fed based on their sector area ($60^{\circ}, 30^{\circ}, 240^{\circ}$ and 30°). As shown in Figure 2-5, at a total gas flow rate of 300 ml/min, 50% of the fed/inlet methane exited from the air sector (B), and 11% of the O_2 and N_2 exited from the methane sector (A), which represented high internal gas mixing. However, as soon as the total gas flow rate gradually increased, the outlet methane from the air sector decreased. For example, in the fourth case where a total flow rate of 1200 ml/min was fed, the outlet methane from the air sector (B) was only 1/3 of the fed methane, and only around 7% of the O_2 and N_2 exited from the methane sector (A).

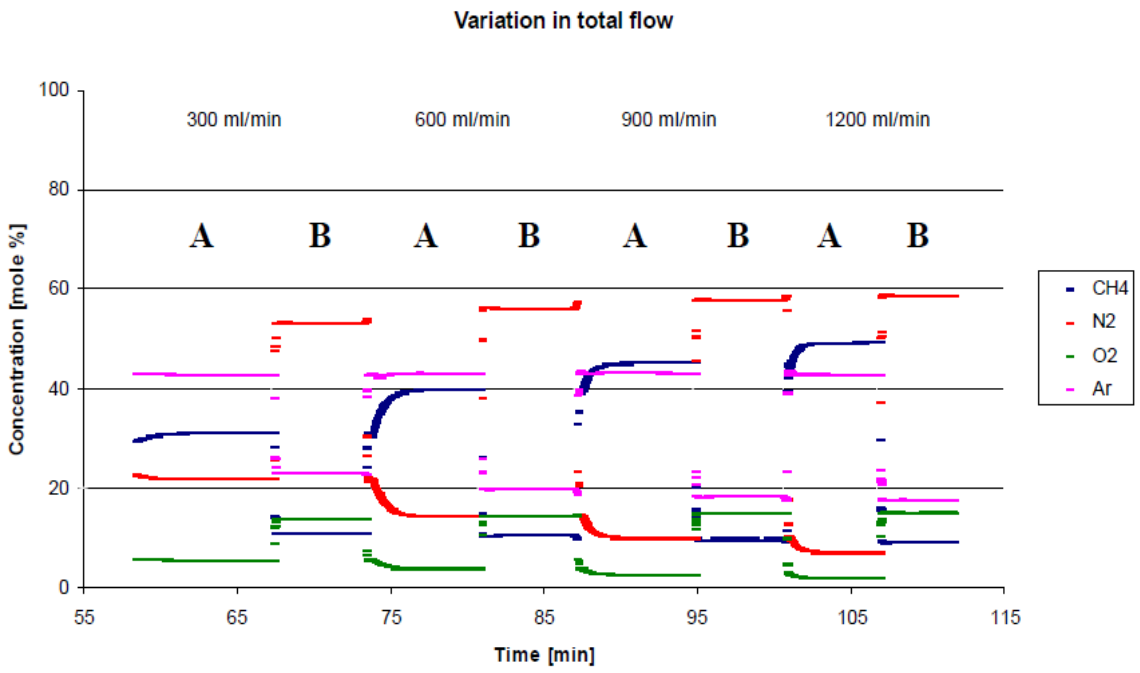

Figure 2-5 (Dahl, 2009): Results from MS analyses of effluent gas from CH_4 side (A) and air side (B) of the rotating reactor.

From the initial test of Dahl's experimental work, (2009), 50% CO_2 capture and 85% CO_2 purity have been accomplished, and internal gas mixing could not be avoided. According to the range of these four flow rates, it can be concluded that a high flow rate (high gas velocity) is required to minimize internal gas mixing. The second obtainable work was performed by Hakonsen (2011), where the reactor described in section 2.3 was used with the following dimensions: the outer diameter of the middle annular fixed bed was 60 mm, the bed thickness was 12 mm, and the bed height was 60 mm. The bed was packed with 120 g of spherical particles of CuO/Al_2O_3 having 10 wt % oxygen capacity. The spherical particles of CuO/Al_2O_3 have a diameter of 1.5 mm and specific surface area of 115 m^2/g, which results in high rest porosity (Hakonsen, 2011). The internal annular feed system was divided into four sectors (methane, steam, air and steam) and set to $60^{\circ}, 30^{\circ}, 240^{\circ}$ and 30°, respectively. Argon was used as an inert to be fed in the both purge sectors. A CuO-based oxygen carrier was used in this experimental work due to its fast kinetics at temperature < 800℃ and to the exothermicity of the both reduction and oxidation reactions (Hakonsen, 2011), as follows:

$$CH_4 + 4CuO \longrightarrow CO_2 + 2H_2O + 4Cu \qquad \Delta H^{\circ}_{red} = -206\ kJ/mol \qquad 2.5$$

$$4Cu + 2O_2 \longrightarrow 4CuO \qquad \Delta H_{ox}^{\circ} = -596\ kJ/mol \qquad 2.6$$

As shown in Figure 2-6, different temperatures (650, 750 and 800℃) of inlet reacting gases were investigated by Hakonsen (2011) to select the most appropriate temperature for the operating conditions. For example, at 650℃, 35 to 62% of CH_4 conversion was obtained, while at 750℃, the CH_4 conversion and CO_2 capture efficiency were 70% and 80%, respectively. However, the best results were obtained at 800℃, when 80% of CH_4 conversion was reached.

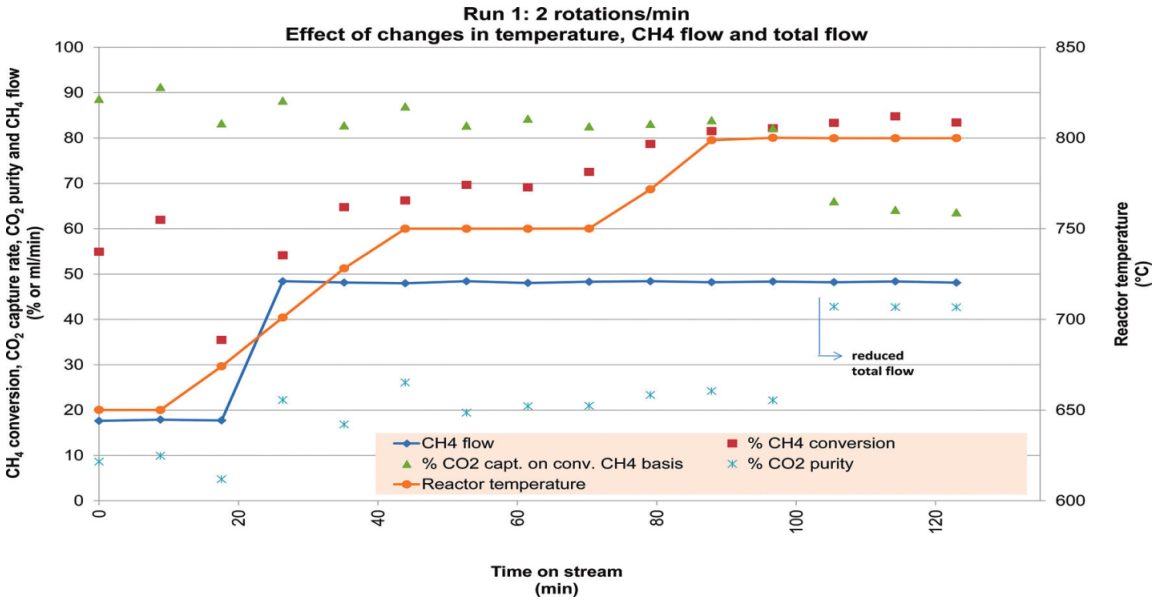

Figure 2-6 (Hakonsen, 2011): The effect of temperature change on reactor performance.

As shown in Figure 2-7, several rotation speeds (1, 2, 3 and 4 rotations/min) were investigated to obtain the best rotation speed for the rotating bed. Among these speeds, Hakonsen (2011) concluded that the highest CH_4 conversion, the highest CO_2 capture efficiencies and the highest potential CO_2 purity were obtained at 2 rotations/min.

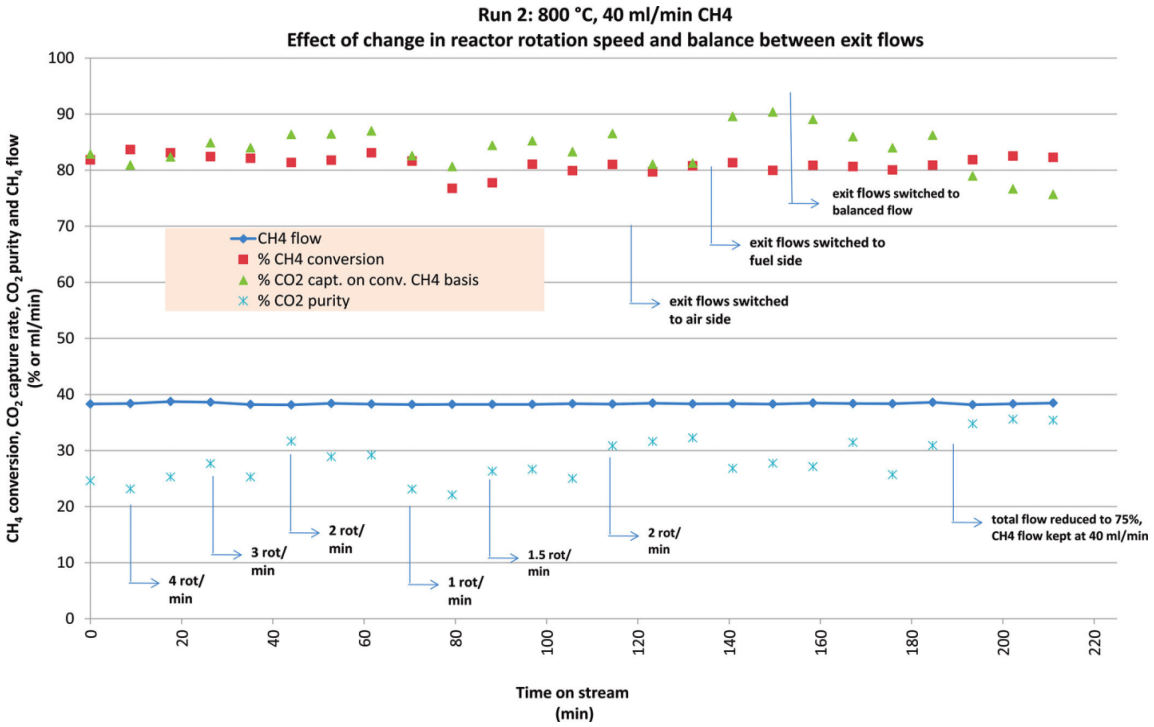

Figure 2-7 (Hakonsen, 2011): The effect of different rotation speeds on reactor performance.

Various gas flow rates of methane, argon and air were experimentally investigated by Hakonsen (2011) to find the optimal operating conditions. The experiment was carried out at a temperature of 800°C and a rotation speed of 2 rotations/min. As shown in Figure 2-8, at the first and last gas flow rates where the total flow rate was 1987 ml/min divided into 1320 ml/min air in the air sector, 84 ml/min argon in each steam sector and 38 ml/min CH_4 plus 295 ml/min argon in the methane sector, good results (83% CH_4 conversion, 90% CO_2 capture efficiency and potential 35% CO_2 purity) were achieved. Also, when the argon flow rate was increased (at 150 min) to 180 ml/min in each steam sector, excellent results were obtained, such as a significant increase in potential CO_2 purity (to around 60%), 80% CH_4 conversion and 90% CO_2 capture efficiency. Hakonsen (2011) suggested that more argon in the inert sectors will suppress mixing between the air and fuel sectors more efficiently. At 90 min, the CH_4 flow rate was reduced to 18 ml/min with the same total flow rate (1987 ml/min); therefore, the low methane flow rate led of course to longer contact time between methane and oxygen carriers, which ultimately resulted in high CH_4 conversion (89%). Increasing the CH_4 flow rate to around 60 ml/min (at 180 min) and further to 100 ml/min (at 225 min) led to a shorter contact time between

methane and oxygen carriers, which resulted in low CH_4 conversion of both flow rates. Based on the findings in Figure 2-8, the best results were accomplished at 150 min, where more argon was fed to obtain potential 60% CO_2 purity, 80% CH_4 conversion and 90% CO_2 capture efficiency. Hakonsen and Blom (2011) indicated that, in the given construction, the major part of the internal gas mixing will be fixed, and that varying the process parameters will only make minor perturbations in performance.

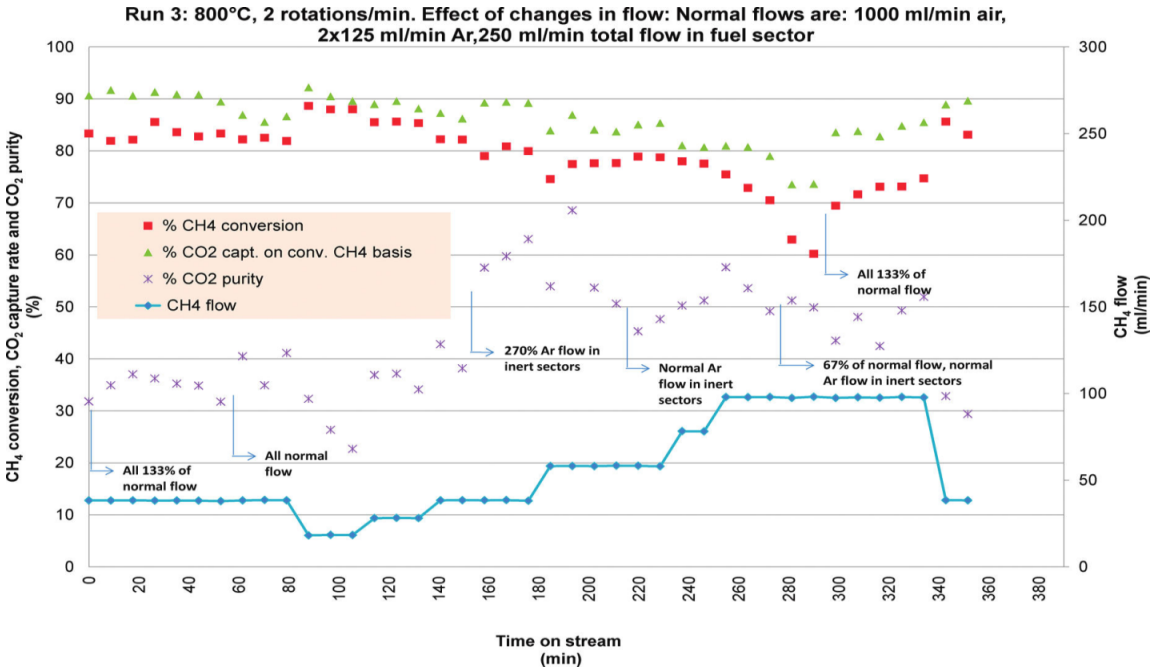

Figure 2-8 (Hakonsen, 2011): experimental run of different gas flows in CLC by using a rotating bed reactor

2.6 SCOPE OF THE THESIS

The aim of the thesis is to investigate, through numerical simulation, the optimal developed design and operating conditions of a rotating bed reactor used in chemical-looping combustion to maximize fuel conversion, CO_2 capture efficiency and energy efficiency. The dissertation is based on a paper of experimental work previously published by Hakonsen and Blom (2011), which was used for model validation. Therefore, the objectives of this study are to:

1. Apply CFD modeling (using COMSOL 4.3b software) of chemical-looping combustion with methane as fuel and copper oxide as an oxygen carrier by means of a rotating bed reactor.
2. Verify modeling results against experimental data by Dahl (2009) and Hakonsen (2011).
3. Improve the reactor's design and operating conditions, such as bed thickness and gas flow region in order to optimize performance of the prototype reactor with no internal gas mixing.
4. Determine the best operating conditions, for example, bed rotating frequency in order to obtain high combustion efficiencies, i.e., high fuel conversion, high CO_2 capture efficiency and high potential CO_2 purity.

CHAPTER 3. METHODOLOGY

3.1 TWO PHASE GAS/SOLID MODEL

Due to improvements in numerical methods and other technology, there has been a significant reduction in the time required to use the computational fluid dynamics (CFD) code. Because of this time reduction, two phase CFD-based models that handle complex gas-solid hydrodynamics and chemical reactions are now achievable. In the previous literature regarding chemical-looping combustion, mathematical modeling was developed to simulate the performance of the fluidized bed reactor using various types of fuel with different oxygen-carriers (CuO, NiO, Fe_2O_3, CoO, etc.). However, until now, no available models have been validated for a rotating bed reactor against experimental data by Dahl (2009) or Hakonsen (2011).

Prior to this study, only limited experimental work had been done with respect to chemical looping combustion using a rotating bed reactor. Moreover, the work was almost entirely focused on the development of operating conditions, such as operating temperature, rotation frequencies, and gas flow rate. There was thus a need to investigate the design of rotating bed reactor. Therefore, in this study, the model's development will focus on the reactor design and with the operating conditions required to perform methane combustion using a CuO-based oxygen-carrier within a chemical looping combustion system. The modeling of gas-solid hydrodynamics and chemical reaction kinetics of the rotating bed reactor will be developed and performed by means of the CFD software, COMSOL.

3.2 ACTUAL GEOMETRY MODELLED

The packed bed reactor is one of the most widely used reactors in the chemical industry for heterogeneous catalytic processes. The reactor consists of a container, such as a tube, pipe, or other vessel that is filled with catalyst particles as a packing material. The packing can be randomly filled with small objects (e.g., Raschig rings) or it can be specifically structurally designed. The modeling challenge of mass and energy transport in the packed bed reactor is affected by the formatted structure of the packed catalyst particles. In most cases, the structure in between particles is described as macro-porous,

while the pore structure inside the catalyst particles are described as the microstructure. This model presents a simple and fast route to studying micro-scale and macro-scale mass transports along with heterogeneous reactions of a packed bed reactor. Mass and reaction distribution within catalyst pellets along the reactor are provided. A packed bed can be used in the distillation process, in a scrubber, or in a chemical reactor, such as a Continuous Stirred-Tank Reactor (CSTR), a Plug Flow Reactor, and a Semi-batch Reactor.

A type of Plug Flow Reactor called a rotating bed reactor is used in chemical looping combustion to carry out the combustion of methane as a fuel and copper oxide (oxygen carrier) as a packing material. The reactor (see Figure 3-1) contains three main systems: the first is a feeding system that is divided into four sectors, where gases (methane, steam, air and steam) can be fed radially into the second system. The second system is a rotating packed bed, where spherical copper/copper oxide particles 1.5 mm in diameter are packed and rotated around the feeding system to adsorb and transfer oxygen from the air into methane. The third system is an outlet system that is divided into two exit chambers separated by two rigid walls, where flue gases can be separated and stored from both reacting sides. The central red part is a heater that heats up the fed gases to an appropriate operating temperature. The rotating bed reactor has the following dimensions: a 60-mm outer diameter; a 12-mm bed thickness; and a 60-mm bed height, these dimensions were used in previous experimental work by Hakonsen (2011).

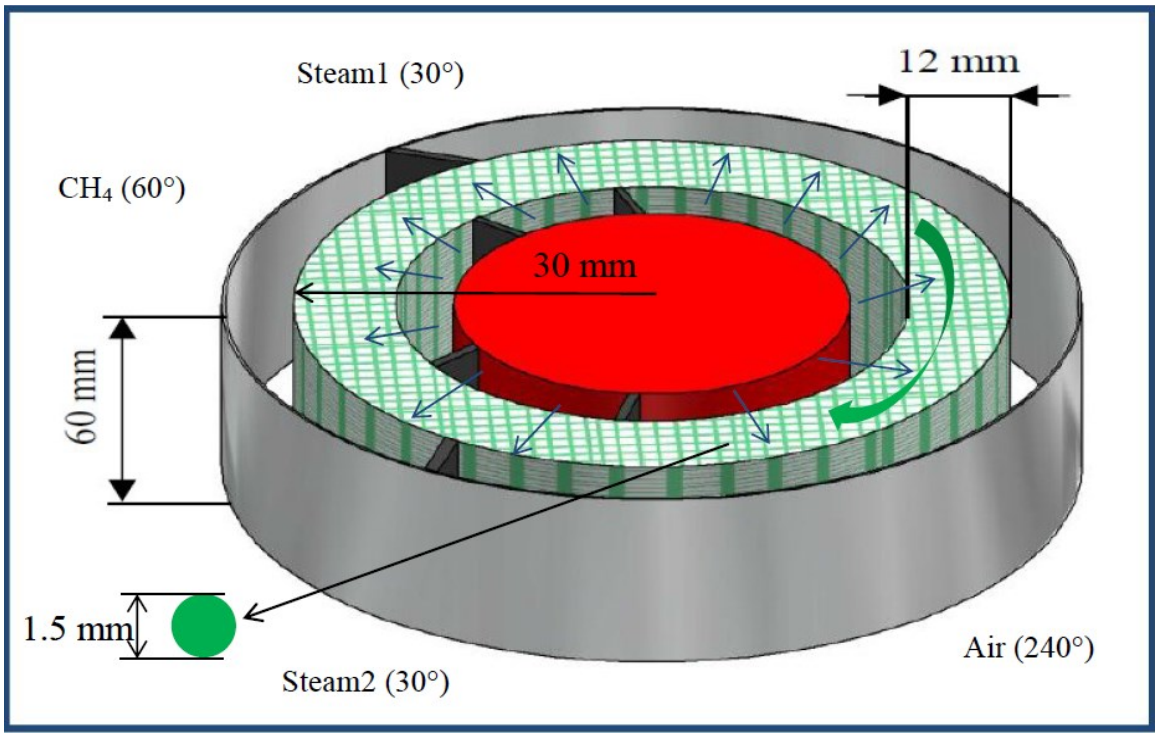

Figure 3-1 Three-dimensional schematic drawing of a rotating bed reactor along the rotation axis.

In this modeling work, to simplify the design of the rotating bed reactor's geometry and avoid simulating any intricate physical movements of the packed particles, a slice of the rotating packed bed was used to represent the rotating bed. The slice (see Figure 3-2) had the following dimensions: the 12 mm length (x axis) represented the rotating bed thickness, and the 0.75 mm thickness (y axis) represented the particle's central distance. The slice was assumed to contain the first row of the copper oxide/copper particles that had connected and travelled over the four gas streams (methane, steam, air and steam). With 12 mm bed thickness and 1.5 mm particle diameter, each single slice has 8 particles when they packed linearly. The slice thus shows the position, along with the percentage of reduction and oxidation of the first particles that have moved over the two reacting gas sectors (methane and air).

The slice is assumed to be stationary as a flat porous bed, while the four gas streams (methane, steam, air and steam) flow alternately over the slice for a specific time. They then diffuse and react on the surface of the solid. The simulation, as illustrated in Figure 3-2, has two domains: the first domain is for the gas phase, where diffusion,

convection and flux with constant feed velocity and different periods of time for each gas stream, take place in the flow channel, having 120 cells in x direction (12 mm length). A homogeneous distribution of solid in the reactor was assumed, which resulted in average particles in each cell have a radius of 0.75 mm that is larger than the cell itself. The pressure drop of each gas stream within the flow channel can be obtained by means of the Ergun equation (Equation 3.8), and was typically found to be negligible. The second domain is for both phases (gas/solid interface), where the diffusion and chemical reaction of gases, controlled by each cell in x direction within the first domain, radially take place on the surface of the solid in only y direction having 50 cells over the particle's central distance. Therefore, there is no interaction or diffusion between the particles in x direction ($D_x = 0$) belongs to different gas cells. The flux of gases between the two domains is controlled by chemical reaction, reduction, and oxidation of gases on the surface of the solid in the second domain.

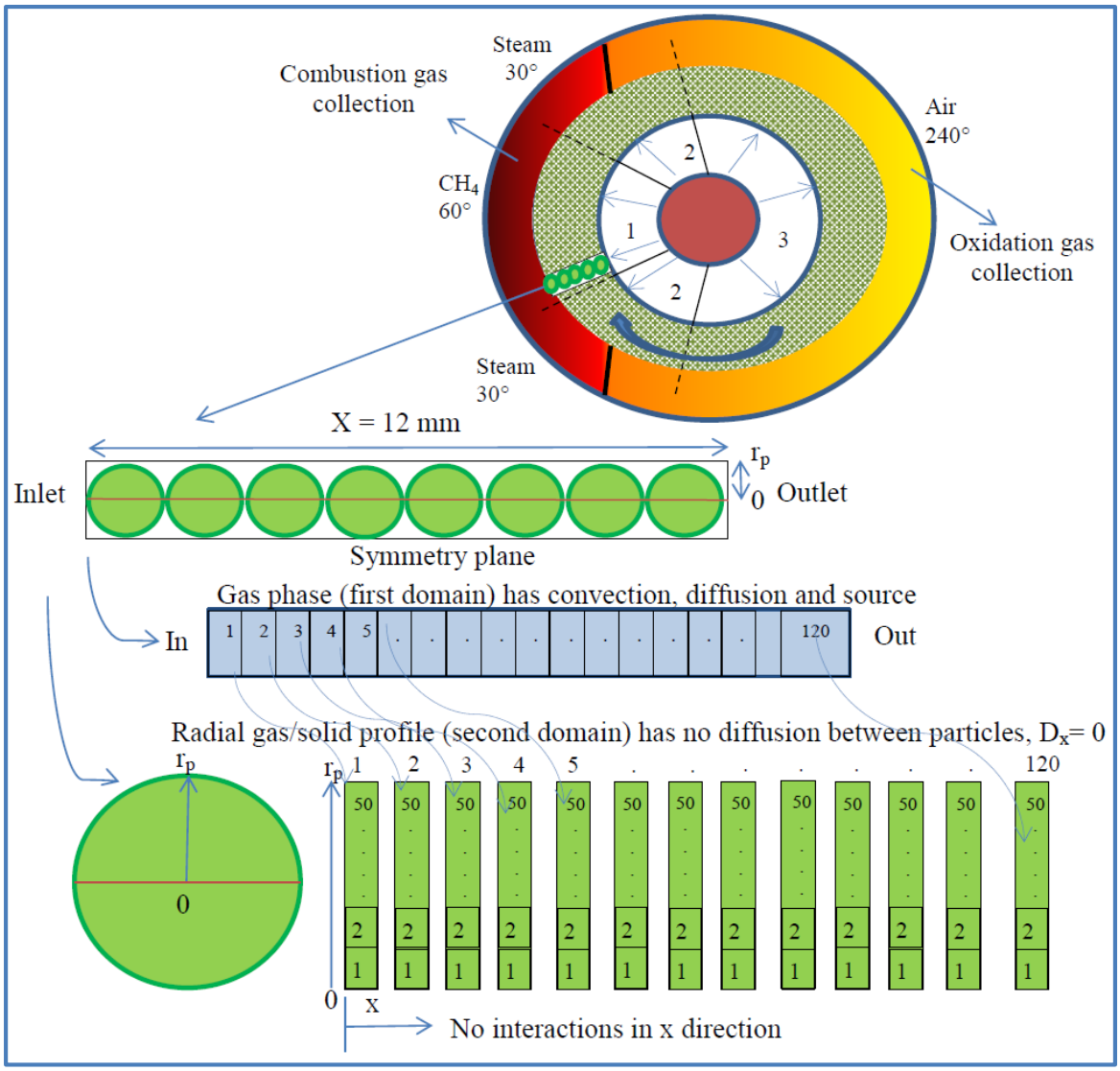

Figure 3-2 Schematic drawing of a slice of the rotating packed bed along the rotation axis.

3.3 THE MAIN ASSUMPTIONS OF THE MODEL

i) It includes two phases: gas and solid.

ii) The bed is assumed to be flat and porous with spherical particles of uniform size.

iii) The void fraction of the rotating bed is assumed as that of a packed bed with a gas volume fraction (ε_g) in the range of 0.3 – 0.5 (McCabe, 2001).

iv) Based on the previous experimental work by Hakonsen (2011), a temperature of 800℃ has been selected as the operating temperature of the inlet reacting gases.

v) Isothermal conditions were assumed, given the similar heats of reaction in both the oxidation and combustion regions.

3.4 GAS-SOLID HYDRODYNAMICS

The mass transport equation for gases when diffusion and convection were applied within the first domain is:

$$\frac{\partial C_i}{\partial t} + \nabla \cdot (-D_{AB} \nabla C_i) + u \cdot \nabla C_i = S \qquad 3.1$$

where C, t, D_{AB}, u are the gas concentration (mol/m^3), time (s), the bulk mass diffusivity of gases (m^2/s) within gas phase, and the linear velocity gases within the flow channel which representing the superficial velocity in the packed bed, respectively. S denotes the source term (mol/m^3 s) of the first domain, which represents the flux of gases entering or leaving the solids over the second domain due to the reactions and the concentration gradients taking place on the outermost part of the solids (diffusion controlled), as illustrated in Figure 3-3.

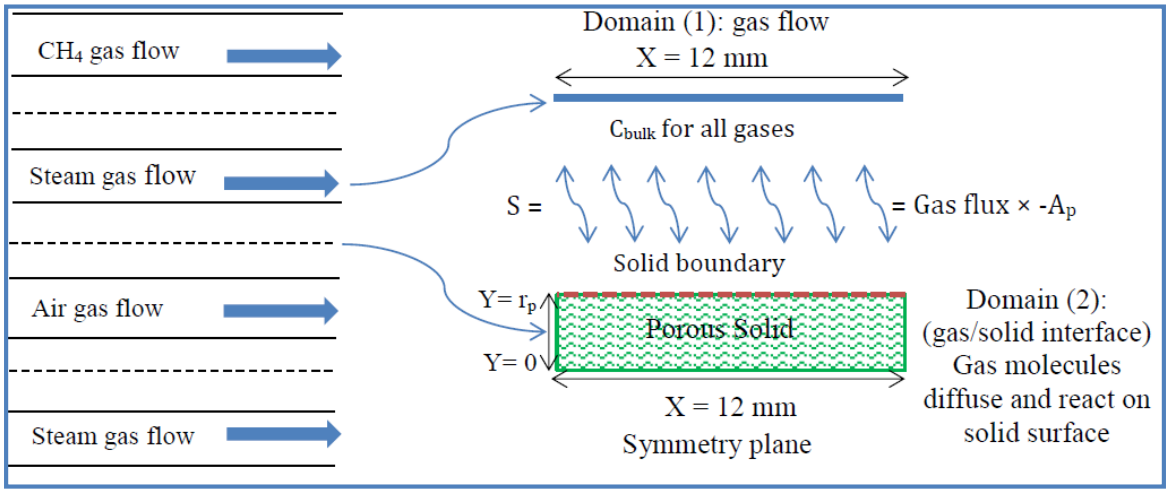

Figure 3-3 Schematic drawing of gas/solid interface between the two domain representing the source term (S) of the first domain.

$$S = -A_p \times Gas\ flux \tag{3.2}$$

where *Gas flux* (mol/m^2.s) in the second domain is the flux of gases entering or leaving the solids due to the reactions and concentration gradients controlled by diffusion in y direction over the interfacial area of the boundary between the gas domain and solid domain. A_p denotes the surface area of particles per unit volume of gas cell, which calculated from a single particle in domain 2 to number of particles in cell of domain 1.

$$Gas\ flux = D_e \frac{\partial c}{\partial y} \tag{3.3}$$

$$A_p = \frac{surface\ area\ of\ particles}{unit\ volume\ of\ gas\ cell} \tag{3.4}$$

$$A_p = \frac{4\pi r_p^2 \times number\ of\ particles\ per\ volume}{gas\ cell\ volume} \tag{3.5}$$

where

$$number\ of\ particles = \frac{volume\ of\ solid}{{}^4/_3\,\pi r_p^3} \tag{3.6}$$

It would be accurately investigated if the actual geometry of the rotating bed reactor simulated as 2D in the first domain and 3D in the second domain, for proper tracking of the gas continuity. However, a test of a simplified 1D/2D model typically took 24 hours for a simulation with only 2 rotations per minute when performed on Intel (R) Xeon (R) CPU processor with 64 GB of ram. A 2D/3D model with even 5 cells in the extra direction would be expected to take several days per run to carry out a simulation with only one or two rotations per minute. Therefore, the simple approach was adapted due to time considerations. The use of a 2D/3D approach is a possible area for future work. In order to simply and apply a 1D/2D model, an assumption of having constant gas flow area and constant solid holdup across the bed thickness were discussed and carried out with this model. In the actual system of the rotating bed reactor as shown in Figure 3-4 a, 67% increase in flow area is applied as gases travel through the reactor. Therefore, reduced velocity at the outer edges of the geometry is expected. Because of a radial flow through the geometry, the gas will decelerate as if moves out of the system. In the current

modeling system, the change in flow area was neglected, and the net solid content within the annular region was averaged over the bed thickness, as illustrated in Figure 3-4 b. Thus, the actual system was simulated as described in section 3.2, illustrated by Figure 3-4 c. Gas velocity was set based on the inlet gas velocity. An average solid capacity was determined to match the validation results of the experimental work (see section 4.1), providing a calibrated base simulation which is intended to describe the performance of the rotating system.

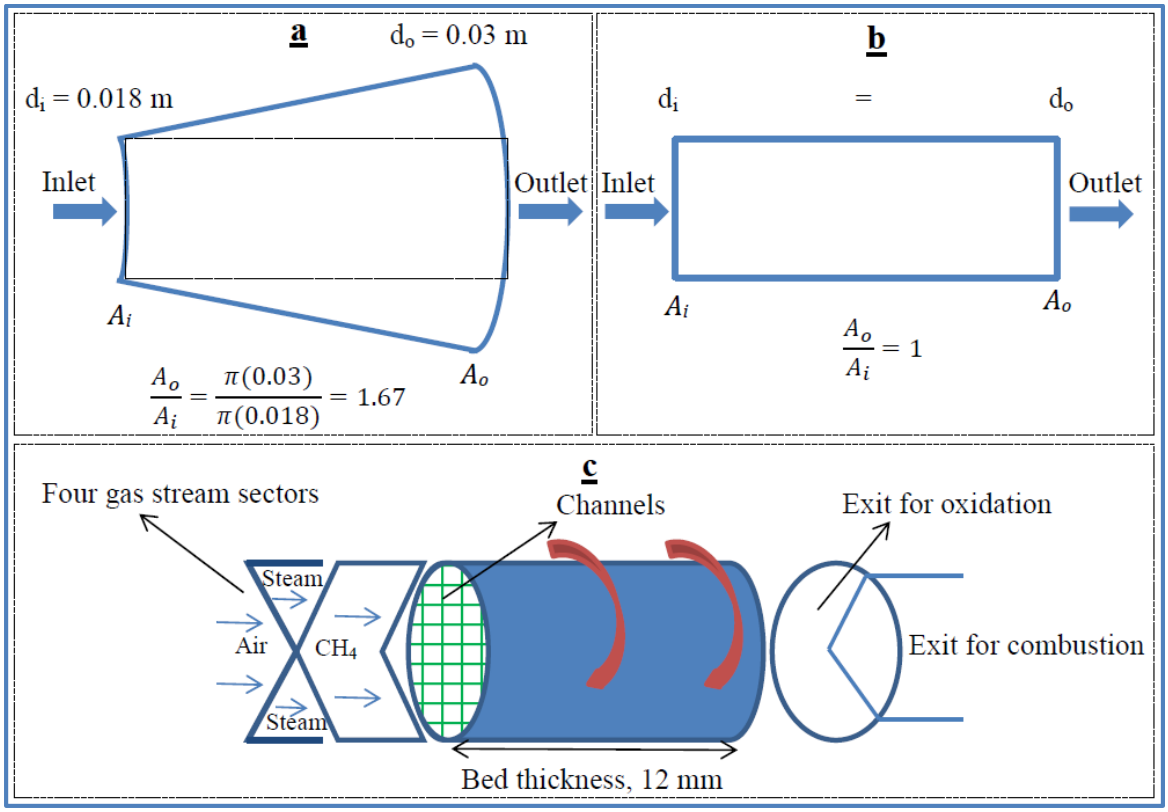

Figure 3-4 Schematic drawing of flow area and solid holdup across the bed of both the actual system and the current modeling system.

The pressure drop equation for flow in the x-direction of the first domain, was

$$PX + \beta * \left(\frac{F}{F_o}\right) * \left(\frac{P_o}{P}\right) = 0 \qquad 3.7$$

where β is the Ergun equation constant represents the pressure drop within the packed bed reactor obtained by the Ergun equation, (Fogler, 2006).

$$\beta = \left(-\frac{\rho u}{\rho g_c D_p}\right)\frac{(1-\emptyset)}{\emptyset^3}\left[\frac{150(1-\emptyset)\mu}{D_p} + 1.75\rho u\right] \quad 3.8$$

where $\emptyset$ is the porosity, D_p the particle diameter (m), μ the gas viscosity (pa.s), ρ the gas density (kg/m^3), and u the reactor flow velocity (m/s) that depends on the pressure drop. Hence, according to the following equation:

$$u = u_{feed} \cdot \frac{C}{C_{feed}} \cdot \frac{P_{feed}}{P} \quad 3.9$$

where u_{feed} is the inlet velocity and C the total concentration (mol/m^3), and P_{feed}/P is the inverse pressure ratio relative to feed conditions (typically ~ 1).

Since no convection was applied between gases and solids in the second domain, the mass transport equation of gases within the second domain (gas/solid interface) can be concluded from equation 3.1, based on diffusion in only y direction as follows:

$$\frac{\partial C_i}{\partial t} + \nabla \cdot (-D_e \nabla C_i) + u \cdot \nabla C_i = R \quad 3.10$$

$$-D_e \nabla C_i = \left(-D_e \times \frac{\partial C}{\partial y}\right) \quad 3.11$$

$$u \cdot \nabla C_i = 0 \quad 3.12$$

$$\frac{\partial C_i}{\partial t} - D_e \frac{\partial^2 C}{\partial y^2} = R_i \quad 3.13$$

where C_i, and D_e are the gas concentration (mol/m^3) and effective diffusivity (m^2/s) of gas species i within the solids. R_i denotes the source term (mol/m^3 s) of the second domain which represents the chemical reaction on the surface of solid.

The mass continuity equation for Cu and CuO solids within the second domain, where no convection or diffusion applied is similar:

$$\frac{\partial C_i}{\partial t} = R_i \quad 3.14$$

where C and t are the solid concentration (mol/m^3) and time (s), respectively. R_i denotes the source term (mol/m^3 s) of the second domain which represents the chemical reaction on the surface of the solid. The particle was assumed to be composed by

spherical grains of CuO, which reacts following a shrinking core model (SCM) controlled by a chemical reaction and diffusion in the grain surface.

3.5 SHRINKING-CORE MODEL

The shrinking-core model (SCM) is used to describe situations in which solid particles are consumed either by dissolution or reaction, and hence the amount of material being consumed is said to be "shrinking". The SCM was developed to be applied to a variety of fluid-solid applications, such as catalyst regeneration and pharmacokinetics. The SCM has also been exploited in the literature to describe the CLC kinetics of the oxygen carrier reduction and oxidation (Sedor, 2008). As illustrated in Figure 3-5, the reaction first takes place on the outer surface of the particle. Then, as the reaction progresses, the gaseous reactants diffuse through the product layer to reach the unreacted core.

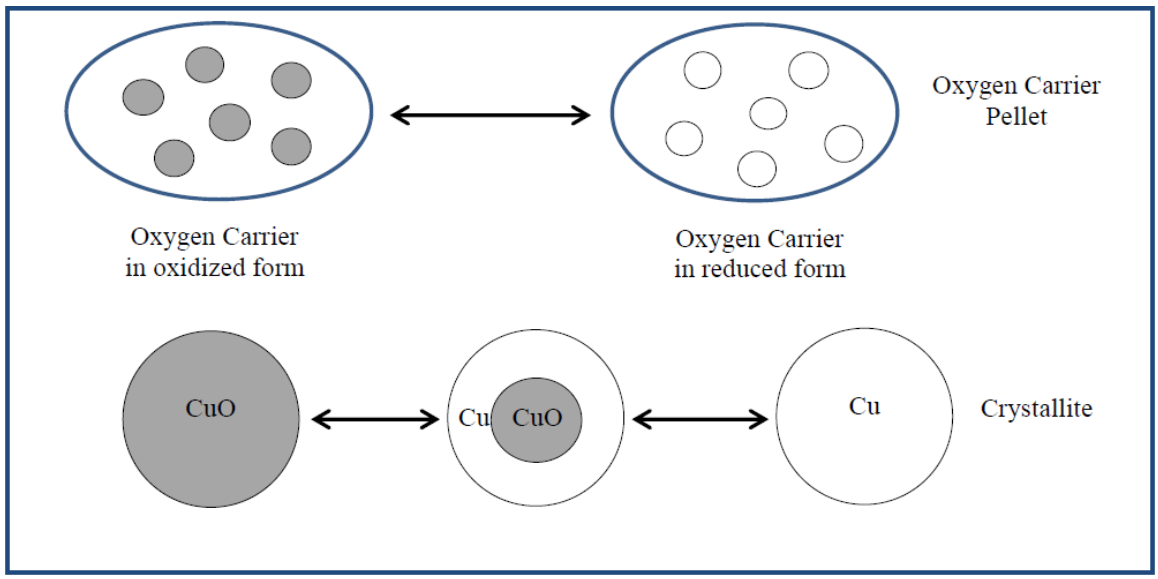

Figure 3-5 Scheme of the shrinking-core model applicable to a CuO/Cu crystallite.

Some assumptions were made in order to apply the shrinking-core model, as follows: (1) the porosity of the oxygen carrier crystallites is neglected; (2) the crystallites are considered spherical; (3) the reaction is first order with respect to the concentration of reactant gas; (4) the crystallite volume is constant during the reaction; and (5) the reaction is isothermal. Therefore, to determine the kinetic parameters of the following reduction

and oxidation reactions of the oxygen carrier (CuO/Cu), the shrinking-core model with the reaction controlled by chemical reaction in spherical grains was used.

$$CH_4 + 4CuO \longrightarrow CO_2 + 2H_2O + 4Cu \quad 3.15$$

$$4Cu + 2O_2 \longrightarrow 4CuO \quad 3.16$$

The reduction of CuO was assumed to proceed towards Cu in one step. In other words, the partial reduction to Cu_2O was not considered. The equations that describe the oxidation and reduction of Cu/CuO under the chemical reaction control in the geometry of spherical grain for this model are as follows, (Abad, 2010):

$$\tau_i = \frac{\rho_m r_g}{b_i K C_i^n} \quad 3.17$$

Where the rate constant follows an Arrhenius type dependence with temperature

$$K = k_0 e^{-E/RT} \quad 3.18$$

The reaction rate of the solid as an oxygen carrier and gas as a fuel were obtained by

$$R_{CuO} = A_{oxy} e^{-E_{oxy}/RT} C_{O_2} - A_{red} e^{-E_{red}/RT} C_{CH_4} \quad 3.19$$

$$R_{CuO} = -R_{Cu} \quad 3.20$$

$$-R_{CH_4} = R_{CO_2} = 0.5 R_{H_2O} = 0.25 A_{red} e^{-E_{red}/RT} C_{CH_4} \quad 3.21$$

$$-R_{O_2} = 0.5 A_{oxy} e^{-E_{oxy}/RT} C_{O_2} \quad 3.22$$

Where A_{oxy}, E_{oxy}, A_{red} and E_{red} are based on the work by Abad (2007) and have values of 4.5×10^{-6}, 15000 (J/mol), 4.7×10^{-6} and 60000 (J/mol), respectively for the stoichiometric basis used in this work.

3.6 EFFECTIVE DIFFUSIVITY

The pores in the pellet are a series of tortuous pathways that interconnect pore bodies and pore throats at varying cross-sectional areas. Individual diffusion is not beneficial but easily described within each tortuous pathway; consequently, an effective diffusion coefficient, as the average diffusion taking place at any position r (radius) in the

pellet, was developed and carried out. Radial variations in the concentration based on the total area (voids and solid) are thus considered to be diffused rather than a void area alone. The effective diffusivity, D_e, of either the bulk or the Kundsen diffusivity can be presented by the following equation (Fogler, 2006). This takes into account some assumptions, such as that the paths are tortuous, the pores are of varying cross-sectional areas, and not all of the areas normally in the direction of the flux are available for the molecules to diffuse. Against these assumptions:

$$D_e = \frac{D_{AB}\phi_P\sigma_c}{\tilde{\tau}} \tag{3.23}$$

where

$$\tilde{\tau} = \text{tortuosity} = \frac{\text{Actual distance a molecule travels between two points}}{\text{Shortest distance between those two points}} \tag{3.24}$$

$$\phi_P = \text{pellet porosity} = \frac{\text{Volume of void space}}{\text{Total volume (void and solid)}} \tag{3.25}$$

$$\sigma_c = \text{Constriction factor}$$

Typical values of the constriction factor, tortuosity, and pellet porosity calculated by (Fogler, 2006) are, σ_c = 0.8, $\tilde{\tau}$ = 3.0, and ϕ_P = 0.40, respectively. Within this work, ordinary molecular diffusion coefficients, D_{AB}, for binary dilute gas mixtures of A and B that depend linearly on the average kinetic speed of the molecules and the mean free path of the gas, are predicted in units of cm^2/s, via the Chapman-Enskog equation (Belfiore, 2003):

$$D_{AB} = \frac{1.86 \times 10^{-3}[T(K)]^{3/2}\left[\left(\frac{1}{MW_{A)}}\right) + \left(\frac{1}{MW_B}\right)\right]^{1/2}}{p\ (atm)\left[\sigma_{AB}(Å)\right]^2 \Omega_D \left(\frac{kT}{\varepsilon_{AB}}\right)} \tag{3.26}$$

Accurate values of the collision integral, Ω_D, for the Lennard-Jones potential can be obtained from the following empirical correlation:

$$\Omega_D \approx A(T^*)^{-B} + C\exp(-DT^*) + E\exp(-FT^*) + G\exp(-HT^*) \quad 3.27$$

where

$$T^* = \frac{kT}{\varepsilon_i} \qquad A = 1.06036 \qquad B = 0.15610$$

$$C = 0.19300 \qquad D = 0.47635 \qquad E = 1.03587$$

$$F = 1.52996 \qquad G = 1.76474 \qquad H = 3.89411$$

For a binary gas mixture of A and B, an estimate of the Lennard-Jones parameters required to calculate D_{AB} via empirical averaging is as follows:

$$\sigma_{AB} = \frac{\sigma_A + \sigma_B}{2}, \qquad \varepsilon_{AB} = \sqrt{\varepsilon_A \varepsilon_B} \quad 3.28$$

$$D_e = D_{AB} \times 0.106666 \quad 3.29$$

3.7 MODELING METHODOLOGY

Comsol multiphysics 4.3b is used to simulate the mass transport processes of a rotating bed reactor inside a model with two domains. The first domain is for the gas phase, where the diffusion and flux of different gas streams (CH_4, CO_2, H_2O, O_2 and N_2) take place in a 1D flow channel. The geometry (flow channel) of the first domain is shown in Figure 3-6. The figure shows 120 as the number of elements set for the interval, with 0 at the left endpoint and 0.012 m at the right endpoint. These, represent the bed thickness, where the four gas streams (methane, steam, air and steam) flow alternately from 0 to 0.012 m. The second domain is for two phases (gas/solid interface), where the diffusion and chemical reaction of gases, controlled by the first domain, take place on the surface of the solid represented by a 2D slice of a flat porous bed. The geometry (flat porous bed) of the second domain is shown in Figure 3-7. In this figure, 50 is set as the number of elements at the 0.00075 m height of the rectangle (representing the particle radius) and 120 is set as the number of elements at the 0.012 m width of rectangle

(representing the bed thickness). Because of the validated symmetry assumption, only one slice representing the rotating bed is needed.

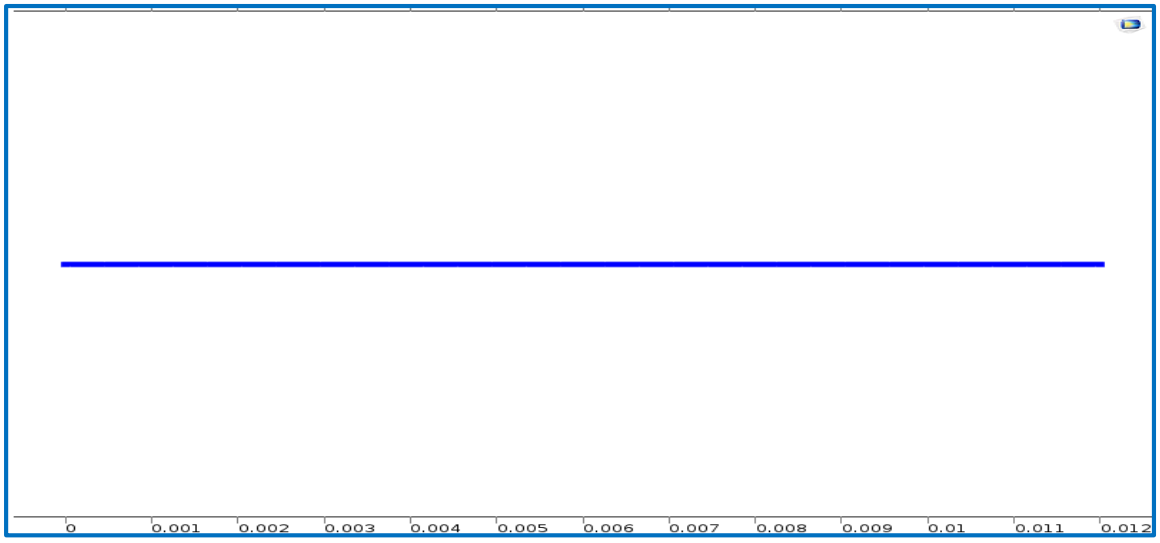

Figure 3-6 Geometry 1 representing the flow channel for the first domain in the model

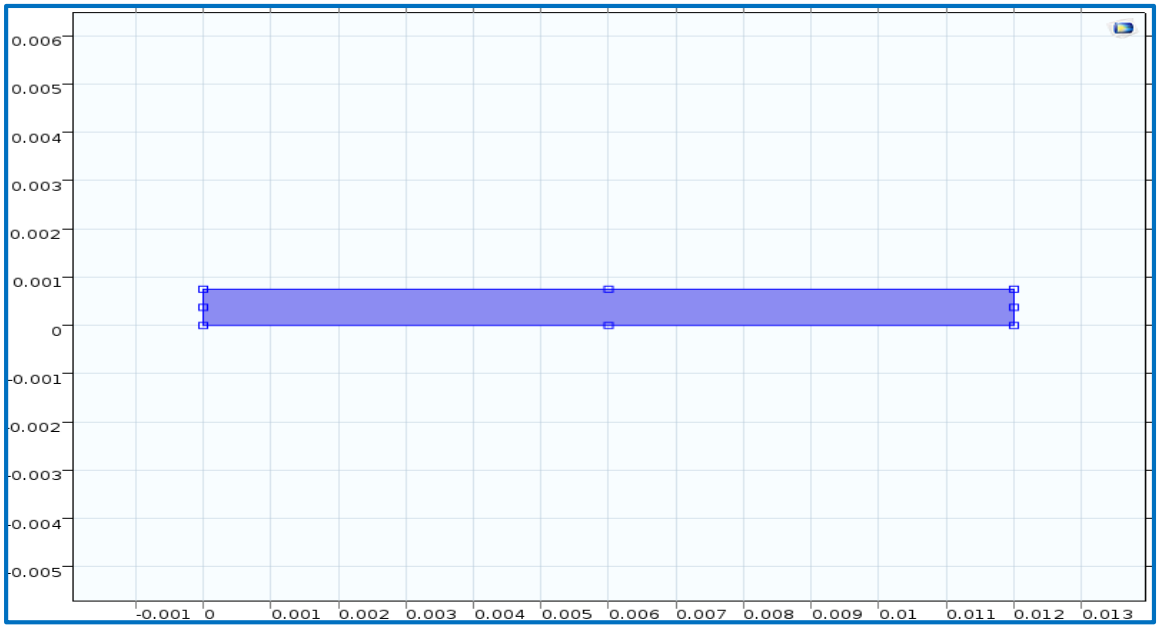

Figure 3-7 Geometry 2 representing the flat porous bed for the second domain in the model

To set up the model, start by creating the first domain for the gas phase. The transport of Diluted Species was selected as the physics user interface for the reactor

mass transport. Five gas streams either entered or produced (CH_4, H_2O, CO_2, O_2 and N_2) as inflow/outflow boundary conditions. The outflow boundary condition was set to have a constant outlet pressure. The feed velocity was set by creating time dependent boundary conditions for each gas stream and composition. The pressure drop in the reactor is described by the Ergun equation (Equation 3.8) for packed bed reactor, where the coefficient form PDE (partial differential equation) was applied within the first domain with the reactor flow velocity (u) that depends on the pressure drop according to Equation 3.9. Initially, both the flow channel in the first domain and the flat porous bed in the second domain were assumed to have a concentration of steam (H_2O).

To control the flux of gases between the two domains, diffusion of each gas stream onto the surface of the flat porous bed, followed by the chemical reaction of the reacting gases on the solid surface, was applied in the second domain using the Transport of Diluted Species as the physics user interfaces. The concentration, velocity and diffusion of gases on the surface of the solid controlled by the first domain were set for the second domain. The velocity of gases within the second domain was set to zero at the inlet/outlet direction where no flux takes place in the second geometry. The rate of concentration over time was calculated by Equation 3.13, where diffusion and chemical reactions, reduction and oxidation (Equations 3.15 and 3.16), of gases on the solid surface (described by shrinking core model) were taken into consideration. Note that no diffusion in the x-direction was allowed within the second domain.

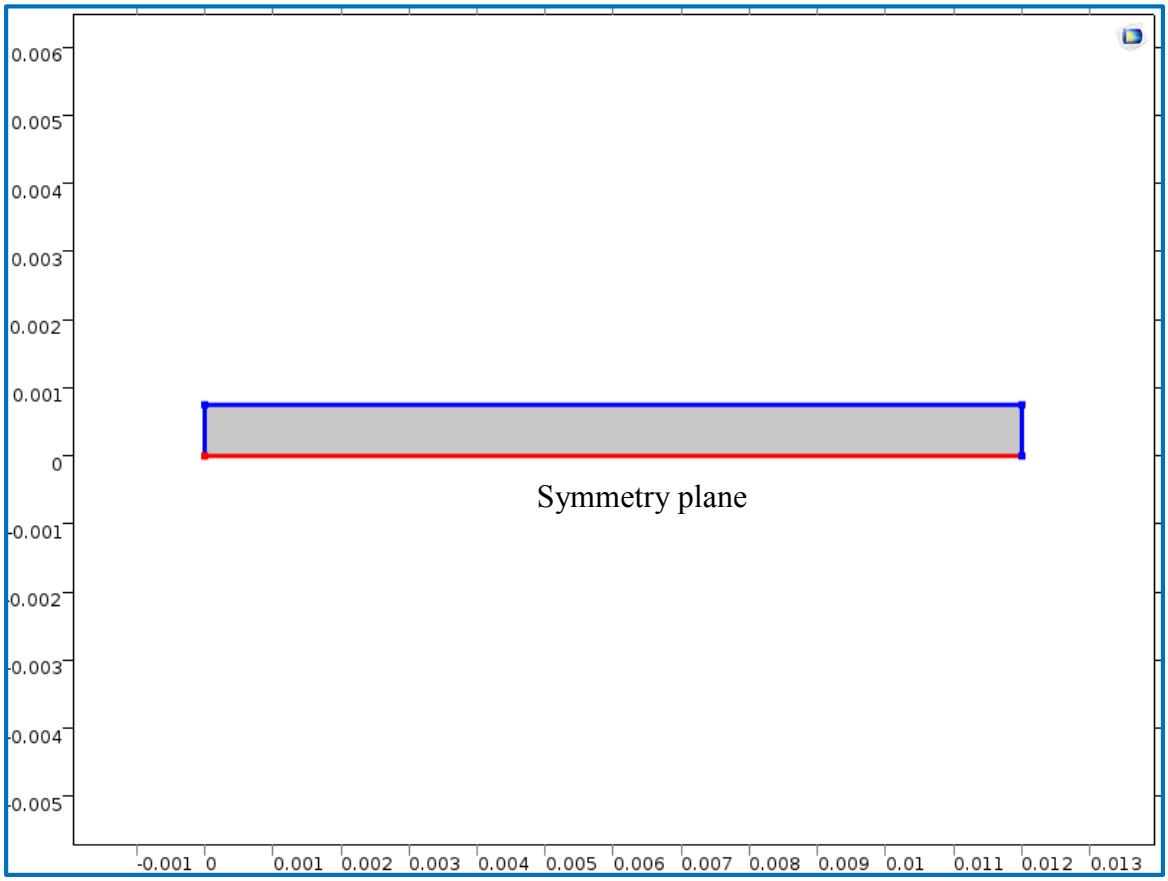

Figure 3-8 Geometry 2 of the second domain where no flux takes place on the solid surface and symmetry plane was applied.

The mass transport of Cu and CuO solids within the second domain was carried out by setting a new Transport of Diluted Species, where only chemical reactions, reduction and oxidation of solids were applied according to Equations 3.15 and 3.16. Diffusion was set to very small values (0.000000001 cm^2/s) for Cu and CuO. No flux was applied for the solid, as shown in Figure 3-8. The second domain was initialized with a concentration of 45.3 mol/m^3 of CuO based on capacity validation models. The time stepping for the simulation as managed by Comsol's built-in stability and relative accuracy parameters. The physical properties of the rotating bed reactor are provided in Table 3-1.

Table 3-1 Physical properties were applied within modeling runs for all cases.

Symbol	Value[unit]	Definition
P_{feed}	1[atm]	Feed pressure
T	1073[K]	Temperature
D_{CuO}	1e-13[m^2/s]	Diffusion coefficient for CuO
D_{Cu}	1e-13[m^2/s]	Diffusion coefficient for Cu
E_1	60000[J/mol]	Activation energy for R_1
k_1	98363[1/s]	Pre-exponential factor for R_1
u_{feed}	$V_{feed}/A_{feed}/0.3$	Linear inflow velocity
ΔHr_1	-49.20225[cal/mol]	Heat of reaction for R_1
kp	0.779[W/(m*K)]	Thermal conductivity
ε_b	0.45	Porosity of the bed (void/total)
ρ_p	1808.5789[kg/m^3]	Density of pellet
Rr	$4*A_{feed}/(2*(60/360*0.018[m]*3.14159*2+0.06[m]))/2$	Reactor radius
Ra	A_{feed}	Reactor area
C_{tot_feed}	$P_{feed}/R/T$	Total feed concentration
$x_{\_CH4\_feed}$	0.115	Molar fraction of CH_4 in feed
$CuO_{\_Capacity}$	45.3[mol/m^3]	Molar fraction of CuO in solid initially present
$x_{\_H2O\_feed}$	$(1-x_{CH4feed})$	Concentration of inert in feed (steam)
A_p	2200[m]	Surface area of particles per unit volume
r_p	0.00075[m]	Particle radius
V_{feed}	5.5e-6[m^3/s]	Inlet Volumetric Flow Rate
A_{feed}	60/360*.018*3.14159*2*.06[m^2]	Cross-section for flow
D_{AB}	0.0001781[m^2/s]	Diffusion coefficient for CH_4
D_{AB}	0.0001781[m^2/s]	Diffusion coefficient for CO_2
D_{AB}	0.0001781[m^2/s]	Diffusion coefficient for H_2O
E_2	15000[J/mol]	Activation energy for R_2
k_2	100.7333[1/s]	Preexponential factor for R_2
ΔHr_2	-142.3522[cal/mol]	Heat of reaction for R_2
$x_{\_O2\_feed}$	0.21	Molar fraction of O_2 in feed
$x_{\_N2\_feed}$	$(1-x_{O2\_feed})$	Molar fraction of N_2 in feed
D_{AB}	0.0001781[m^2/s]	Diffusion coefficient of O_2
D_{AB}	0.0001781[m^2/s]	Diffusion coefficient of N_2
$x_{\_SH2O\_feed}$	1	Molar fraction of SH_2O
D_{AB}	0.0001781[m^2/s]	Diffusion coefficient for SH_2O

CHAPTER 4. RESULTS AND DISCUSSION

4.1 Investigation of CuO capacity required for 80% CH_4 conversion

To determine the equivalent concentration (or capacity) of the simulated solid material for oxidation and reduction, the simulated capacity was adjusted until the experimental optimum conditions reported by Hakonsen (2011) were obtained (see Figure 2-8). These conditions corresponded to two rotations per minute (2 RPM) at a 150 min operating time, when 80% CH_4 conversion, above 60% CO_2 purity, and 89% CO_2 capture efficiency were acquired. Ten simulations with varied values of copper oxide (CuO) capacity were investigated (Figure 4-1), from which 45.3 mol/m^3 of CuO gives the closest results for CH_4 conversion and CO_2 purity to the noted experimental results. The work of Hakonsen (2011) was used as a validation case prior to the analysis of the effects of different operating parameters and bed configurations on overall performance.

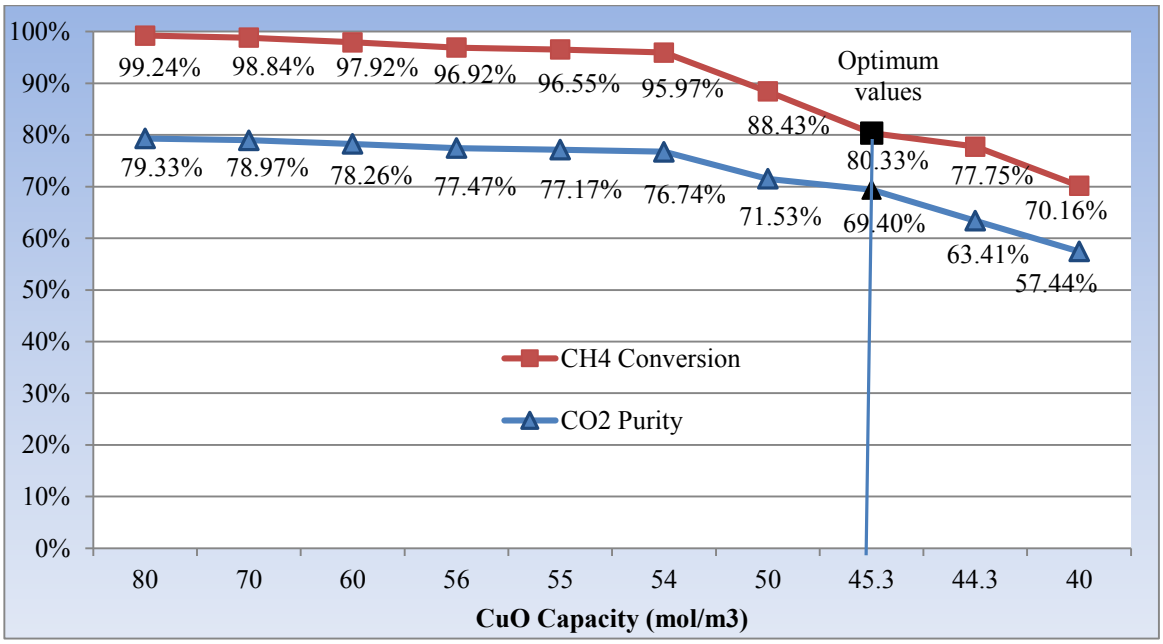

Figure 4-1 Analysis of CuO capacity at two rotations per minute, gas flow rate of 38 ml/min CH_4 diluted by 295 ml/min steam, and temperature of 1073 K along with atmospheric outlet pressure.

4.2 Numerical Validation Case

The implemented model was validation for a rotation speed of 2 RPM, a temperature of 1073 K and an atmospheric outlet pressure. Figure 4-2 provides a

conceptual schematic of the geometry being modelled, where the red central circle is a heater that heats up the feed gases to a suitable reaction temperature (assumed to be 800°C) and the green circle is the packed catalyst bed which rotates clockwise. The reactor is divided into four sections based on the composition being fed: (1) a fuel section (combustion region) (0 to 60°); (2) two steam sections (2×30°, 60° to 90° and 330° to 360°); and (3) an air section (oxidation region) (240°, 90° to 330°). The rotating catalyst bed has an inside radius of 18 mm, a bed thickness of 12 mm, and a holder height of 60 mm filled with a 45.3 mol/m^3 capacity of copper oxide as an oxygen carrier. The external annular outlet system is divided into two exit chambers where generated gases such as CO_2, H_2O and unused feed gases can be captured. The two exit chambers are separated by rigid dividers, 2a and 2b, both of which are located in the middle of each steam sector in order to prevent internal gas mixing of the produced gases from each side, namely the combustion side (CO_2 and H_2O) and the oxidation side (N_2 and unused O_2).

In this modeling work, an operating time of 30 seconds for one rotation was applied and split over the four gas sectors, starting with the methane sector, as follows: 60°/360°*30 s = 5 s for the methane sector, 30°/360°*30 s = 2.5 s for the first steam sector, 240°/360°*30 s = 20 s for the air sector, and 30°/360°*30 s = 2.5 s for the second steam sector, respectively. Theoretically, as can be seen in Figure 4.2, particles of oxidized copper as an oxygen carrier travel over the CH_4 sector (60°) from an operating time of 0 s to 5 s, where the combustion of methane takes place. This provides energy with only CO_2 and H_2O as flue gases, which can easily be separated by condensing H_2O. The particles must be consumed and reduced by almost 100% to copper and then moved over the first steam sector (steam 1) at an operating time of 2.5 s before they reach the oxidation region (air sector), at an operating time of 7.5 s. During the air sector (240°/360°), the particles travel at an operating time of 20 s to highly adsorb and transfer oxygen from the air over the second steam sector (steam 2), taking a longer operating time of 2.5 s into the methane sector again.

As a consequence of the continuous rotation of the particles around the two sectors with the reacting gas stream (i.e., an air stream and a fuel stream), there is a transfer of oxygen from the air to the methane sector, and continuous combustion can thus be

provided over the combustion region. The two sectors with the stream of inert gas (steam) are utilized to prevent the mixing of the two reacting gases and their products (flue gases) inside the reactor. CO_2 and H_2O, as flue gases produced in the combustion region, can be captured within the area between the two steady walls, 2a and 2b, at an angle of 90°. Unused O_2 and N_2 as flue gases exiting over the oxidation region can be captured within the area between 2b and 2a at an angle of 270° and then released to the atmosphere. In this way, continuous combustion of methane with inherent separation of CO_2 from other flue gases such as N_2, H_2O and unused O_2 can be achieved using a rotating bed reactor.

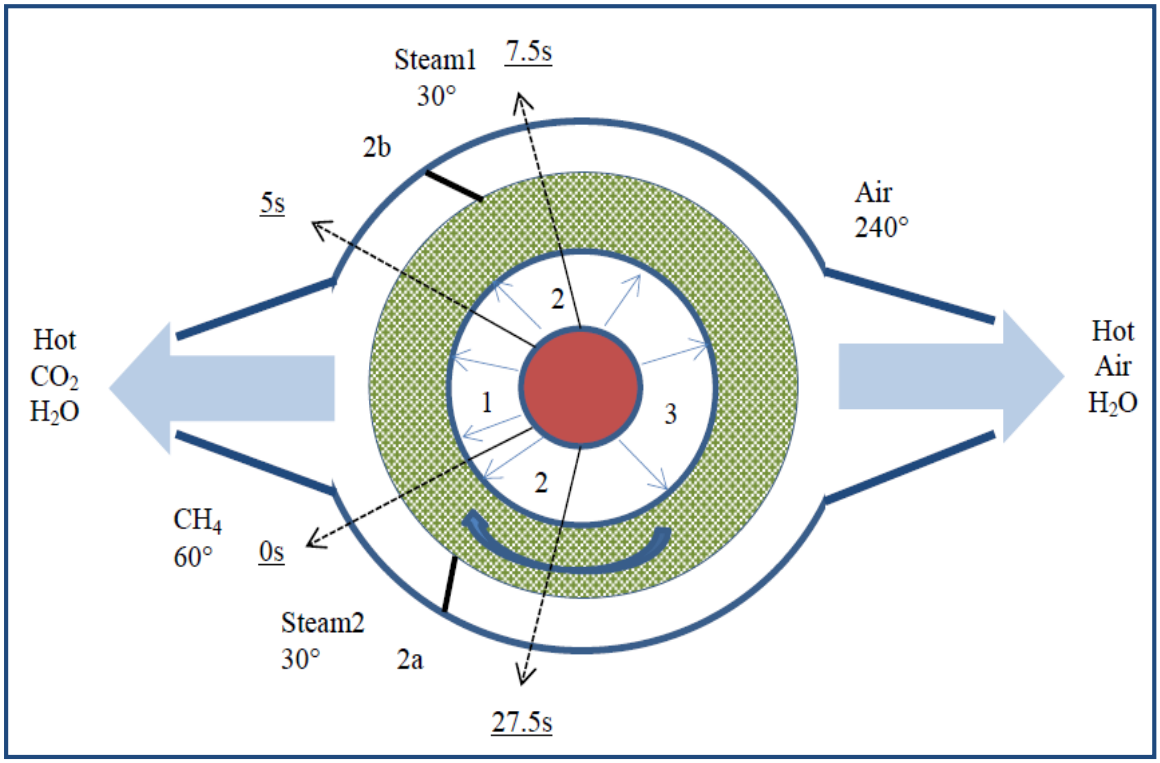

Figure 4-2 Schematic drawing of the rotating bed reactor, (Hakonsen, 2011).

For this CFD modeling work using COMSOL software, the reality of the particle movement around the four gas streams was applied as a time function for each gas flow rate over a certain area of packed bed. Figure 4-3/Figure 4-4 show a 60-second time schedule of two cycles of the inlet/outlet four gas streams flowing over a certain area of a stationary packed bed, with an initial CuO capacity of 45.3 mol/m^3. The 5 s operating time serves to flow 0.0211 mol/m^2.s CH_4 diluted by 0.1629 mol/m^2.s steam (H_2O) over the packed bed, where combustion takes place. This reduces CuO to Cu and provides

energy, using only CO_2 and H_2O as flue gases. The next 2.5 s of operating time serves to flow 0.184 mol/m^2.s steam as an inert gas to prevent mixing of the previous fed reacting gas (CH_4) and the following reacting gas (air). At a 20 s operating time, 0.184 mol/m^2.s air was fed, starting at 7.5 s and going to 27.5 s, resulting in highly adsorbed oxygen from air by copper. This can be oxidized into copper oxide as an oxygen carrier, transferring oxygen for the next cycle starting at operating time of 30 s with reacting gas of CH_4 after a 2.5 s feeding operating time of steam.

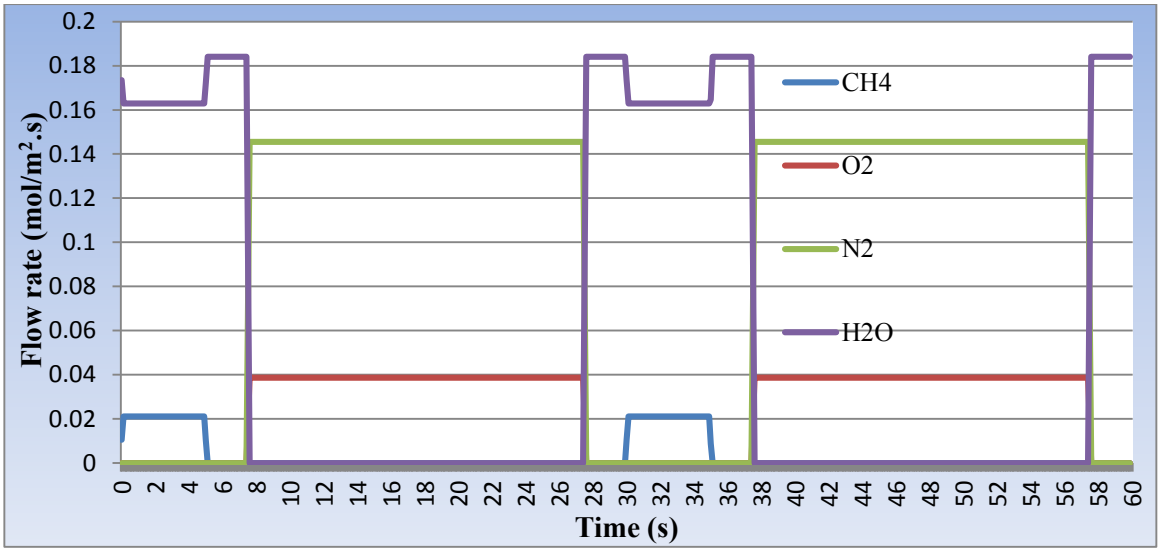

Figure 4-3 Inlet mole flow rate of each gas steam over the packed bed.

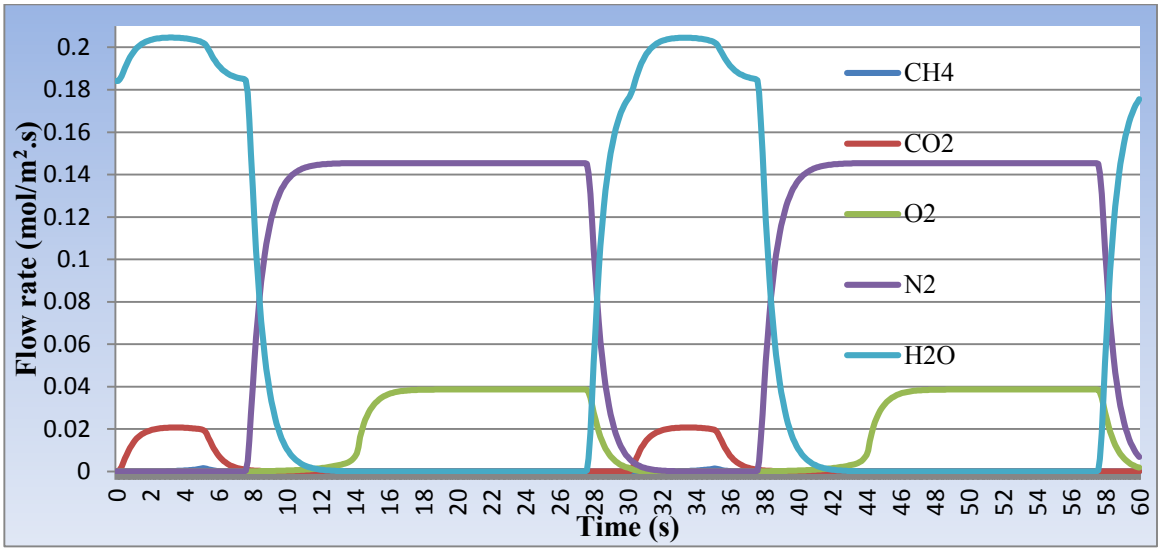

Figure 4-4 Outlet mole flow rate of each gas steam over the packed bed.

Figure 4-5 illustrates the main results of the validation case when additional parameters such as CH_4 conversion, CO_2 recovery, CO_2 purity, O_2 conversion, CH_4 crossover, CO_2 crossover, O_2 crossover, and N_2 crossover are taken into account. We calculate the CH_4 conversion by taking the integral from t = 0 to 5 s of inlet methane ($CH_{4\ in}$) minus the integral over time from 0 to 6.25 s (0 – 2b) of outlet methane ($CH_{4\ out}$). We then divided this by the integral of $CH_{4\ in}$, as shown in equation 4.1. The CO_2 recovery was given by the integral from t = 0 to 6.25 s of the outlet CO_2 in the exit chamber over the methane region ($CO_{2\ out}$ in CH_4 region), divided by the integral from t = 0 to 9 s of the total CO_2 generated by methane combustion (all $CO_{2\ out}$), as shown in equation 4.2.

Next we obtained dry CO_2 purity by dividing the integral from t = 0 to 6.25 s of the outlet CO_2 in the exit chamber (0 – 2b) over the methane region, by the sum of the integral from t = 0 to 6.25 s of all outlet gases in the exit chamber (0 – 2b) except steam (H_2O), as shown in equation 4.3. The integral from t = 7.5 to 27.5 s, of inlet O_2 ($O_{2\ in}$) within the oxidation region minus the integral from t = 6.25 to 90.3 s of all outlet O_2 (all $O_{2\ out}$), divided by the integral of $O_{2\ in}$, gives us the oxygen conversion (O_2 absorbed) over air section, as shown in equation 4.4. Equations 4.5 and 4.6 describe the crossover of

unconverted methane and generated carbon dioxide from combustion region into the exit chamber (2b – 2a) of the oxidation region, while Equations 4.7 and 4.8 define the crossover of unused oxygen and nitrogen from the oxidation region into the exit chamber (2a – 2b) of the combustion region, respectively.

$$CH_4\ Conversion = \frac{CH_{4_{in}} - CH4_{out}}{CH4_{in}} \quad 4.1$$

$$CO2\ Recovery = \frac{CO2_{out}\ in\ CH4\ Region}{All\ CO2_{out}\ (Generated)} \quad 4.2$$

$$CO2\ Purity = \frac{CO2_{out}\ in\ CH4\ Region}{(CO2_{out} + CH4_{out} + O2_{out} + N2_{out})\ in\ CH4\ Region} \quad 4.3$$

$$O2\ Conversion = \frac{O2_{in} - All\ O2_{out}}{O2_{in}} \quad 4.4$$

$$CH4\ Crossover = \frac{All\ CH4_{out} - CH4_{out}\ in\ CH4\ Region}{All\ CH4_{out}} \quad 4.5$$

$$CO2\ Crossover = \frac{All\ CO2_{out}\ (Generated) - CO2_{out}\ in\ CH4\ Region}{All\ CO2_{out}\ (Generated)} \quad 4.6$$

$$O2\ Crossover = \frac{All\ O2_{out} - O2_{out} in\ Air\ Region}{All\ O2_{out}} \quad 4.7$$

$$N2\ Crossover = \frac{All\ N2_{out} - N2_{out} in\ Air\ Region}{All\ N2_{out}} \quad 4.8$$

Since bed rotation was applied in this modeling work through time dependent boundary conditions, some discrepancies were expected between the simulated work and previous experimental data. For example, the simulated cross-over of gases from the oxidation region to the combustion region was lower in the simulated case than the experimental results. Thus, higher CO_2 recovery (99%) and higher CO_2 purity (69%) were obtained, compared to 89% and 64% in the experimental conditions. The CO_2 purity data given in Figure 4-5 indicates the amount of CO_2 present in the fuel exit gas, taking all components other than water into consideration. Since CH_4 conversion was 80%, 20% of the fed methane was unused and left the reactor either on the combustion or oxidation sides. Of the amount unused that left the reactor, 1.19% crossed over to the oxidation side and caused internal gas mixing of CH_4, unused O_2 and N_2. The high CO_2

capture efficiency of CO_2 recovery and CO_2 purity corresponded to low crossover (0.54%) of CO_2 into the oxidation region, although if the CH_4 crossing over were to assume to combust on the oxidation side, then the CO_2 recovery would reduce to 94% and be closer to the experimental system. Since a low rotation speed of 2 RPM was applied along with a large area of the oxidation region (240°), a low O_2 conversion of 24% was obtained, indicating that the oxidation region in this setup is inefficient with an excess region dedicated to this purpose. Oxygen crossover was found to be low, with 0.51% and 0.41% of fed O_2 and N_2 ending up in the methane region as free gases.

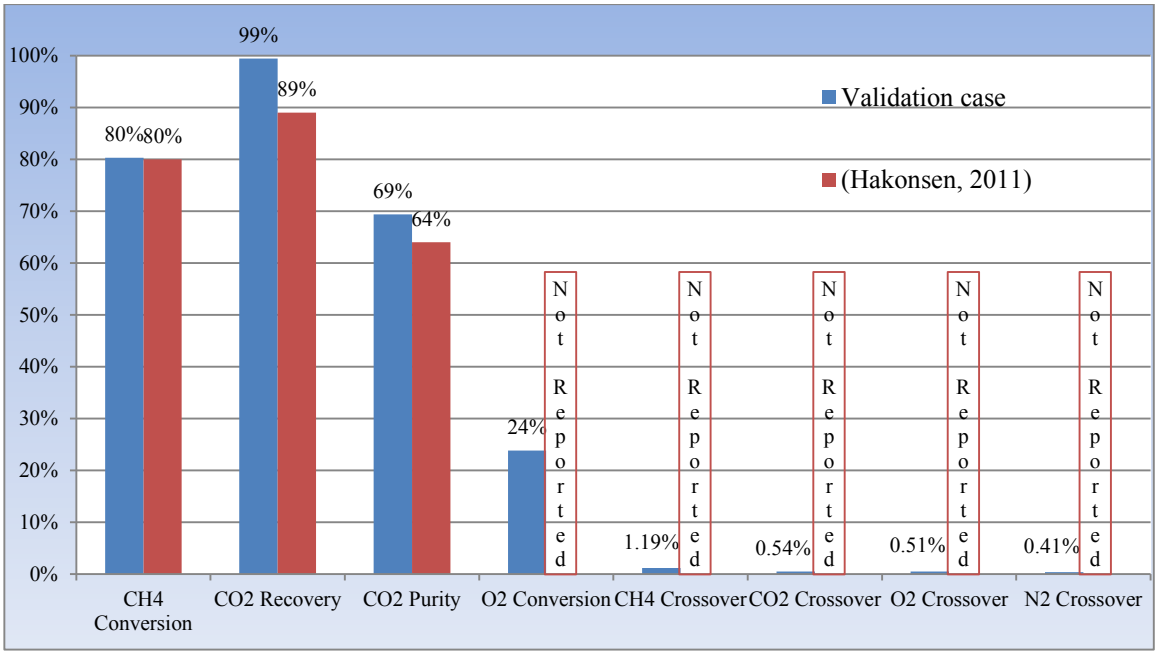

Figure 4-5 Results of the validation case and experimental results by Hakonsen (2011) at two rotations per minute.

Figure 4-6 shows several different positions of solid concentrations of CuO over the combustion region (methane sector). As illustrated in Figure 4-6, the x-axis represents the bed thickness of 12 mm as the bed length where gases flow in the x-direction; the y-axis represents the distance to a symmetrical point within the solid packing (0.75 mm) analogous to a particle radius; and the z-axis represents the concentration. At the beginning of each cycle, the rotating catalyst particles were fully oxidized due to the extended oxidation region present in the validation case. As the oxidized particles travelled through the methane region, the oxygen was rapidly depleted from the solid

particles with very little evidence of mass transfer resistance playing a significant role in combustion rate. The CuO was fully depleted by 4.7 seconds (56.4° of 60° combustion region), which is one of the significant factors which resulted in a methane conversion of only 80% (i.e. to increase methane conversion, a higher net oxygen flow rate needs to enter the combustion region through rotation of the bed). Therefore, a higher bed rotating speed is recommended for greater oxygen capacity over the combustion region to obtain higher methane conversion. It is worthwhile noting that some over-shoots in concentration were observed during the simulations, where even with fairly strict time discretization and dampening factors a slight over-consumption of CuO was predicted. This primarily occurred right at the inlet with a negligible net effect on oxygen capacity in the context of a parametric study

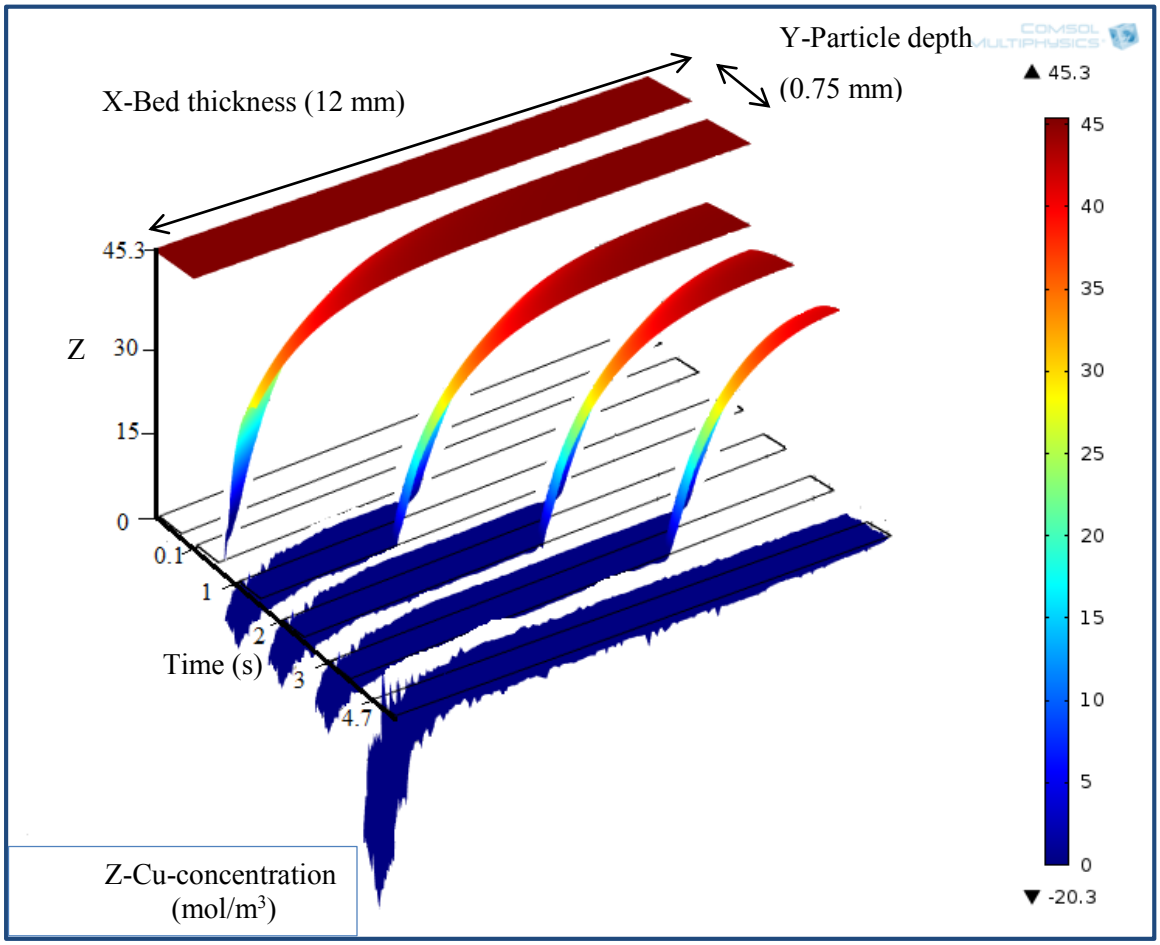

Figure 4-6 Solid concentration of CuO within the combustion side for operating time (t) = 0, 0.1, 1, 2, 3 and 4.7 seconds after entering the combustion region for the validation case at two rotations per minute.

In Figure 4-7, on the other side of the reactor (oxidation region), six varied positions of Cu concentration over the air sector are shown. When the reduced Cu first enters the oxidation region (7.5 s), the surface concentration of Cu decreased dramatically with the introduction of a fresh feed of air. Within only 4.5 seconds of entering the oxygenation region (of a total 20 seconds region time), almost 95% of the Cu capacity was oxidized to CuO. As a result, only 22.5% of the area (4.5 s/20 s operating time) of the oxidation region was used to convert most of the Cu to CuO, while more than 75% represents inefficient operation. As more than 75% of the oxygen flowing over the bed in the oxidation side was not adsorbed, reducing the net energy efficiency, a smaller area of air sector (oxidation region) is expected to increase overall performance.

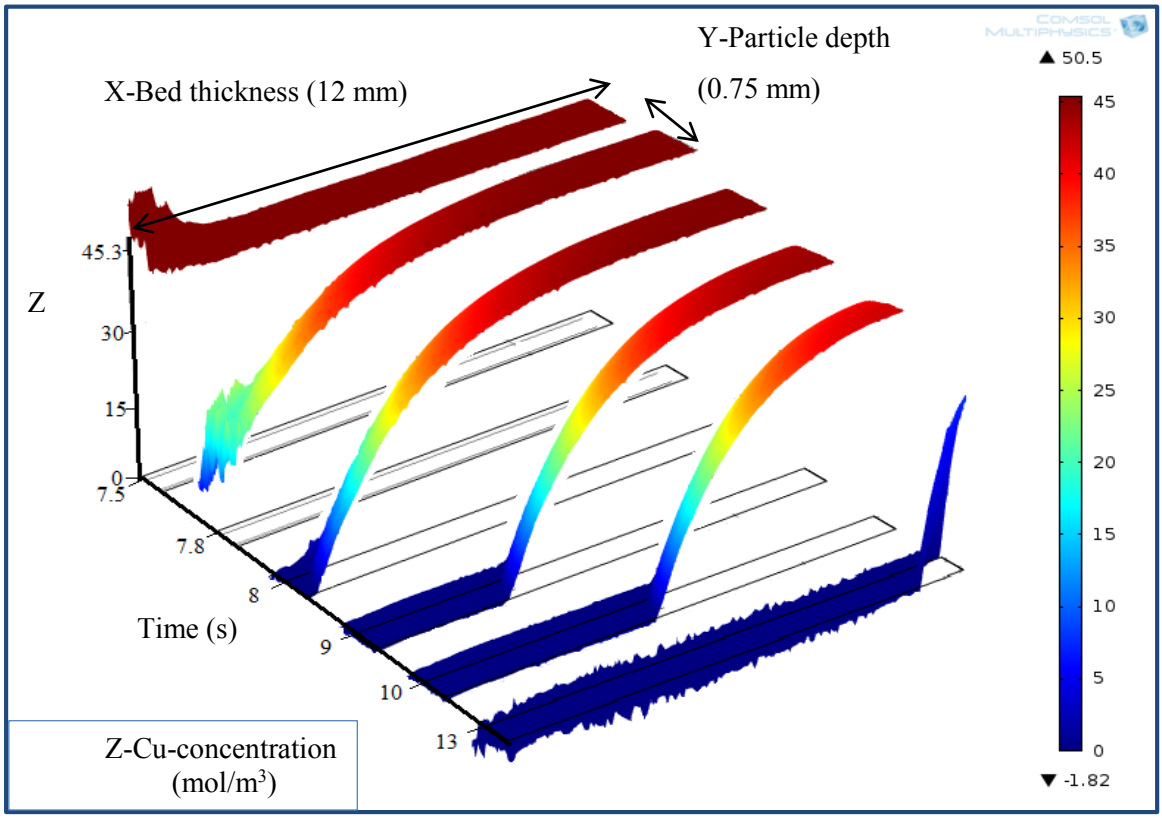

Figure 4-7 Solid concentration of Cu within the oxidation side for time (t) = 7.5, 7.8, 8, 9, 10, 13 seconds after entering the oxidation region for the validation case at two rotations per minute.

In this work, the following parameters are focused on and compared to different simulation cases to obtain optimal results. Varied changes in operating conditions and reactor designs, such as reactor rotation frequency, bed thickness and gas flow regions,

are investigated to ascertain maximum and optimal fuel (CH_4) conversion, CO_2 capture efficiency, and energy efficiency.

4.3 Mesh Convergence Study

An edge mesh for the first domain and a mapped mesh for the second domain were used for better control of the elements shape and size. A convergence study was performed in order to determine the optimum number of elements needed to maintain the highest level of accuracy and minimize simulation time. Simulation with different distribution of elements within edge and mapped meshed were performed. As mentioned in section 0, 120 as the number of elements for the interval geometry of the first domain and 50 elements at the 0.00075 m height along with 120 elements at the 0.012 m width of rectangle geometry for the second domain were set for the first run of a numerical validation case. Lower number of elements of 60 for the interval geometry (see Figure 4-8) and 25 elements at the height along with 60 elements at the width of the rectangle geometry (see Figure 4-9) were set to investigate the effect of different elements distribution over the geometries.

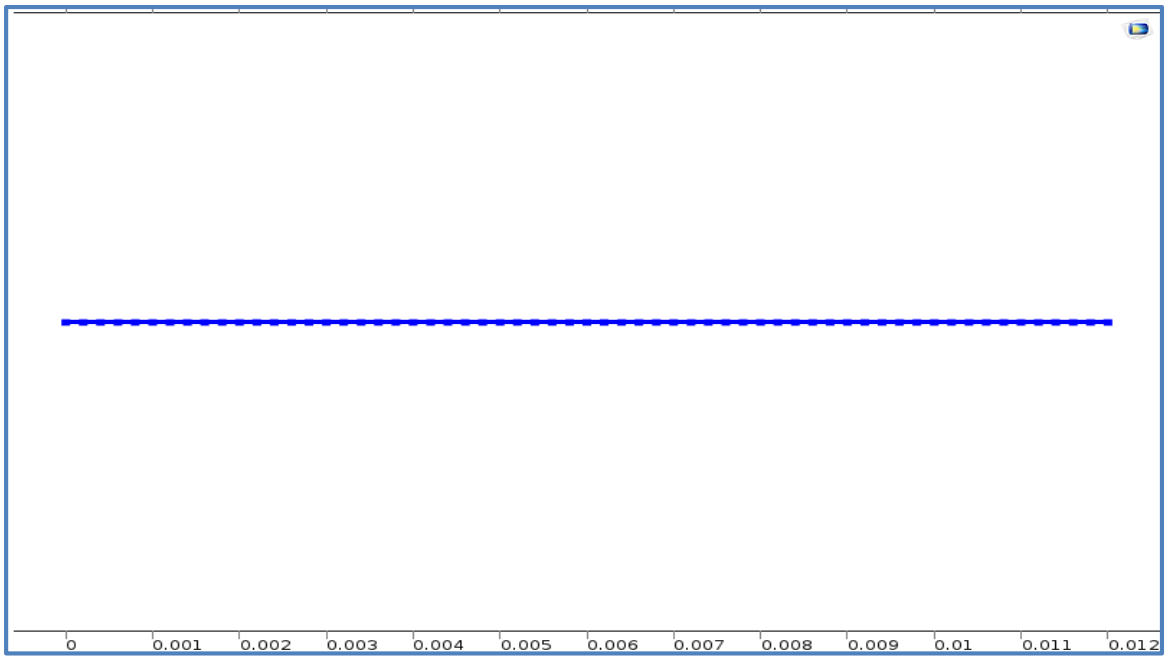

Figure 4-8 Elements distribution of geometry 1 representing the flow channel for the first domain in the model.

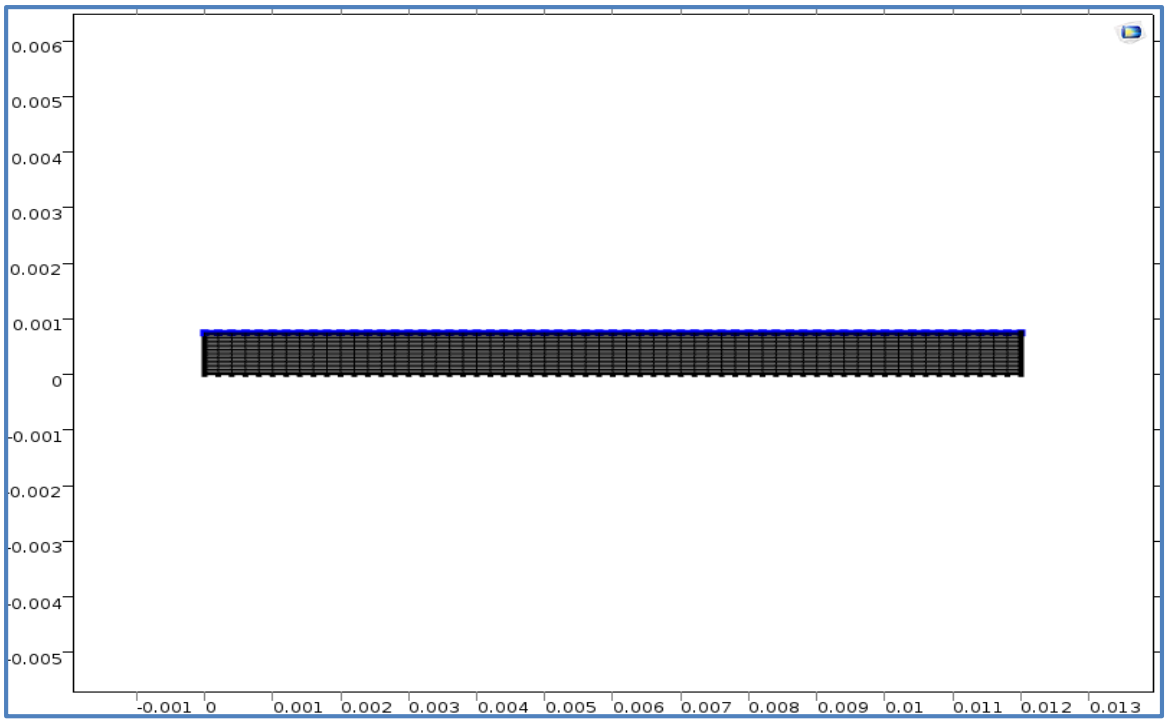

Figure 4-9 Elements distribution of geometry 2 representing the flat porous bed for the second domain the model.

The exact results (see Figure 4-5) of methane conversion, CO_2 recovery, CO_2 purity, oxygen conversion and gas crossover of the numerical validation case were obtained with a simulation having lower elements distribution over the two geometries (see Figure 4-8Figure 4-9) and same running time. Thus, there is no effect on results of applying different amount of elements over both geometries. High amount of elements similar to the numerical validation case was applied with all cases simulated in this study for higher resolution.

4.4 Reactor Rotation Frequency

Two modeling runs were carried out to analyze reactor performance using different reactor rotation frequencies. Variations in the reactor rotation speed between 1 and 4 rotations/min led to moderate changes in reactor performance (Figure 4-10). Since a higher bed rotating speed results in greater oxygen capacity transferred by CuO over the combustion region, CH_4 conversion varied between 38% and 99%, with the lowest conversion obtained at a rotation speed of 1 min^{-1} and the highest at 4 min^{-1}. Therefore, a

higher rotation speed shows promise for higher fuel conversion (i.e., higher energy generated within combustion region). Because a lower conversion of CH_4 produces a lower amount of CO_2, which can easily be captured within combustion region, the highest CO_2 recoveries (up to 100%) were obtained at 1 and 2 rotations/min.

Since CO_2 purity depends on the sum of all outlet gases (CO_2, CH_4, O_2 and N_2) within the combustion region (2a – 2b), CO_2 purity was dropped to 39% and 50% with rotation speeds of 1 min^{-1} and 4 min^{-1}, respectively. The consequence was high (almost 62%) unconverted outlet methane in the combustion region at 1 RPM and high crossover of O_2 and N_2 from the oxidation region into the combustion region at 4 RPM. Therefore, the highest unwanted CO_2 crossover was obtained at rotation speeds of 4 min^{-1}. Furthermore, an 80% conversion of CH_4 with almost 90% of CO_2 recovery efficiency and the highest CO_2 purity efficiency along with very low CO_2, O_2 and N_2 crossover were acquired at a rotation speed of 2 min^{-1}, which is thus considered to be optimal for CO_2 capture efficiency among the three rotation speeds (1, 2 and 4 min^{-1}) for the setup at these conditions and designs. However, two additional rotation speeds (2 and 4 min^{-1}) were investigated and analyzed with different geometry designs, such as bed thickness and flow region area, to maximize the fuel conversion along with CO_2 capture efficiency.

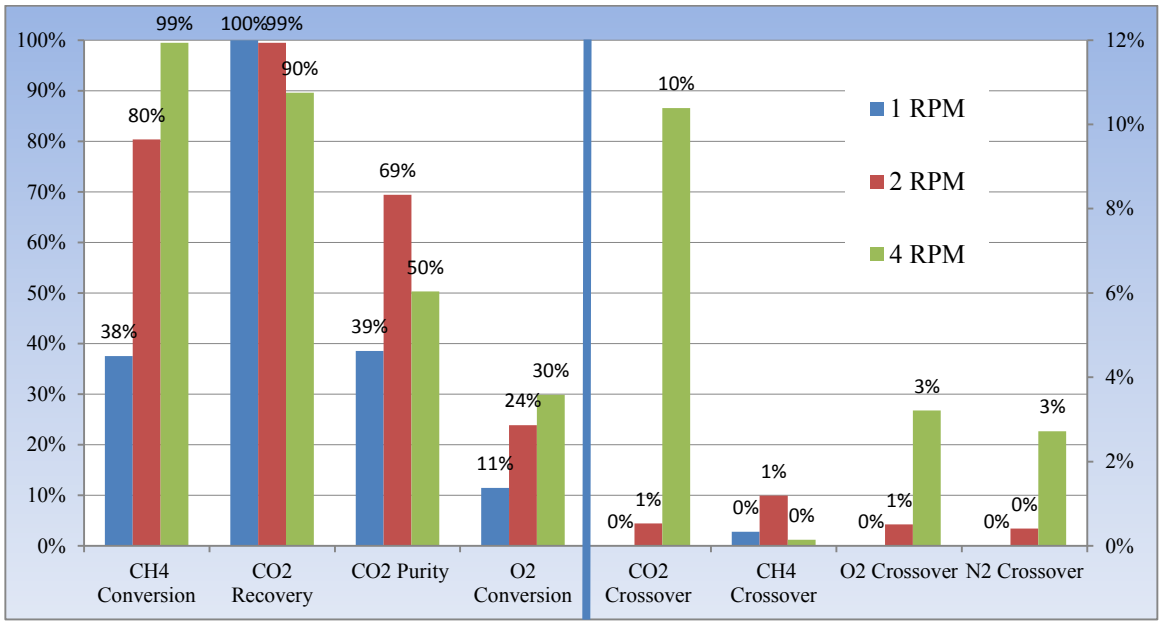

Figure 4-10 Effect of change in reactor rotation speed of three modeling runs using three different rotating frequencies, 1 min^{-1}, 2 min^{-1} and 4 min^{-1}.

4.5 EFFECT OF CHANGE IN ROTATING BED THICKNESS

Two different bed thickness values of 10 mm and 14 mm and two rotation speeds of 2 min^{-1} and 4 min^{-1} were chosen to investigate the impact of rotating bed thickness on operating parameters. As illustrated in Figure 4-11, the widest bed thickness (14 mm) gave the highest CH_4 conversion for both rotation speeds, primarily due to the increased oxygen content relative to the other bed thicknesses at each RPM. With rotation frequencies of 2 RPM, a higher bed thickness (higher oxygen content) increases CH_4 conversion from 59% to 97%, and therefore higher values of CO_2 recovery and purity are expected.

However, the reverse results were obtained with a rotation speed of 4 RPM, where higher values of bed thickness gave lower CO_2 recovery and CO_2 purity at almost same CH_4 conversion. From this it can be concluded that higher thickness gives more chance of gas leakage between stream sectors. As a result, a higher unwanted crossover of CO_2, O_2, N_2 and CH_4 occurred with higher bed thicknesses for both 2 and 4 rotations per minute, and a greater likelihood of internal gas mixing over the bed was given by higher (14 mm) bed thickness. Because of this, wider bed thickness is recommended to be applied with any rotation frequencies for higher fuel conversion, but not for avoiding internal gas mixing.

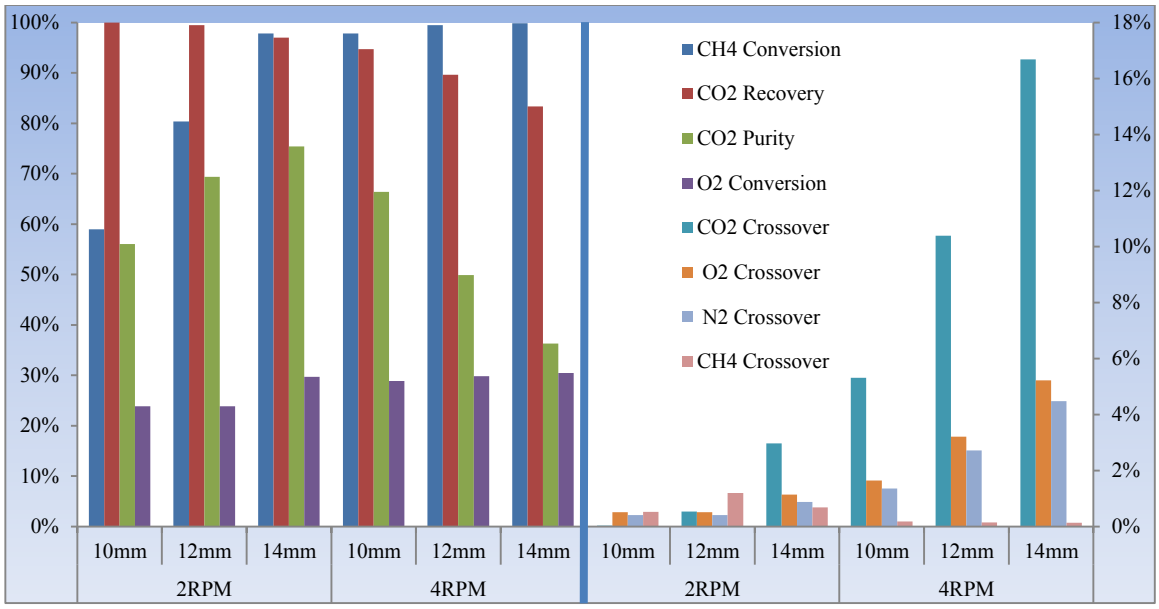

Figure 4-11 Effect of change in rotating bed thickness of six modeling runs using three different values of bed thickness (10, 12 and 14 mm) along with two rotation speeds of 2 min^{-1} and 4 min^{-1}.

4.6 FLOW REGION AREA WITH DIFFERENT ROTATION FREQUENCIES OF REACTOR

Five cases of the modeling run with different geometry designs along with varied rotation speeds of 2 RPM and 4 RPM were simulated and investigated to analyze the effect of changes in the flow region area. A brief description of each case with geometry design and rotation speed is provided in Table 4-1. As mentioned in section 4.2, a low rotation speed of 2 RPM along with a large area of the oxidation region (240°) was applied with the validation case, which resulted in low O_2 conversion of 24%, (see Figure 4-5). Therefore, cases 1 and 2 were designed in attempt to reduce the inefficient area of the oxidation region and increase the combustion region to a 2:1 ratio since it takes 2 moles of O_2 to burn 1 mole of CH_4. Rotation speed of 4 RPM was applied with case 2 to increase oxygen capacity over the combustion region for higher methane conversion. Increasing the steam region ratio to triple area of the validation case was applied with case 3 in order to avoid any gas crossover through the bed. It worked well and resulted in zero crossover, but high amount of steam means high energy expenditure, especially with small area (60°) of the combustion region (low energy production). As a consequence, the amount of purge (steam region) was reduced with case 4 to the double of the

validation case for saving steam energy and increasing the area of the combustion region (increasing energy production). Since there was minimal crossover with case 4 at 2 RPM, case 5 was performed with same geometry of case 4 but higher rotation speed of 4 RPM for higher methane conversion.

Table 4-1 Six different geometric designs of flow region area along with varied rotation

Case	Combustion	Steam Purge (x2)	Oxidation	RPM
Validation	60°	30°	240°	2
1	100°	30°	200°	2
2	100°	30°	200°	4
3	60°	90°	120°	2
4	80°	60°	160°	2
5	80°	60°	160°	4

Figure 4-12 illustrates the significant results from the five cases. In case 1, slow movement (2 RPM) of the rotating bed with a large combustion region of 100° gave the lowest values of CH_4 conversion (48%) and CO_2 purity (47%) along with the highest CO_2 recovery (100%) caused by low CO_2 production captured within the large combustion region. In addition, the highest undesirable crossover of O_2, N_2 and CH_4 were also given by case 1. Case 2 had the same geometry design as case 1 but higher rotation frequencies of 4 RPM (i.e., a higher oxygen capacity within the combustion region). This resulted in high CH_4 conversion (95%) and high CO_2 recovery (93%) but relatively low CO_2 purity (58%) caused by high crossover of O_2 and N_2 from the oxidation region into the combustion region.

Case 3 had a similar rotation speed and area of combustion region as the validation case, resulting in the same CH_4 conversion (80%) and CO_2 recovery (100%). However, a larger steam region of 90° gave the benefit of a higher capture and purity of CO_2 and zero crossover for CO_2, O_2, N_2 and CH_4 and gave the disadvantage of using higher steam flow rate (i.e., more energy required for steam generation). In case 4, the low oxygen capacity was transferred by the rotation speed of 2 RPM over a large combustion region of 80°, resulting in a low CH_4 conversion of 60% and a low CO_2 purity of 60%. Therefore, the geometry of case 4 is not recommended to be applied with the rotation speed of 2RPM. The highest CH_4 of 98%, along with high efficiencies of CO_2 recovery (97%) and CO_2

purity (78%) as well as very low values (0%, 1.2%, 2.5% and 2.8%) of crossover for CH_4, N_2, CO_2 and O_2, respectively, were achieved with case 5, which has the same geometry as case 4 but applied with a rotation speed of 4 RPM (i.e., more oxygen capacity transferred over the combustion region for higher fuel conversion). Therefore, optimal results for the setup at these conditions were attained with cases 3 and 5, both of which demonstrated high conversion, high efficiencies of CO_2 recovery and CO_2 purity, and very low crossover.

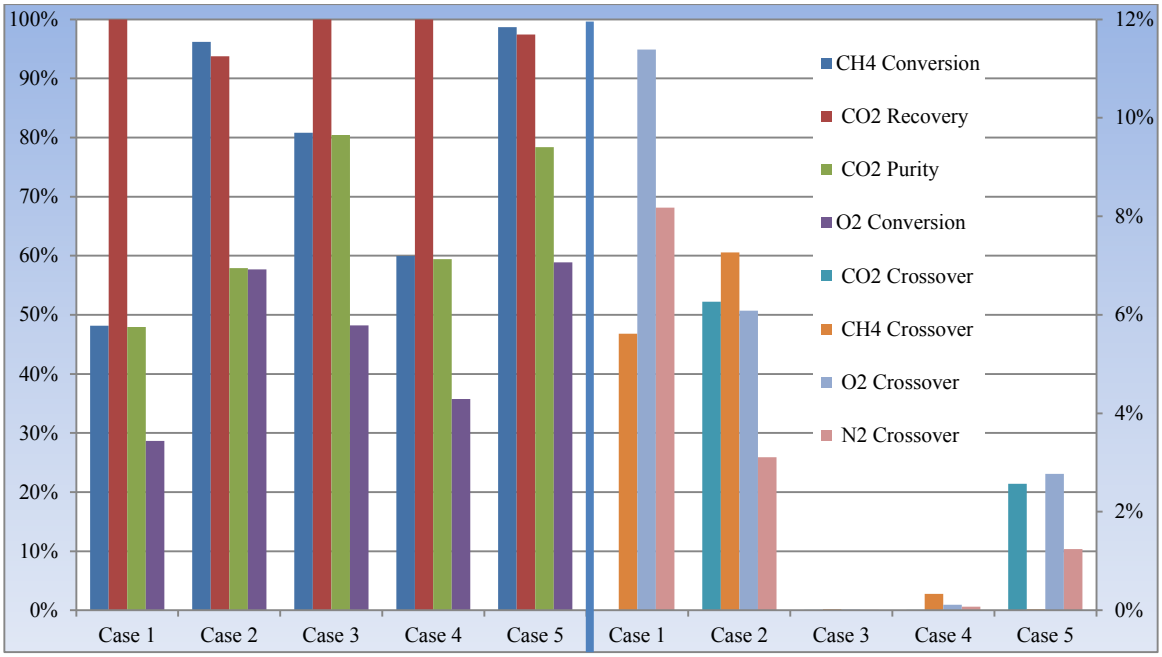

Figure 4-12 Effect of change in flow region area of five modeling runs having different region areas and bed rotation frequencies.

4.7 COMPARISON AND ANALYSIS OF THE THREE OPTIMAL CASES OF THE SETUP

A detailed comparison between the validation case and the two optimal cases that gave the best results took into account the most economical simulation with the highest energy supply. As shown in Figure 4-13, case 3 gave almost the same fuel conversion (same energy supply) and CO_2 recovery efficiency as the validation case. However, 10% less CO_2 purity efficiency was obtained with case 3. Furthermore, a large steam section (90°) in case 3 resulted in zero values of CH_4, CO_2, O_2 and N_2 crossover compared to very low values of crossover obtained in the validation case. As mentioned in Table 4-1, the geometry of case 3 shows a steam section with a triple-sized steam section in the

validation case; therefore, a triple amount of steam (i.e., triple the energy of the steam supply) is required. The setup of case 3 resulted in a lower energy supply when the energy of the steam supply was taken into account.

The highest fuel conversion (99%) along with relatively high CO_2 recovery efficiency (99%) and CO_2 purity efficiency (78%) were achieved in case 5. The geometry of case 5 has a steam section double the size (and thus double the energy of steam supply) of the validation case, as mentioned in Table 4-1. Compared to the validation case, a 19% higher fuel conversion (more energy supply and more water production) and slightly higher values of CO_2, O_2 and N_2 crossover were achieved in case 5, whose high fuel conversion (99%) resulted in zero crossover of CH_4. Therefore, optimal results for the setup at these conditions were attained with case 5, which demonstrated higher conversion, higher efficiencies of CO_2 recovery and CO_2 purity, and very low crossover.

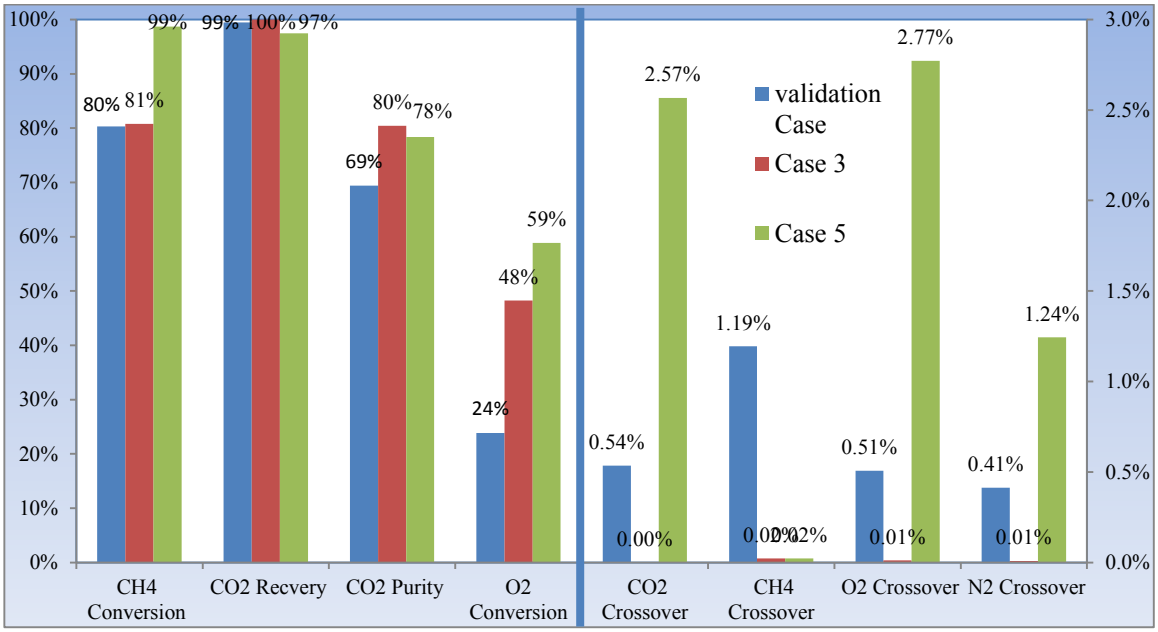

Figure 4-13 Results of setup's three optimal cases taking into account rotation speed and flow region area.

Figure 4-14 shows six different positions of CuO concentration over combustion regions for case 5. Compared to the validation case (Figure 4-6), a larger area (80°) of the combustion region and a higher rotation speed of 4 rotation/minute were applied to case 5, which resulted in a higher net oxygen flow rate entering the combustion region.

Consequently, a 99% fuel conversion was obtained by only 80% consumption of oxygen capacity passed by particles over the combustion region at operating time of 3.3 seconds (80° of 80° combustion region). Therefore, a higher rotation speed shows promise for transferring higher oxygen capacity from the oxidation region into the combustion region, which ultimately leads to higher fuel conversion (higher energy supply) even with higher fuel flow rate (case 5) compared to the validation case.

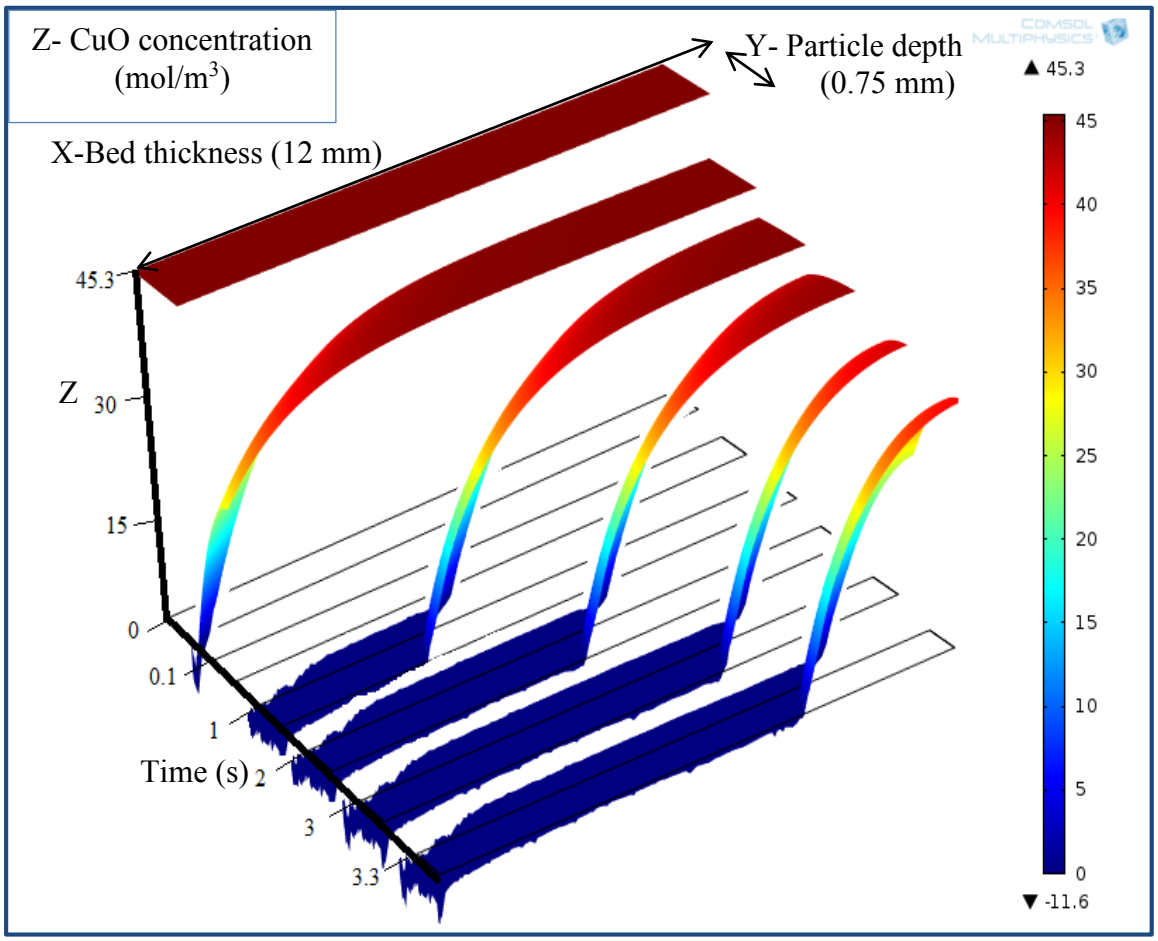

Figure 4-14 CuO concentration over combustion region for case 5.

Since almost 95% of the Cu capacity was oxidized to CuO within only 4.5 seconds of entering the oxygenation region (of a total 20 seconds region time) with the validation case (Figure 4-7), a smaller area (160°) of the oxygenation region was used with case 5 in attempt to decrease the net oxygen flow rate and increase the net energy efficiency. Cu concentration profile of six different positions over the oxygenation region for case 5 is presented in Figure 4-15. Within only 4.2 seconds of entering the oxygenation region (of

a total 6.6667 seconds region time), almost 95% of the Cu capacity was oxidized to CuO. As a result, more than 62% area (4.2 s/6.67 s operating time) of the oxygenation region was used to convert most of the Cu to CuO. Therefore, low inefficient operation over the oxygenation region of 37% was obtained with case 5 compared to 75% inefficient operation with the validation case. It can be concluded that a smaller area of air sector shows promise for higher overall performance.

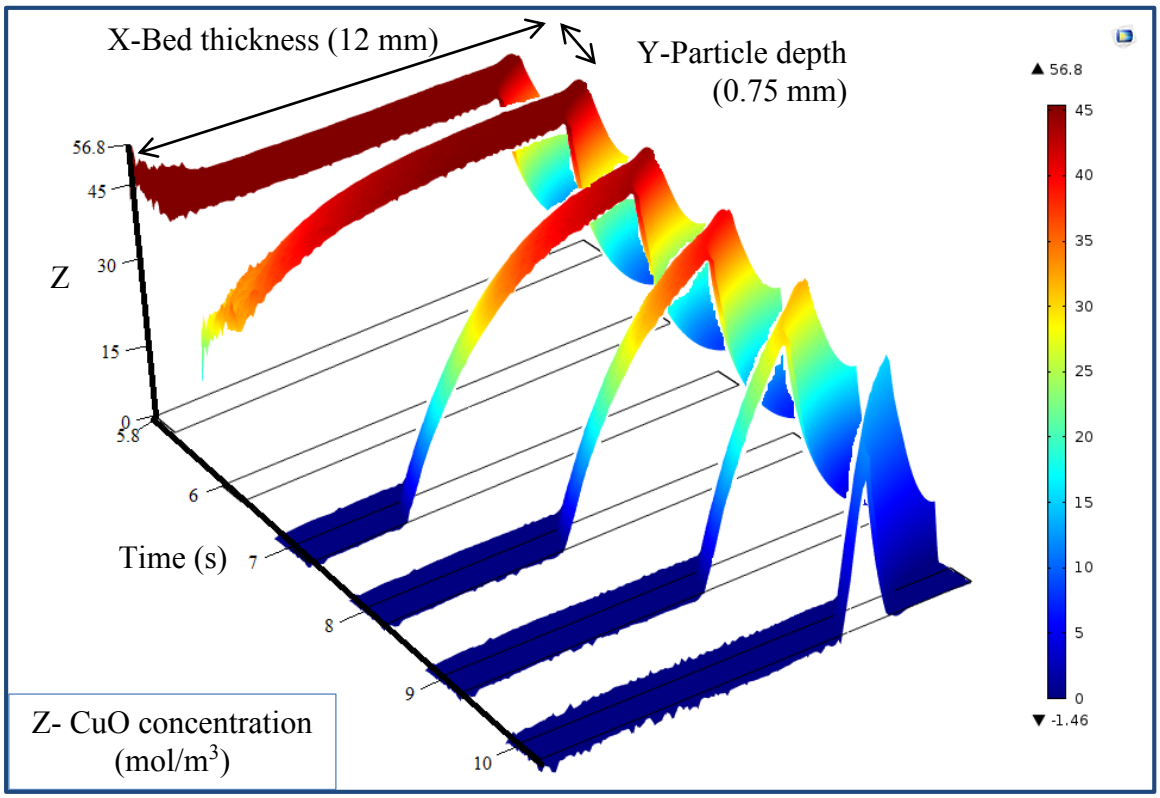

Figure 4-15 Cu concentration over oxidation region for case 5.

4.8 Analysis of Result

In order to allow for the CFD results to be extended beyond the limited cases actually simulated, scaling analysis was performed on the different regions of the reactor in an attempt to gain a better understanding of how the performance itself relates to operating conditions and design of individual regions.

Focusing first on the methane region, all of the simulations collapsed onto a similar curve when scaled by $(t/t_{bed})^{1.5}$, where t is the time since entering the region and t_{bed} is the

average residence time in the bed (i.e. bed thickness / gas velocity). The resulting characteristic curves are shown in Figure 4-16. Since a high rotation speed along with high values of bed thickness transfer high oxygen capacity by particles moving from an oxidation region into a combustion region, only 60-75% oxygen capacity was consumed in cases having the same design as the validation case but a higher rotation speed of 4 RPM and bed thicknesses of 14 and 12 mm (see Figure 4-16). Therefore, as shown in Figure 4-11, very high fuel conversion of up to 99% was obtained with these cases, whereas high unwanted CO_2 crossover achieved 10 and 17%, respectively. Furthermore, 90% of oxygen capacity was consumed to achieve over 95% fuel conversion and less than 5% CO_2 crossover with two cases (see Figure 4-11 and Figure 4-13) sharing the same rotation speed of 4 RPM, having different bed thickness of 10 and 12 mm and different fuel design sections of 60° and 80°. As illustrated in Figure 4-16, almost 100% of oxygen capacity was consumed (i.e., a fully reduced oxygen carrier over a combustion region) in most of the other cases before high fuel conversion could be obtained (see Figure 4-10, Figure 4-11, Figure 4-12 and Figure 4-13). It can be concluded from this that higher rotation speed is promising for transferring higher oxygen capacity over a combustion region. Therefore, higher fuel conversion is expected, taking into account higher unwanted CO_2 crossover in some cases. It should be noted that the horizontal sections in Figure 4-16 represent are primarily for operating conditions where due to high rotation rates there was insufficient time to use the full bed capacity or full oxygenate the solids.

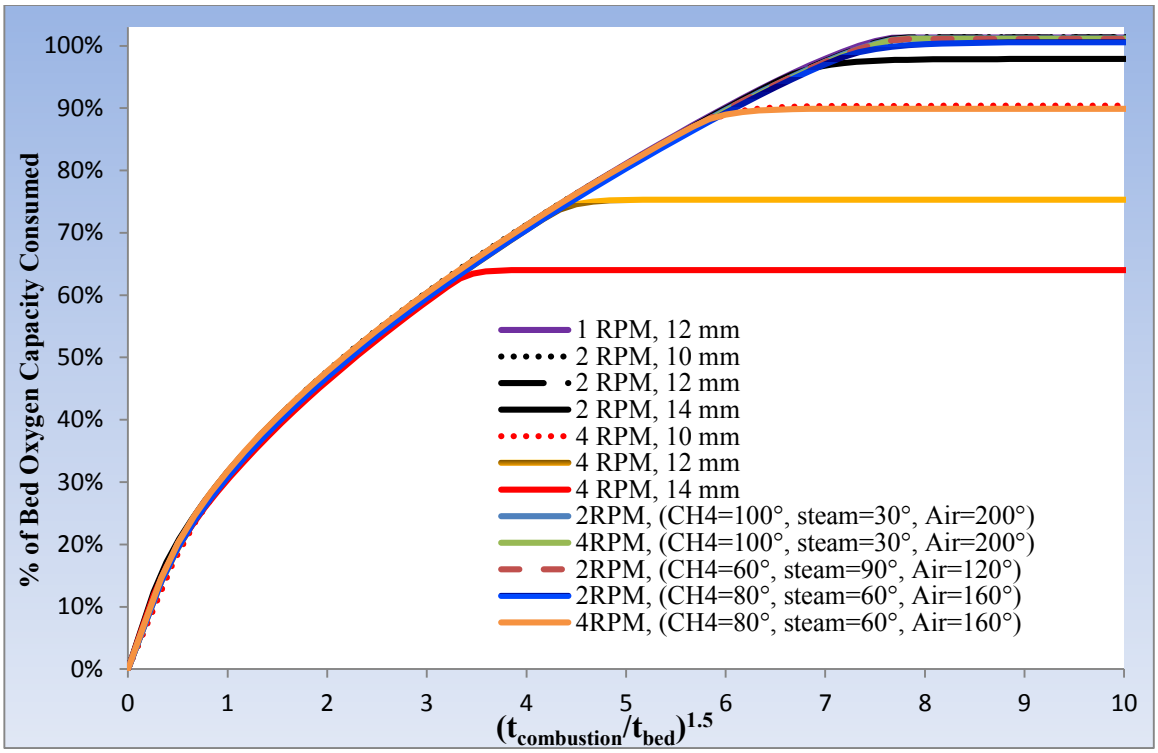

Figure 4-16 The percentage of bed oxygen capacity consumed over the combustion region of twelve modeling runs with different bed thicknesses and gas section areas. The first seven cases have the same gas sections area as the validation case, and the last five cases have the same bed thickness as the validation case.

Figure 4-17 presents the average of CH_4 concentration (mol/m^3) within the bed vs dimensionless operating time over bed time, with a scaling power of 1.5. The average amount of CH_4 concentration within the bed depends mainly on the percent of conversion (combustion) of CH_4 into CO_2 and H_2O, which is based on the amount of oxygen capacity being transferred into the combustion region. Thus, the average amount of CH_4 concentration in Figure 4-17 follows the oxygen capacity presented in Figure 4-16, where a high oxygen capacity over the combustion region resulted in high CH_4 conversion, while low oxygen capacity over the bed led to low CH_4 conversion. For example, the lowest average CH_4 concentration left within the bed was acquired by cases having the highest oxygen capacity per unit volume vs. time caused by high rotation speed of 4 RPM and a large bed thickness of 14 mm, whereas the highest average of CH_4 concentration left over the bed was given by cases with low rotation speeds of 1 and 2 RPM and small bed thicknesses of 10 and 12 mm (see Figure 4-10, Figure 4-11, Figure 4-12 and Figure

4-13). Of particular note is that for dimensionless operating time above 7, the methane concentration increased at a higher rate as the remaining oxygen capacity becomes low. Optimal use of O_2 capacity is thus expected to occur for operating time near this value, which should also limit CH_4 cross-over by keeping the concentration within the bed low.

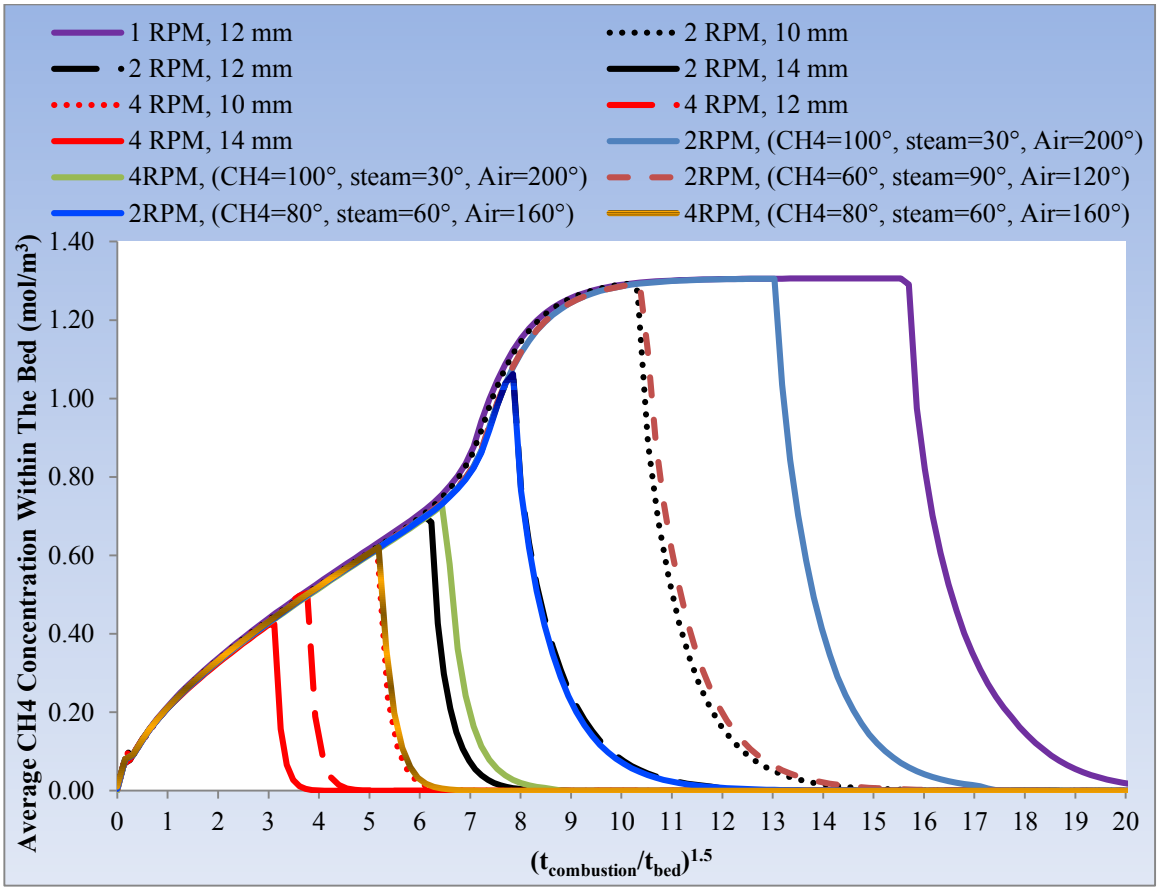

Figure 4-17 Average CH_4 concentrations within the bed (mol/m^3) of twelve modeling runs with different bed thicknesses and gas section areas. The first seven cases have the same gas sections area as the validation case, and the last five cases have the same bed thickness as the validation case.

Figure 4-18 provides the concentration reduction curve within the purge region following the CH_4 region, scaled on a similar basis. The average unconverted CH_4 concentration (mol/m^3) entering the same region has a significant effect on the time required to purge the CH_4 levels to a point which limits crossover, with most cases where O_2 capacity was completely consumed having the highest unconverted average of CH_4 caused by low rotation speed and low oxygen capacity over the bed, such as 1 RPM, 12 mm, 2 RPM, 10 mm, etc.

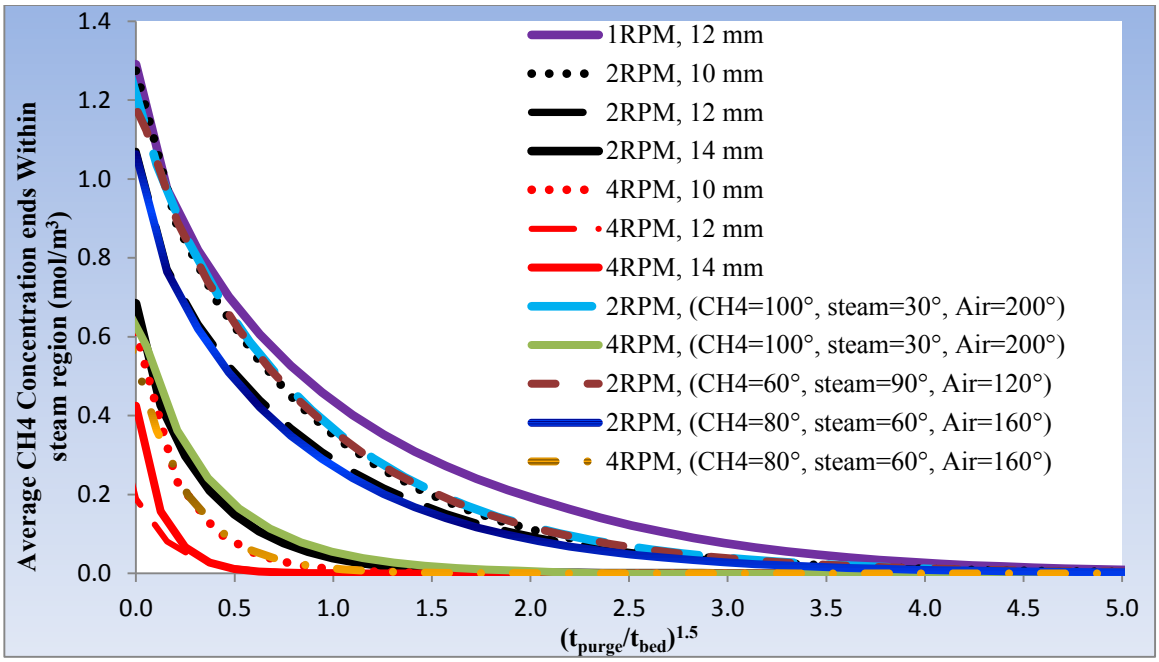

Figure 4-18 Average CH_4 concentration ends within the steam region (mol/m^3) of twelve modeling runs with different bed thicknesses and gas section areas. The first seven cases have the same gas sections area as the validation case, and the last five cases have the same bed thickness as the validation case.

Figure 4-19 shows the average of CO_2 concentration (mol/m^3) within the bed, also scaled by $(t/t_{bed})^{1.5}$. The concentration depends on the percentage of methane converted into CO_2 and H_2O by oxygen capacity transferred into the combustion region. Initially increasing but dropping off as CO_2 generation drops. After the oxygen capacity is consumed, the CO_2 concentration profile follows a similar trend as observed within the purge region, whereby the combustion gases are simply displacing any CO_2 remaining in the bed. Therefore, the average of CO_2 concentration in Figure 4-19 follows the percent of bed oxygen capacity consumed over the combustion region (see Figure 4-16). As the highest oxygen capacity has been transferred over the combustion region by cases having a high rotation speed of 4 RPM and higher bed thicknesses of 14 and 12 mm, the CO_2 concentration was generated with a high values at the end of the combustion region, when operating time and bed volume were taken into account. Therefore, high unwanted CO_2 crossover from the combustion region into the oxidation region was detected with these cases (see Figure 4-11). With the low oxygen capacity being transferred over the combustion region (lower methane conversion), lower values of CO_2 concentration were

obtained even before the end of the combustion region (Figure 4-19). A higher oxygen capacity over the combustion region is caused by a higher rotation speed, which is required for higher fuel conversion, taking into consideration low values of CH_4 and CO_2 crossover.

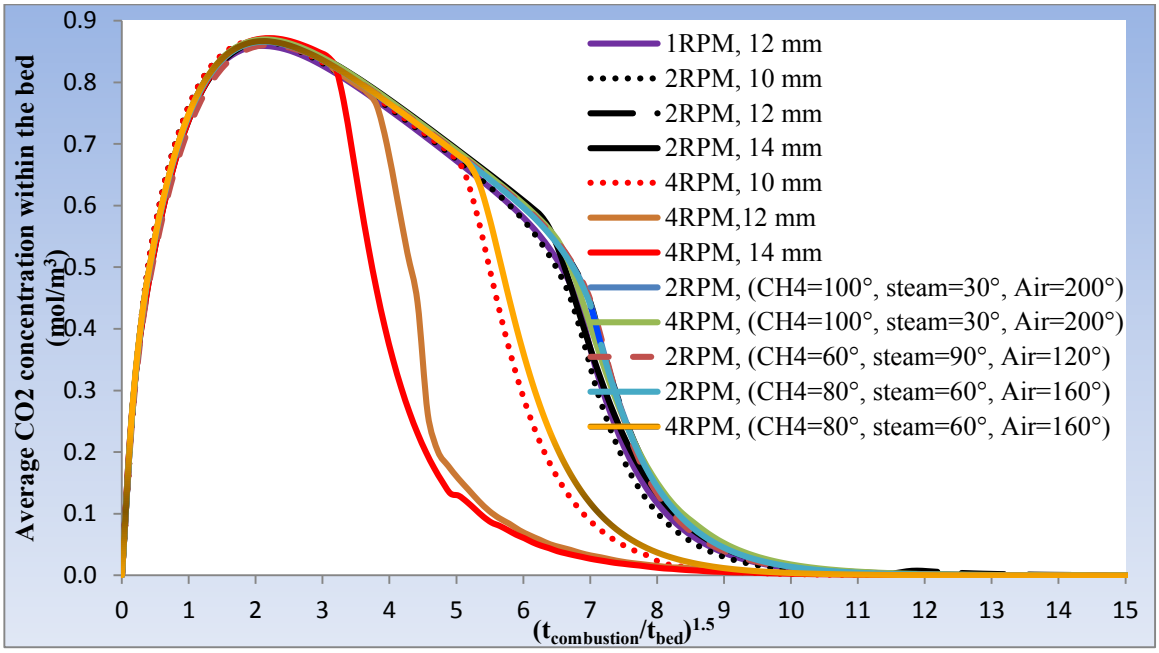

Figure 4-19 Average CO_2 concentration within the bed (mol/m^3) of twelve modeling runs with different bed thicknesses and gas section area. The first seven cases have the same gas sections area as the validation case, and the last five cases have the same bed thickness as the validation case.

The lowest CO_2 crossover from the combustion region into the steam region was obtained with cases such as 1 RPM, 12 mm, 2 RPM 10 mm and case 2 (see Figure 4-10, Figure 4-11 and Figure 4-12). Here, low CH_4 conversion was caused by low rotation speeds along with low values of bed thickness and low oxygen capacity over the combustion region. The highest CO_2 crossovers into the steam region (see Figure 4-20) and then to the oxidation region (see Figure 4-11 and Figure 4-12) were given by cases having the highest rotation speed and highest bed thickness, such as 4 RPM, 14 mm, 4 RPM, 12 and case 2. In order to achieve high fuel conversion and avoid high CO_2 crossover into an oxidation region, a high rotation speed of 4 RPM along with a larger steam region area (60°) was suggested (case 5), which resulted in a high methane conversion of 98.7% with lower CO_2 crossover of 2.5% (see Figure 4-12). This is and

considered to be optimal for the setup at these conditions. Therefore, to reach high fuel conversion with 0% of CO_2 and/or CH_4 crossover from the combustion region into the oxidation region, minimum dimensionless operating time greater than 2 to 3 should be used before the rigid panel separating the combustion and oxidation regions to ensure that most of the CO_2 remaining within the bed is purged.

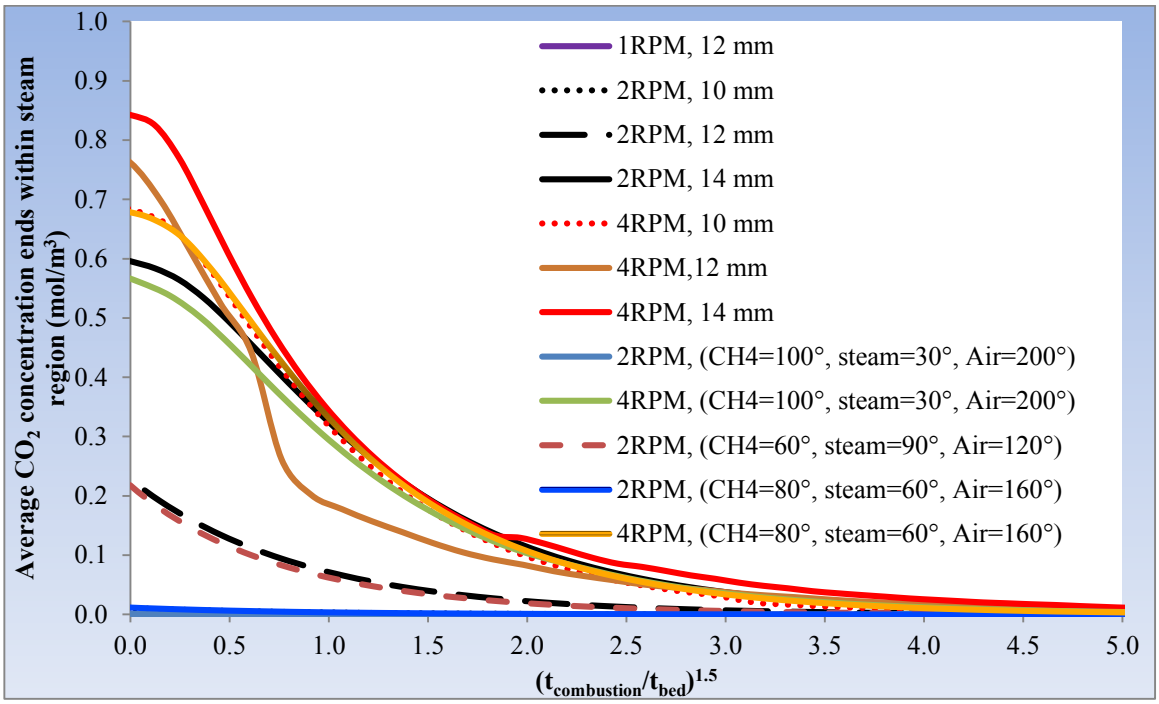

Figure 4-20 Average CO^2 concentration ends within the steam region (mol/m^3) of twelve modeling runs with different bed thicknesses and gas section area. The first seven cases have the same gas sections area as the validation case, and the last five cases have the same bed thickness as the validation case.

Because the percentage of conversion of Cu capacity into CuO over the oxidation region based on how much CuO is reduced to Cu over the combustion region, Figure 4-21 followed exactly the percentage of oxygen capacity consumed by reducing CuO over the combustion region presented by Figure 4-16. As illustrated in Figure 4-21, the percentage of CuO reduced into Cu in all cases within the combustion region (see Figure 4-16) was re-oxidized before the moving particles reached the end of the oxidation region. In other words, the percentage of oxygen capacity of all cases consumed from CuO particles within the combustion region was completely recovered with only a 60% conversion of the oxygen flowing over the oxidation region. The highest percentage

recorded was case 5 (see Figure 4-10, Figure 4-11 and Figure 4-12). Moreover, the area of the oxidation region can be shrunk in all cases (each by a different size) into a smaller area of the bed, and thus the unused area of the oxidation region can be utilized either with a combustion region to obtain more fuel conversion and/or a steam region to increase the chance of avoiding internal gas mixing.

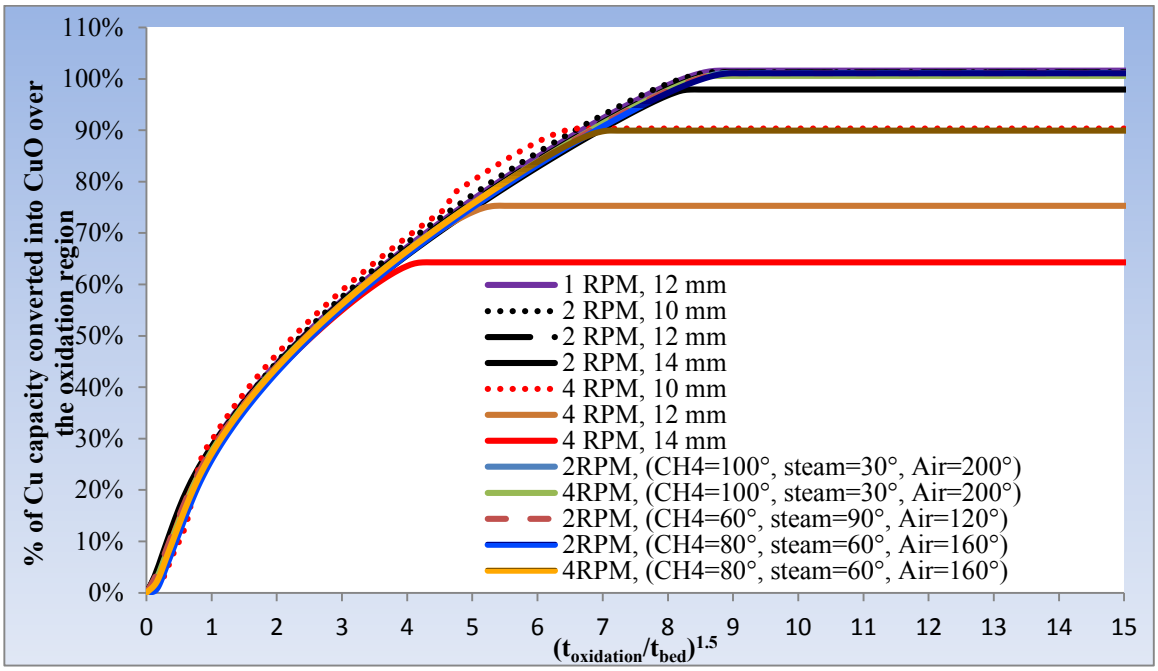

Figure 4-21 The percent of Cu capacity converted into CuO over the oxidation region of twelve modeling runs with different bed thicknesses and gas section area. The first seven cases have the same gas sections area as the validation case, and the last five cases have the bed thickness as the validation case.

Figure 4-22 shows the average of O_2 concentration (mol/m^3) within the bed, which depends on the percentage of oxygen absorbed by copper over the oxidation region. Although the highest percentage among all cases (60%) of oxygen absorbed over the oxidation region was obtained by case 5 (see Figure 4-10, Figure 4-11 and Figure 4-12), the highest average of oxygen (2.39 mol/m^3) was reached by some points over the bed before the end of the oxidation region in all cases, including case 5. The oxidation region has a high area that ranges between 120° and 240°, which is considered to be the largest area (up to double) compared to the combustion and/or steam region. Consequently, the average of oxygen flowing over the oxidation region was high and

more than sufficient for all cases, which resulted in O_2 crossover into the steam region and then to the combustion region, as illustrated in the next figure (Figure 4-23).

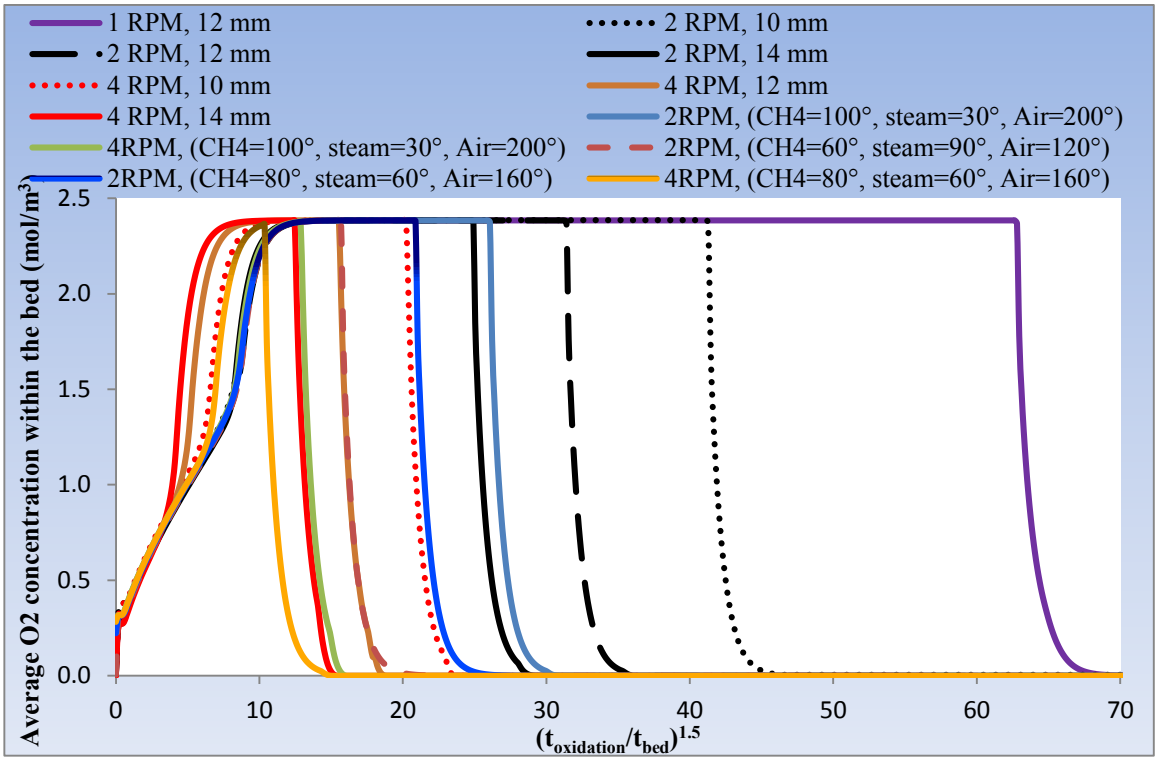

Figure 4-22 Average O_2 concentration within the bed (mol/m^3) of twelve modeling runs with different bed thicknesses and gas section areas. The first seven cases have the same gas sections area as the validation case, and the last five cases have the same bed thickness as the validation case.

Figure 4-23 shows that the average unabsorbed O_2 concentration (mol/m) was ended within steam region as a crossover from the oxidation region in to the steam region. Since the highest amount of oxygen absorbed over the oxidation region is 60% (case 5), all cases have high unabsorbed oxygen, leading to longer purge times being needed to eliminate O_2 crossover from the oxidation region into the combustion region. In some cases, the O_2 crossover passed into beyond of the first half of the steam region (combustion region). The highest O_2 crossover among all cases was given by cases having either high rotation speed or small areas of steam regions along with low oxygen absorption over the oxidation region, such as 4 RPM, 14 mm, 4 RPM, 12 mm, case 1 and case 2 (see Figure 4-11 and Figure 4-12). In order to avoid this high crossover, the unused area of the oxidation region can be utilized within the steam region for larger

areas to have all O_2 crossover ends within the first half of the steam region (i.e., oxidation region). It is suggested that $(t/t_{bed})^{1.5}$ be at least 3 within the steam region before reaching the divider plate to avoid N_2 and O_2 crossover.

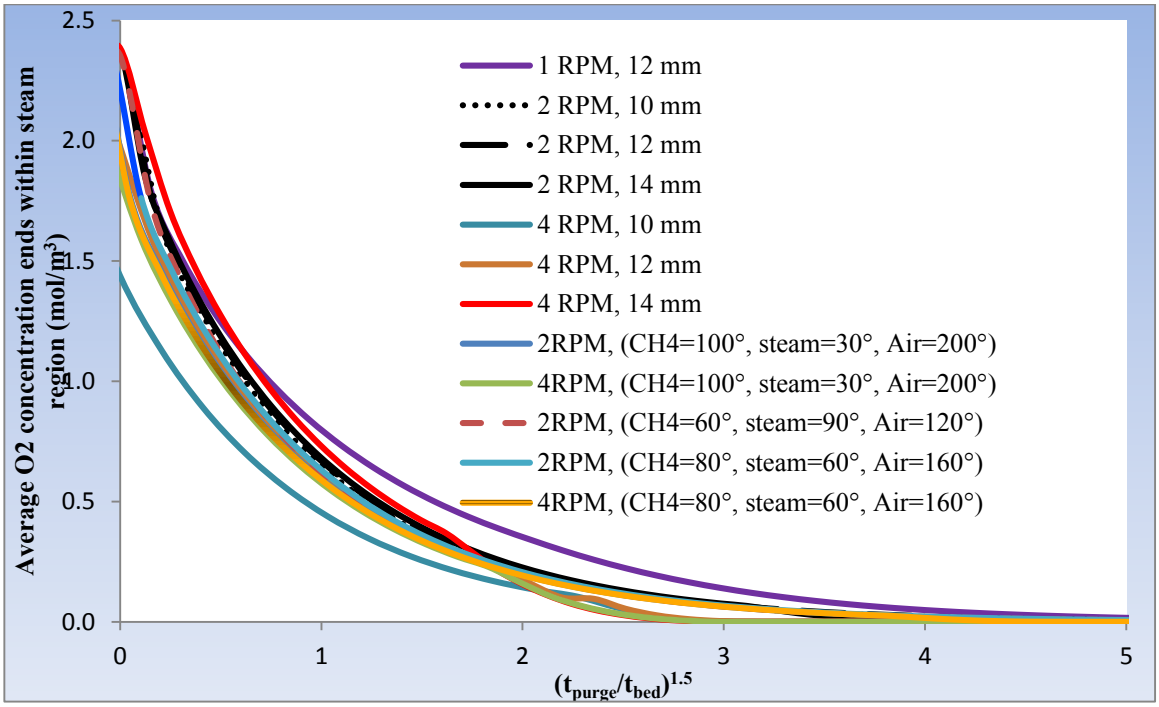

Figure 4-23 Average O_2 concentration ends within the steam region (mol/m^3) of the twelve modeling runs with different bed thicknesses and gas section areas. The first seven cases have the same gas sections area as the validation case, and the last five cases have the same bed thickness as the validation case.

4.9 Optimal Case Design

In order to estimate the optimal design and operating conditions that can be used for the rotating bed reactor, an analysis of results in Section 4.8 was completed. For example, as illustrated in Figure 4-16, to ensure that the particles of the bed have sufficient oxygen capacity over the combustion region, $(t_{combustion}/t_{bed})^{1.5}$ must not exceed 7. Almost 100% oxygen capacity was used to obtain an 82% CH_4 conversion (see Figure 4-17) with most cases simulated in this work. With an 82% CH_4 conversion within the combustion region, $(t_{purge}/t_{bed})^{1.5}$ of the steam region follows the combustion region (suggested to be 3 to the barrier with 0.5 after the barrier) to prevent a crossover of CH_4 and CO_2 into the oxidation region (see Figure 4-18 and Figure 4-20).

In order to convert 100% of Cu into CuO and avoid inefficient operating time and energy over the oxidation region, $(t_{oxidation}/t_{bed})^{1.5}$ must not exceed 9 as shown in Figure 4-21. Here we can see that the highest average concentration of O_2 (2.39 mol/m^3) was reached (see Figure 4-22). To avoid a high crossover of O_2 and N_2 into the combustion region, $(t_{purge}/t_{bed})^{1.5}$ of the steam region follows the oxidation region was calculated to be 2.5 at the barrier and 0.5 after the barrier. Since $(t_{combustion}/t_{bed})$ of the combustion region, (t_{purge}/t_{bed}) of the steam region following the combustion region, $(t_{oxidation}/t_{bed})$ of the oxidation region and (t_{purge}/t_{bed}) of the steam region following the oxidation region were calculated to be 3.66, 2.3, 4.33 and 2.08, respectively, whereas t_{total}/t_{bed} was found to be 12.37. Therefore, the ratio of the regions is 3.66:2.3:4.33:2.08, corresponding to angles of 106.52°:66.94°:126.01°:60.53°. Thus if the beginning of the combustion region was 0 degree, the external baffles would be located at 167° and 353°. With this design of the rotating bed and these angles of stream regions, limited cross-over of CO_2 and O_2/N_2 between the regions and limited inefficiencies in both the combustion and oxidation regions can be obtained. Both the rotation frequencies (RPM) and the bed thickness can therefore be adjusted according to the following design equations (Equations 4.9 and 4.10).

$$\frac{t}{t_{bed}} = \frac{rotation\ time}{bed\ time} = 12.37 \tag{4.9}$$

or

$$\frac{60}{RPM}\frac{gas\ velocity}{bed\ thickness} = 12.37 \tag{4.10}$$

So for a bed thickness of 12 mm and the base-case gas velocity (0.01621 m/s), an RPM of 6.55 would be needed. Slower RPM's would result in low conversion of CH_4, while higher RPM's would induce CO_2 and O_2 crossover.

A simulation with 12 mm bed thickness, 0.01621 m/s gas velocity and 6.55 RPM rotation frequency, represents the optimal case design was performed to investigate the design equation 4.10 for future work. Figure 4-24 shows the main results of the optimal case design compared to the best results obtained of two cases (case 3 and case 5) simulated before the analysis of results. The highest methane conversion, the highest CO_2 recovery/purity, the highest O_2 conversion (efficient use of the oxidation region area) and

zero gas crossover between combustion and oxidation regions were attained by the optimal case design. Therefore, the design equation 4.10 was successfully created and used with the optimal case design, and it can be used in any future work with different rotation speed and/or different bed thickness.

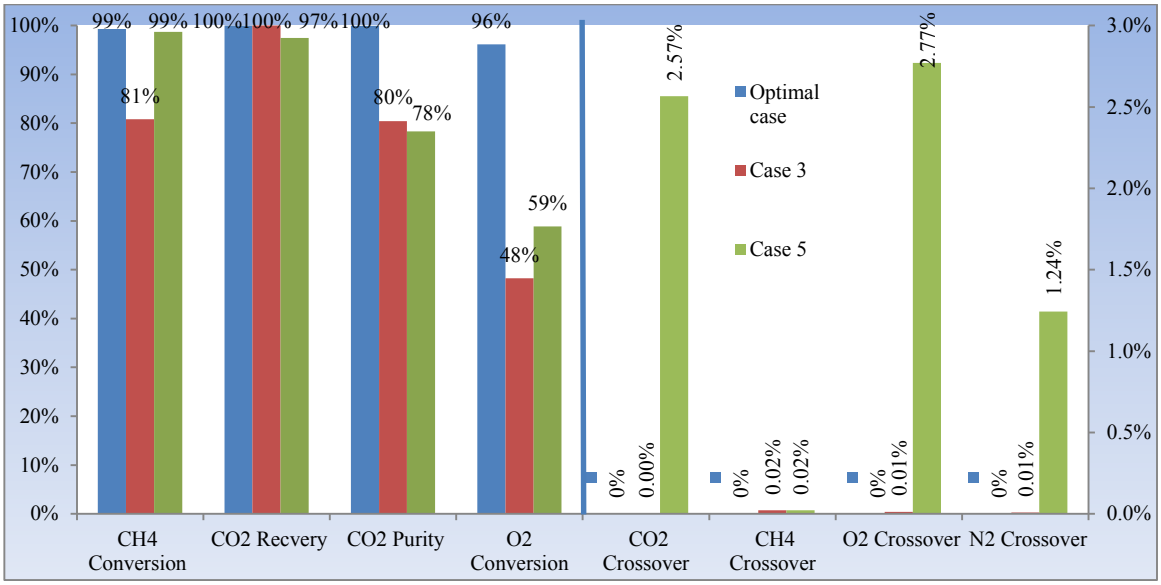

Figure 4-24 Results of the optimal case design compared to the best results obtained by two cases (case 3 and case 5) simulated before the analysis of result.

4.10 Effect of Geometric Assumptions

As discussed in section 3.4, the primary effect of the simplified assumptions of geometry design in this work is in t_{bed}. A correlation based on the CFD approach was figured out where the performance is adjusted by $(t/t_{bed})^{1.5}$. t_{bed} in the actual geometry of the rotating bed reactor (RBR) is greater than t_{bed} in the channel assumed by this study to represent the rotating bed, (see Figure 3-4 a and b).

$$t_{bed_{RBR}} = \frac{bed\ volume}{volematric\ flow\ rate} = \frac{(\pi(0.03)^2 - \pi(0.018)^2)H}{u_{in}(\pi 0.018)H} = 1.974\ s \qquad 4.11$$

$$t_{bed_{channel}} = \frac{bed\ thickness}{gas\ velocity} = \frac{0.012}{0.01621} = 0.74\ s \qquad 4.12$$

Since all gas regions have a comparable effect of different values of t_{bed}, no change in the configuration (angles for each region) is taken into account. If t_{bed} is higher, the biggest effect is with the purge region where it must be longer to avoid gas crossover. Since the configuration is constant, this would be achieved through a lower RPM relative to the optimum simulated in this work. Some variability in the concentration profiles is expected, but the main effect of a higher t_{bed} would be in the RPM selected in the design equation 4.9 where t/t_{bed} is still going to be 12.37. Therefore, the rotation frequency (RPM) of the optimum design for an actual geometry of the rotating bed reactor can be calculated by the following equation 4.13.

$$\frac{t}{t_{bed_{RBR}}} = 12.37 = \frac{60}{RPM}\frac{1}{1.974} \tag{4.13}$$

$$RPM = 2.47\ rotation/min \tag{4.14}$$

CHAPTER 5. CONCLUSION

In this dissertation, a CFD model of a rotating bed reactor for chemical looping combustion using methane as fuel and a CuO-based oxygen carrier was simulated and the effects of some parameters (e.g., reactor rotation frequency, bed thickness and gas flow regions) were investigated. The model was constructed and studied using the CFD software known as COMSOL. Various rotation speeds of 1, 2 and 4 rotations/min and three different bed thickness values of 10 mm, 12 mm and 14 mm along with six different geometric designs (see Table 4-1) of flow region areas were simulated and investigated to improve the reactor's design and operating conditions.

It was found that, in most cases, a higher rotation speed of 4 RPM resulted in higher fuel conversion, taking into account higher cross-over with some different geometries. As well, wider bed thickness was recommended for higher fuel conversion but not for avoiding internal gas mixing, which is considered to be the main challenge of this reactor. It was found that, the optimal case design (which has a geometry design (see Figure 5-1) of an 106.52° combustion region, 66.94° for the following steam region, 126.01° oxidation region and °60.53 applied with 6.55 rotations/min and 12 mm bed thickness) is considered represent the optimal design and operating conditions, as it gave the best performance among all cases simulated in this work.

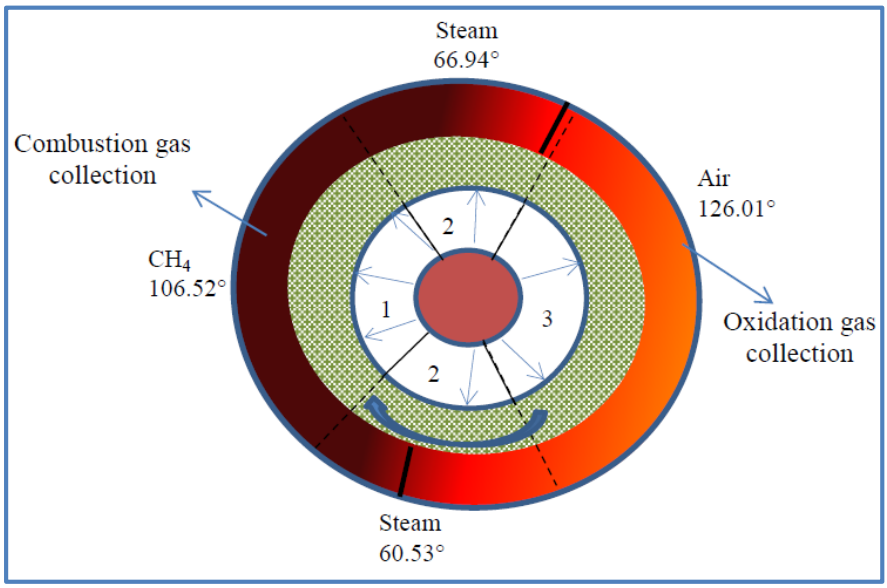

Figure 5-1 Schematic drawing of the optimal case's geometry.

Based on the analysis of the results of this research, dimensionless scaling was applied to provide a graphical method of optimizing the reactor geometry, as well as the rotation rate required for a given gas flow rate. By using the dimensionless scaling, a design equation was created and applied to give the optimal case design with the optimal performance of the rotating bed reactor.

Future work this area should explore these optimums in more detail, using different gas flow rate and applying 2D/3D model, which then can ideally be applied with an experimentally constructed reactor to determine if rotational mass transfer has a significant effect on the dimensionless scaling observed.

REFERENCES

ABAD, A., ADAZ, J., LABIANO, F. G., DE DIEGO, L.F., GAYAN, P., & CELAYA, J. (2007). Mapping of the range of operational conditions for Cu-, Fe-, and Ni-based Oxygen Carrier in Chemical-Looping Combustion. *Chemical Engineering Science* 62 (2007) 533-549.

ADANZ, J., DE DIEGO, L. F., LABIANO, F. G., GAYAN, P., & ABAD A. (2004). Selection of Oxygen Carriers for Chemical-Looping Combustion. *Energy & Fuels*, 18: 371-377.

BERGUERAND, N., & LYNGFELT, A. (2010). Batch testing of solid fuels with ilmenite in a 10 kWth chemical-looping combustor. *Fuel*, 89, 1749–1762 and references therein.

CHO, P., MATTISSON, T., & LYNGFELT, A. (2004*).* Comparison of iron-, nickel-, copper- and manganese-based oxygen carriers for chemical-looping combustion. *Fuel*, 83: 1215– 1225.

DAHL, IVAR. M., BAKKEN, E., LARRING, Y., SPJELKAVIK, I., HAKONSEN, F., & BLOM, R. (2009). On the development of novel reactor concept for chemical looping combustion. *Energy procedia*: 1 1513-1519.

FOGLER, H. S. (2006). Elements of Chemical Reaction Engineering (4th Edition).

GLOBAL CCS INSTITUTE. (2011). "CO_2 Capture technologies." Retrieved from http://www.globalccsinstitute.com/publications/technology-options-co2-capture

HABER J. (1991*).* Manual on catalyst characterization. *Pure &Applied Chemical*. 63: 1227- 1246.

HAKONSEN, S. F., & BLOM, R. (2011). Chemical looping combustion in a rotating bed reactor- finding optimal process conditions for prototype reactor. *Environ. Sci. Technol.* 45 (22), pp 9619–9626. DOI**:** 10.1021/es202244t.

HARVEY, D. L. D. (2000). Global Warming - The Hard Science. Singapore, *Pearson Education Limited.*

HERZOG, H., MELDON, J., & HATTON, A. (2009). Advanced post-combustion CO_2 capture. *MIT Energy, CAT Force*

HOTEIT, A., FORRET, A., PELLETANT, W., ROESLER, J., & GAUTHIER, T. (2011). Chemical looping combustion with different types of liquid fuels. *Oil & Gas Science and Technology-Rev. IFP Energies nouvelles, Vol*. 66: No. 2, pp. 193-199.

IPCC (1997). The regional impacts of climate change - The Scientific Basis, Cambridge University Press.

IPCC (2005). Capture of CO_2 - The Scientific Basis, Cambridge University Press.

ISHIDA, M., & JIN H. (1994). A novel combustor based on chemical-looping combustion reactions and its reactions kinetics. *Journal of Chemical Engineering of Japan*. 27, 296–301.

JERNALD, E., MATTISSON, T., & LYNGFELT, A. (2006). Thermal analysis of chemical looping combustion. *Chemical Engineering Research and Design*, 84(A9): 795–806.

JIN, H., & ISHIDA, M. (2004). A new type of coal gas fueled chemical-looping combustion. *Fuel*, 83: 2411–2417.

KVAMSDAL, H. M., JORDAL, K., & BOLLAND, O. (2007). A quantitative comparison of gas turbine cycles with CO_2 capture. *Energy, 32: 10–24.*

LEWIS, W., & GILLILAND, E. (1954). Production of pure carbon dioxide. *US Patent:* 2,665,971.

LYNGFELT, A., JOHANSSON, M., & MATTISSON, T. (2008). Chemical looping combustion- Status of development. *9th International Conference on Circulating Fluidized Beds* (CFB-9).

LYNGFELT, A., LECKNER, B., & MATTISSON, T. (2001). A fluidized-bed combustion process with inherent CO_2 separation; application of chemical-looping combustion. *Chemical Engineering Science*, 56: 3101–3113.

LYNGFELT, A. (2010). Oxygen carriers for chemical-looping combustion operational experience. *Oil & Gas Science and Technology – Rev. IFP Energies nouvelles,* Vol. 66, No. 2, pp. 161-172.

MATTISSON, T., & LYNGFELT, A. (2001). Capture of CO_2 using chemical-looping combustion. *In Scandinavian Nordic Section of Combustion Institute. Goteborg.*

MCCABE, W. E., SMITH, J.C., & HARRIOTT, P. (2001). Unit Operations of Chemical Engineering.

NASA GODDARD INSTITUTE FOR SPACE STUDIES. (2015). "Global Temperature Anomaly 1880-2015." Retrieved from http://www.giss.nasa.gov/research/features/201501_gistemp/

NOORMAN, S., ANNALAND, M. V. S., & KUIPERS, H. (2007). Packed Bed Reactor Technology for Chemical-Looping Combustion. *Ind. Eng. Chem. Res.46,* 4212-4220.

PROLL, T., KOLBITSCH, P., BOLH_AR-NORDENKAMPF, J., & HOFBAUER, H. (2009). A novel dual circulating fluidized bed system for chemical looping combustion. *Environmental Energy Engineering.* 55, 3255–3266.

RITCHER, H., & KNOCHE, K. (1983). Reversibility of combustion process. *America Chemical Society. Ser.* 235, 71–85.

SEDOR, K. E., HOSSAIN, M. M., & LASA, H. I. (2008). Reduction kinetics of a Fluidizable Nickel-Alumina Oxygen Carrier for Chemical-Looping combustion. *The Canadian Journal of Chemical Engineering,* 86 (3), 323-334.

SON, S. R., GO, K. S., & KIM, S. D. (2009). Thermogravimetric Analysis of Copper Oxide for Chemical-Looping Hydrogen Generation. *Ind. Eng. Chem. Res*: *48,* 380–387.

STRÖMBERG, L. (2001). Combustion in a CO_2/O_2 Mixture for a CO_2 Emission Free Process. *Centre for Environment and Sustainability Chalmers University of Technology & Göteborg University*. 58-63

TRAMBOUZE, P., & EUZEN, J. (2004). Chemical Reactors: From Design to Operation. Paris: Editions Technip.

U.S. Department of Commerce, National Oceanic & Atmospheric Administration | NOAA Research. (2015). "Trends in Atmospheric Carbon Dioxide." Retrieved from http://www.esrl.noaa.gov/gmd/ccgg/trends/